Chromatin architecture and physical constriction cooperate in phenotype switching and cancer cell dissemination

Pietro Berico[1,2,#], Cody Dunton[3], Luay Almassalha[4], Amanda Flores-Yanke[1,2], Karla I. Medina[3], Nicolas Acosta[3], Tara Muijlwijk[2,5], Catherine Do[1,6], Soobeom Lee[1,6], Sharon N Edmiston[7,8,9], David L. Corcoran[7,8,9], Allison Reiner[10], Caroline Kostrzewa[10], Kathy Dorsey[7,8,9], Milad Ibrahim[2,5], Ronglai Shen[10], Nancy E. Thomas[7,8,9], Amanda W. Lund[2,5], Ata S. Moshiri[5], Iman Osman[2,5], Iannis Aifantis[1,6], Jane A. Skok[1,6], Vadim Backman[3,#], Eva Hernando[1,2,#]

[1] Department of Pathology, NYU Grossman School of Medicine, New York, NY, USA.

[2] Interdisciplinary Melanoma Cooperative Group, Perlmutter Cancer Center, NYU Langone Health, New York, NY, USA.

[3] Department of Biomedical Engineering, Northwestern University, Evanston, IL 60208, USA.

[4] Medical Scientist Training Program, Feinberg School of Medicine, Northwestern University, Evanston, IL 60611, USA.

[5] The Ronald O. Perelman Department of Dermatology, New York University School of Medicine, New York, NY, USA.

[6] Perlmutter Cancer Center, NYU Langone Health, New York, NY, USA.

[7] Department of Dermatology, School of Medicine, University of North Carolina, Chapel Hill, NC.

[8] Lineberger Comprehensive Cancer Center (LCCC), University of North Carolina at Chapel Hill, Chapel Hill, NC.

[9] Department of Genetics, School of Medicine, University of North Carolina, Chapel Hill, NC.

[10] Memorial Sloan Kettering Cancer Center, New York, NY, USA.

#Corresponding authors: Eva.Hernando-Monge@nyulangone.org, v-backman@northwestern.edu, Pietro.Berico@nyulangone.org

Abstract

Phenotypic plasticity is a prominent cancer feature that contributes to metastatic potential and resistance to therapy across multiple cancer types. Cancer cell state transitions have been attributed to transcriptional programs, such as the AP1/TEAD-regulated gene network driving the mesenchymal-like (MES) phenotype. In addition, during dissemination, tumor cells are subjected to variable loads of physical mechanical pressure and constriction across transited tissue, which are thought to impact nuclear molecular crowding. How the interplay between mechanical pressure, global 3D nuclear architecture and transcriptional programs contributes to MES identity and metastatic adaptation remains unclear. Using cutaneous melanoma as a model for early dissemination, we integrate in vitro and in vivo epigenomic profiling with nanoscale imaging of cell lines and patient samples to investigate chromatin organization features underlying the MES phenotype. We find that in MES cells, CTCF is relocated from domain boundaries to regulatory regions of EMT-like genes, leading to reduced insulation, extended topological associated domains (TADs) and increased inter-domain contacts, and de novo formation of chromatin hubs. This conformational rewiring, along with loss of heterochromatin, supports nuclear deformability during invasion and dissemination. Conversely, physical constriction of melanocytic cells induces MES-like chromatin features —including CTCF repositioning and heterochromatin loss— and promotes metastasis in vivo. Similarly, pharmacological inhibition of the heterochromatin mark H3K9me3 triggers MES characteristics and increases invasiveness. These results demonstrate that metastatic competency involves both epigenetic and structural nuclear reprogramming, enabling shifts in gene networks and physical adaptability. Our findings reveal mechanistic links between nuclear architecture and aggressive tumor behavior, identifying potential biomarkers and therapeutic targets to intercept metastatic progression.

Introduction

Metastasis is the leading cause of death among cancer patients[1-3]. Still, the mechanisms behind cancer dissemination remain largely unknown[4] and an unmet need to advance therapeutic options. Modern omics technologies have proven that (irreversible) genetic mutations do not fully explain cancer cell metastatic behavior nor patients' outcome, while 'reversible' epigenetic mechanisms can also confer aggressive potential[5, 6]. Cancer cells acquire transient phenotypic states through heritability and plasticity of gene regulatory networks (GRNs) led by different transcription factors (TFs)[7], as an adaptive response to the tumor microenvironment stimuli[8]. Among the cues, tissue cellular density and matrix composition exert biodynamic forces directly toward tumor cells which can increase molecular crowding within the nuclear compartment[9-11].

CTCF is the master regulator of nuclear architecture and, together with cohesin complex, nuclear lamina, non-coding RNAs, and other DNA and RNA-binding proteins pack the two meters long human DNA into chromatin, which expands and contracts to regulate gene expression, DNA replication and repair, RNA transcription and splicing[12]. Chromatin is organized into thousands of nanoscale chromatin packing domains (CPDs) that are only vizualied by super-resolution imaging. These are typically up to 200 nm in size and containing 10 kb to 1 Mbp of DNA. These domains represent a distinct organization layer in addition to compartments, TADs and loops that are defined by contacts through chomatin conformation capture or similar approaches, and may function as transcriptional memory elements[13-16]. Not surprisingly, alterations in nuclear architecture can lead to cancer[17]. For instance, genetic and epigenetic aberrations can disrupt compartments, domains and structural loops to rewire cis-regulatory elements (CRE)[18-22] and establish oncogenic chromatin hubs[23, 24], composed of CREs simultaneously contacting multiple genes involved in pro-tumorigenic biological processes.

Recently, it has also emerged that chromatin regulation provides nuclear physical structure, mechanical rigidity[25, 26] and shape[27] which steer microenvironment adaptability[28, 29] and may ease tumor cell compression during intra- and extravasation in the metastatic cascade[30]. Concomitantly, mechanical compression can directly rewire 3D chromatin, establishing an intricated bi-directional regulatory feedback between the two processes[28, 31, 32,33] . The amount and maturation of CPDs within the nucleus changes the mechanical stability of a cell; for instance, stable mature domains have been shown to lower the probability of blebbing during cell migration, with predominantly 'domain-less' chromatin forming the blebs.[34] However, the impact of constriction-induced changes on nuclear architecture and phenotype switch during metastasis remains unclear.

A mesenchymal or dedifferentiated cancer cell state (MES), enriched on an epithelial-to-mesenchymal-transition (EMT) program, is thought to be the founder of dissemination in multiple cancer types[35-39]. Skin cutaneous melanoma (SKCM) represents an exquisite model of metastasis because it can disseminate from thin primary lesions[40] —which already display intra-tumor heterogeneity including MES cells[39, 41, 42]— irrespective of the genetic drivers. In response to microenvironmental cues[43], melanoma cells 'switch' from a differentiated melanocytic-like state (MEL) led by MITF/SOX10 GRNs, to an EMT-like, AP1/TEADs-dependent MES phenotype[44, 45]. However, MITF/SOX10 and AP1/TEADs silencing are insufficient to trigger a complete switch toward a MES state[46, 47], suggesting other changes in addition to differential gene expression are required [45, 47-53]. We propose that the bi-directional interplay between nuclear 3D chromatin organization and physical compression critically shapes cancer cell plasticity by impacting both gene expression and mechanical properties. In the context of melanoma, our understanding of global nuclear architecture and its contribution to phenotypic plasticity and metastasis is largely unknown.

102 Combining multiple omics techniques, we profiled the nuclear physical properties and global 3D
103 chromatin architecture of patient samples, and of a large panel of melanoma cell lines
104 representative of distinct phenotypic states (MEL, intermediate —INT— and MES) or MEL upon
105 silencing of MITF and SOX10 (siMS), the key GRNs of the MEL state. Compared to MEL, siMS
106 and INT cells, we observed a dramatic rewiring of 3D chromatin in MES cells and a preferential
107 binding of CTCF to CRE of EMT-related genes and chromatin hubs over TAD boundaries.
108 Accordingly, silencing of CTCF re-activates MEL-like GRNs and disrupts the activity of a subset
109 of chromatin hubs, some of which support MES cell migration. While melanoma states exhibit
110 extensive differences in nuclear topology, these only result in limited transcriptional changes,
111 suggesting that MES-like 3D chromatin features confer additional biological properties
112 contributing to metastasis beyond gene expression, such as nuclear deformability and flexibility.
113 Supporting this hypothesis, we find MES cells display higher nuclear flexibility and lower stiffness
114 by mathematical polymer simulations, Partial Wave Spectroscopy (PWS) reduced H3K9me3
115 packing scale domains by spectroscopic single-molecule localization microscopy (sSMLM) and
116 increased cis-long interactions by HiC. Strikingly, these molecular features are partially adopted
117 by MEL cells undergoing constriction during transwell migration or upon H3K9me3 inhibition,
118 which are both independently able to increase their metastatic potential. Altogether, our study
119 shows that nuclear architecture and cell compression co-regulate gene expression and
120 mechanical properties unleashing the MES identity and metastatic capacity.
121

122 **Methods**

123 **Cell culture**

124 All melanoma cell lines were grown at 37°C in 5% CO_2 and routinely tested for mycoplasma
125 contamination using MycoAlert® PLUS Mycoplasma Detection Kit (Lonza, #LT07-703). SKMEL-
126 5, SKMEL-28, SKMEL-239 and SKMEL-147 were kindly provided by Alan Houghton (Memorial

127 Sloan-Kettering Cancer Center, New York, NY, USA); 501mel were purchased from Yale
128 University, MM cell lines (MM057, MM074, MM087, MM029 and MM099) were obtained from Prof.
129 Ghanem Ghanem (Institute Jules Bordet, Bruxelles, BE). MM047 cells were obtained from
130 Frédéric Coin and Irwin Davidson (IGBMC, Illkirch, France). 501mel and SK-MEL cell lines were
131 grown in 10% Fetal Bovine Serum (FBS) in DMEM and penicillin-streptomycin (PS). MM cell lines
132 were grown in Ham-F10 supplemented with 10% FBS, PS and 2mM L-Glutamine.
133 Cells were transfected with 25nM of siNTC (Horizon Discovery, #D-001810-10), siMITF (Horizon
134 Discovery, #L-008674-00) and siCTCF (Horizon Discovery, #L-020165-00) using Lipofectamine
135 RNAiMAX (Thermo Scientific Scientific, 13778150) following manufacturer's instructions.
136
137 **Transwell migration assay**
138 For migration under constriction, $1x10^6$ 501mel and MM099 were seeded into cell culture inserts
139 with 3.0μm pore size (Corning, #353091) into a dedicated 6 well plate (Corning, #353502) and
140 grown in complete media. 72hrs later, cells were gently detached from both sides of the insert
141 using trypsin and processed for HiC, CUT&Tag (CTCF, H3K9me3 and H3K27ac), ATAC and
142 RNAseq.
143 To assess the effects of H3K9me3 perturbation, $1\text{-}2x10^5$ 501mel and SKMEL-28 were seeded
144 into cell culture inserts with 8.0μm pore size (Corning, #353097) placed into a dedicated 24 well
145 plate (Corning, #353504) and grown in complete media supplemented with DMSO or 5nM
146 Chaetocin (MedChem Express, #HY-N2019) for 12-24hrs. Next, inserts were rinsed twice in PBS
147 and fixed with 4% PFA-PBS solution (Electron Microscopy Sciences, #15733-10) for 10min at
148 room temperature. Next, inserts were stained in 0.2% crystal violet solution for 15min at room
149 temperature, rinsed in distilled water by simultaneously cleaning the inner side with a cotton swab.
150 After drying at room temperature, inserts were imaged using a digital brightfield microscope
151 (Invitrogen, EVOS core) and quantified with ImageJ.

152

153 **ChIP and HiC**

154 Melanoma cell lines were double crosslinked for 30min in 25nM EGS (Thermo Scientific Scientific,
155 #21565) and for 10min in 1% FA (Sigma-Aldrich, #47608) at room temperature and then
156 processed for ChIP and HiC.

157 For ChIP, $1x10^7$ cells were lysed in ChIP lysis buffer (CLB = 10mM Tris HCl pH8, 100mM NaCl,
158 1mM EDTA pH8, 0.5mM EGTA pH8, 0.1% Sodium Deoxycholate, 0.5% N-lauroylsarcosine, 1%
159 Triton X-100) and sonicated with Diagenode Bioruptor for 15-30 cycles (30" ON +30" OFF max
160 intensity). 5ug/IP of H3K27ac antibody (Active Motif, #91193), H3K9me3 (Active Motif, #61013)
161 or IgG control (Cell Signaling Technology, #3900) were prebound to 50ul of Protein A/G magnetic
162 beads (Pierce Thermo Scientific Scientific, #88803) in PBS+BSA 0.5% for 1hr @RT. Chromatin
163 was diluted to 1ml in CLB and magnetic beads-antibody complex was added to each IP ON at
164 4°C on revolver. IP were washed twice in Wash Buffer I (WBI, 20mM Tris HCl pH7.5, 150mM
165 NaCl, 2mM EDTA pH8, 0.1% SDS, 1% Triton X100), Wash Buffer II (WBII, 10mM Tris HCl pH8,
166 250mM LiCl, 1mM EDTA, 1% Triton X100, 0.7% Sodium Deoxycholate) and TET Buffer (10mM
167 Trist HCl pH8, 1mM EDTA, 0.2% Tween20) and eluted in Elution buffer (EB, 10mM Tris HCl pH8,
168 300mM NaCl, 5mM EDTA pH8, 0.5% SDS, 10ug RNAse A, 100ug proteinase K) 30min at 37°C
169 + ON at 55°C. IP elutions were purified using MinElute Reaction Cleanup kit (Qiagen, #28204)
170 and libraries were prepared using NEBNext Ultra II DNA Library Prep Kit for Illumina (NEB,
171 #E7600S) following manufacturer's instructions.

172 For HiC, $2.5x10^6$ cells were processed using Arima-HiC+ kit (Arima Genomics, #A101020)
173 following the manufacturer instructions. HiC libraries were generated using Arima-HiC+ kit (Arima
174 Genomics, #A510008, #A303011) following manufacturer's instructions.

175 ChIP and HiC libraries were pooled together at 2nM concentration and sequenced paired-end
176 2x150bp using Illumina NovaSeqX+.

177

178 **HiC in DNA from FFPE tissues**

179 Between 5-10 Formalin Fixed Paraffin Embedded (FFPE) patient tumor tissue sections of 10μm
180 per sample were cut and pooled in a 1.5mL tube for de-waxing and re-hydration using xylene,
181 ethanol and molecular grade water. Next, FFPE samples were processed with the Arima-HiC+
182 FFPE Kit (Arima Genomics, #A101060) following manufacturer's instructions. HiC FFPE libraries
183 were generated using Arima-HiC+ kit (Arima Genomics, #A510008, #A303011) following
184 manufacturer's instructions.

185

186 **Omni-ATACseq**

187 $5x10^5$ cells were harvested and assessed to not have more than 15% of cell death using trypan
188 blue. Next, dead cells were additionally removed treating cells with 200U/ml of DNAse
189 (Worthington, #LS002007). Cells were resuspended in 500ul of cold buffer 1 (10mM Tris-HCl pH
190 7.5, 10mM NaCl, 3mM $MgCl_2$, 0.1% NP-40, 0.1% Tween-20) and the equivalent volume for $5x10^4$
191 cells (50ul) was kept for the next steps. A final concentration of 0.1% of digitonin was added to
192 the cells and incubated on ice for 3 minutes. Digitonin permeabilization was quenched adding 1ml
193 cold buffer 2 (10mM Tris-HCl pH 7.5, 10mM NaCl, 3mM $MgCl_2$, 0.1% Tween-20). Afterward, cells
194 were pelleted and resuspended in 50ul of transposition mixture (20mM Tris HCl pH 7.5, 10mM
195 $MgCl_2$, 20% dimethyl formamide, PBS, 1% digitonin, 10% tween-20) supplemented with 2.5-5ul
196 of Transposase (Illumina, #20034197) and incubated in thermomixer at 37°C for 30 minutes with
197 1000rpm. Transposition mixture was purified using DNA Clean and Concentrator-5 kit (Zymo,
198 #D4014) for library preparation. 20ul of transposed DNA was processed for Nextera library using
199 the same protocol described in Schmidl work[54]. OmniATAC libraries were pooled together at 2nM
200 concentration and sequenced paired end 2x150 using Illumina NovaSeqX+.

201

202 **CUT&Tag**

203 For CTCF genomic occupancy was assessed using CUT&Tag-IT™ (Active Motif, #53160)
204 following manufacture instructions. Briefly, 1.5-5x10^5 cells were captured with concanavalin A
205 beads and 1ug of IgG control (Cell Signaling Technology, #3900) or CTCF (Active Motif, #61311)
206 antibodies were incubated 2hrs at 4°C on revolver in cell lysis buffer. For H3K9me3 and H3K27ac
207 Pre and Post migration, 1ug of antibodies H3K9me3 (Active Motif, #39062) and H3K27ac (Active
208 Motif, #39133) were incubated overnight at 4°C on revolver in cell lysis buffer. Afterward, 1ul of
209 guinea pig anti-rabbit antibody was added to the reaction followed by 1hr of tagmentation at room
210 temperature with 1ul of Tn5 transposase enzyme. Tagmentation was stopped with EDTA, SDS
211 and proteinase K incubation for 1hr at 55°C. Tagmented DNA was purified using DNA purification
212 reagents within the kit. Finally, tagmented DNA was processed for Nextera library preparation
213 using i7 and i5 indexed primers and Q5 TAQ polymerase. CUT&Tag libraries were pooled together
214 at 2nM concentration and sequenced paired end 2x50 using Illumina NovaSeqX+.

215

216 **RNAseq**

217 Total RNA libraries were prepared using automated TruSeq stranded total RNA and RiboZero
218 Gold kit (Illumina, #RS-122-2301) according to the manufacturer's instructions. RNA libraries
219 were sequenced paired end 2x50 using Illumina NovaSeqX+.

220

221 **Methylation array**

222 DNA methylation profiling was performed using the genome-wide Infinium MethylationEPIC array
223 (Illumina) as described previously[55]. Briefly, DNA (250ng/ sample) from melanoma cell lines was
224 extracted with QIAamp DNA Micro Kit (Qiagen, #56304) and bisulfite-treated using EZ DNA
225 Methylation GOLD kits (Zymo Research, #11-335) according to manufacturer's protocol.
226 BeadArray processing and scanning was performed in the UNC-CH Mammalian Genotyping

227 Core. Methylated and non-methylated control samples (Zymo Research, #50-444-307) were
228 included in the experiment. BeadArray data was assembled using Illumina GenomeStudio
229 methylation module (v3.2). Background intensity from negative controls was subtracted from each
230 data point.
231
232 **Tumor dissociation**
233 Freshly dissected tumors from mice were dissociated at single cell by first chopping the tissue in
234 a petri dish with a scalpel. Then, whole tumors were resuspended in 4mL/gr of HBSS (Sigma-
235 Aldrich, #H6648) supplemented with 750U/ml of Collagenase I (Sigma-Aldrich, #C2674) and
236 625U/ml of DNAse I (Worthington, #LS002138) and incubated for 50min at 37°C upon strong
237 shaking. Cell suspension was sequentially filtered through a first 70μm cell strainer (Fisher
238 Scientific, #22363548) and then a 40μm cell strainer (Fisher Scientific, #22363547). Next, single
239 cell suspensions were depleted of immune and dead cells by flow cytometry sorting (Sony
240 Biotechnology, SY3200 HAPS) using PE-conjugated CD45 (BioLegend, mouse #111103) and
241 DAPI staining.
242
243 **PIPseq**
244 Before processing, cell number and viability were assessed using a TC20 Cell Automated Cell
245 Counter (BioRad). Briefly, cells were partitioned into PIPs (PIPseq T20 3' Single Cell RNA Kits,
246 V4.0PLUS, Fluent BioScience) with subsequent cDNA generation and final library preparation
247 following manufacturer's instructions. Sample input varied from ~80,000 to 200,000 per
248 reaction. cDNA quality and concentration were evaluated on a BioAnalyzer 2100 using a High
249 Sensitivity DNA Kit (Agilent Technologies). Final gene expression libraries were amplified between
250 6 and 15 cycles and visualized on an Agilent TapeStation 4200 using High Sensitivity D1000

251 ScreenTape (Agilent Technologies). Sequencing was performed using a NovaSeq X+ 10B 200
252 Cycle Flowcell (Illumina).
253
254 **Low input HiC (LoHiC)**
255 Between 0.5-1x10^6 tumor cells were double crosslinked and subjected to HiC as previously
256 described[56]. Then, single cells were processed with Chromium Next GEM single Cell ATAC
257 Reagent Kits v2 (10X Genomics) following manufacture instructions.
258
259 **CRISPR/Cas9 screen**
260 MM099 cells were transduced with lentivirus carrying a doxycycline inducible dCas9-KRAB-
261 MeCP2 (Addgene, #140690) and a custom CRISPR library pRSGScribe1 (Cellecta) targeting 43
262 MES hubs plus 2 positive (*ACTB*, *GAPDH*) and 5 negative controls[57] (5 sgRNAs/target) for a total
263 of 230 sgRNAs. Single guide RNAs (sgRNAs) were designed using CRISPick[58]. After viral library
264 titration, cells were infected with a 0.3 MOI to prevent multi-copy insertion and have a maximum
265 of one sgRNA/cell. Finally, cells were collected at day 0 and 21 upon doxycycline induction
266 (1μg/ml). Cell pellets were lysed to retrieve genomic DNA using QIAamp DNA Micro Kit (Qiagen,
267 #56304). sgRNA sequencing libraries for t0 and t21 were prepared using NGS prep kit for sgRNA
268 Libraries with supplementary primers (Cellecta, #LNGS-360, #LNGS-360-SP) following
269 manufacturer's instructions.
270
271 **Spectral partial wave spectroscopy (PWS) Imaging**
272 PWS imaging was performed under physiological conditions (37ºC, 5% CO_2) using a stage-top
273 incubation system (In Vivo Scientific). Cells were seeded on 8-chamber cover glass slides and
274 allowed to adhere for 24 hours prior to imaging. Measurements were acquired on an inverted
275 microscope (Leica DMIRB) equipped with a 63x oil-immersion objective (HCX PL APO, Leica), a
276 CCD camera (ImageEM C9100-13, Hamamatsu), and a liquid crystal tunable filter (LCTF, Cri

277 VariSpec) to enable spectrally resolved imaging. Broadband illumination was provided by a white-
278 light LED source (X-Cite 120 LED, Excelitas), and a long-pass filter (Semrock BLP01-405R-25)
279 was used to reject short-wavelength excitation light. Spectra image stacks were collected from
280 500 to 700 nm at 2-nm intervals, as previously described[59-61].
281 PWS imaging quantifies wavelength-dependent interference patterns arising from multiple light
282 scattering events within the sample, which are sensitive to nanoscale fluctuations in the local
283 refractive index. Because refractive index is proportional to macromolecular density, PWS
284 provides a label-free optical readout of chromatin nanoscale organization. For each pixel in the
285 lateral image plane (x,y), the standard deviation of the backscattered intensity across the spectral
286 dimension (λ) was computed, yielding a local chromatin packing scaling parameter, $D_a(x, y)$. The
287 average nuclear chromatin packing scaling, D_n, was obtained by averaging D_a across all pixels
288 within the nuclear region of interest. D_n reflects the organization of chromatin into spatially
289 segregated packing domains and is derived from optical modeling and chromatin density
290 autocorrelation functions established in prior chromatin tomography and PWS studies[61-63]. For
291 each experimental condition, D_n values were calculated for individual nuclei across biological
292 replicates, and group-level statistics were used to quantify treatment-associated changes in
293 chromatin packing.
294 In addition to live-cell measurements, PWS imaging was also performed on formalin-fixed
295 paraffin-embedded tumor sections. OPAL-stained tumor sections were imaged by PWS and multi-
296 channel fluorescence imaging. PWS and OPAL images were spatially registered, enabling
297 chromatin packing metrics to be associated with immunophenotypically defined cell populations
298 within intact tumor tissue.
299
300 **Dynamic PWS Measurements**
301 Dynamic PWS imaging was performed as previously described[61, 64] to quantify nanoscale
302 chromatin motion in live cells. In this mode, wide-field backscattered intensity was recorded at a

fixed wavelength (550 nm) over time, generating a three-dimensional data cube with dimensions (x, y, t). Temporal intensity fluctuations at each pixel arise from the movement of intracellular macromolecular structures, including chromatin. Fractional moving mass (FMM) was computed from the temporal variance of the backscattered intensity, σ_t^2, and normalized using a biophysical scattering model to convert raw fluctuations into a quantitative measure of nanoscale mass motion. Following Gladstein *et. al.* (2019)[61], FMM is defined as:

$$\sigma_t^2 \cdot \frac{\pi \rho_0}{2\Gamma^2 k^3 n_i} \left(\frac{NA_i}{NA_c}\right)^2 \left(\frac{n_1}{n_m - n_1}\right)^2 = \rho_0 V_{cm} \phi = m_c \phi = m_f$$

Where m_f represents the mass undergoing motion within the sample and is given by the product of the mass of a typical moving cluster (m_c) and the volume fraction of the mobile mass (ϕ). Here, $m_c = \rho_0 V_{cm}$, with V_{cm} denoting the volume of a characteristic moving macromolecular cluster and ρ_0 the dry mass density.

For normalization, the refractive index of a nucleosome was approximated as $n_m = 1.43$, the nuclear refractive index as $n_1 = 1.37$, and the refractive index of the immersion medium as $n_i = 1.518$. The dry density of a nucleosome was taken as $\rho_0 = 0.55\ g\ cm^{-3}$. The scalar wavenumber of the illumination light was $k = 1.57 \times 10^5\ cm^{-1}$, Γ denotes the Fresnel intensity coefficient for normal incidence, and the numerical apertures of collection and illumination were $NA_c = 1.49$ and $NA_i = 0.52$, respectively. As previously reported[61], σ_t^2 is sensitive to instrument-specific parameters, including depth of field and substrate refractive index. These effects were corrected using empirically determined calibration constants. Pixelwise FMM values were calculated for each nucleus, and distributions were compared across experimental conditions to quantify treatment-induced changes in chromatin mobility.

sSMLM

Cells were seeded on 8-chamber cover glass slides (Cellvis, #C8-1.5H-N) and cultured to approximately 30% confluence. Samples were fixed in 4% paraformaldehyde prepared in

328 phosphate-buffered saline (PBS) for 10 minutes at room temperature, followed by two PBS
329 washes. After fixation, cells were quenched in 0.1% sodium borohydride in PBS for 7 minutes.
330 After three PBS washes, cells were permeabilized and blocked in PBS containing 0.2% Triton X-
331 100 and 3% bovine serum albumin (BSA) for 2hrs at room temperature. To label heterochromatic
332 regions of chromatin, cells were incubated overnight at 4ºC with anti-H3K9me3 antibody (Abcam,
333 ab176916) at 1.2 µg/mL in blocking buffer. After 3 washes in PBS with 0.1% Triton X-100 and
334 0.2% BSA, cells were incubated with Alexa Fluor 647-conjugated secondary antibody (Thermo
335 Scientific, #A-21245) at 2 µg/mL for 1 hour at room temperature. Cells were washed twice in PBS;
336 to stain euchromatic regions, the labeling steps aforementioned were repeated using anti-
337 H3K27Ac antibody (Thermo Scientific, #MA5-23516) and tagged with fluorophore Alexa Fluor
338 488-conjugated secondary antibody (Thermo Scientific, #A-11001) at 4 µg/mL in blocking buffer.
339 To conduct imaging in STORM buffer containing 0.5 mg/mL glucose oxidase (Sigma-Aldrich), 40
340 µg/mL catalase (Roche), and 100 mg/mL glucose in TN buffer (50 mM Tris, pH 8.0, and 10 mM
341 NaCl). Super-resolution imaging was performed using a Nikon Eclipse Ti-U inverted microscope
342 equipped with a 100×/1.49 NA oil immersion objective (SR APO TIRF, Nikon) and an iXon Ultra
343 888 electron-multiplying CCD camera (Andor). A 637-nm laser (Obis, Coherent) provided
344 excitation at the sample plane with an average power of 3–10 kW/cm² and using type F immersion
345 oil (Nikon, #MXA22168). At least 10,000 frames were acquired per field of view with a 30 ms
346 exposure time.
347
348 **Western blotting**
349 Cells were harvested and lysed in LSDB buffer (0.5M KCl, 50mM Tris HCl pH 8.0, 20% Glycerol,
350 1% NP40, 1mM DTT) through three cycle of snap freezing in liquid nitrogen and thermobath at
351 37°C. Cell pellet debris was removed with the help of a pipette tip following centrifugation at
352 20.000g for 15min at 4°C. Between 10-20µg of proteins were run into pre-casted gels Nupage™

353 4-12% Bis-Tris (Thermo Scientific) using the dedicated apparatus (Thermo Scientific, #EI0001).
354 Next, separated proteins were transfer into nitrocellulose membranes (Cytiva, #10600011) which
355 were subsequently blocked into 5% milk TBST solution. Primary antibody staining was conducted
356 by diluting antibodies in TBST (between 1:1000-5000 dilution, Supplemental reagents) and
357 incubated overnight at 4°C with the corresponding membranes upon gentle mix. Secondary
358 antibodies HRP-conjugated were diluted 1:10.000 in TBST and incubated 1hr at room
359 temperature with gentle shaking. Protein signal was revealed using luminol substrate mix
360 (Millipore, #WBLUR0500) and detected with an Odyssey XF Imaging System (LICORbio). Protein
361 quantification was conducted using ImageJ.
362
363 **Immunoprecipitation (IP)**
364 Protein immunoprecipitation was conducted as previously described[46]. Briefly, cells were
365 harvested, pellet and gently lysed into 2 pellet volume of hypotonic buffer (10mM Tris HCl pH 7.6,
366 1.5mM $MgCl_2$, 10mM KCl, 0.1% NP40) using mechanical shear with a loose Dounce to release
367 the cytoplasmic fraction. Next, nuclei were pellet and resuspended in 1 volume of sucrose buffer
368 (20mM Tris HCl PH 7.6, 15mM KCl, 60mM NaCl, 0.34M Sucrose) followed by a drop-by-drop
369 gradual integration of 0.3 volumes of high salt buffer (20mM Tris HCl pH 7.6, 25% glycerol, 1.5mM
370 $MgCl_2$, 0.2mM EDTA, 0.9M NaCl) upon gentle vortex. After 30 min incubation at 4°C on constant
371 slow spinning, ruptured nuclei were pellet, nuclear soluble fraction was collected and nuclei were
372 further resuspended in 1 volume of sucrose buffer supplied with 1mM $CaCl_2$ and 20U/μl of
373 Micrococcal Nuclease (NEB, #M0247S), and incubated in thermoblock for 10min at 37°C.
374 Micrococcal digestion was stopped by adding EDTA (final concentration 4mM) and lysate was
375 centrifuged 20.000g for 30min at 4°C to obtain the nuclear insoluble fraction.
376 For CTCF co-IP, 500μg of nuclear insoluble fraction was diluted in 1mL of TGEN buffer (10mM
377 Tris HCl pH 7.6, 150mM NaCl, 3mM $MgCl_2$, 0.1mM EDTA, 10% glycerol, 0.01% NP40) for each

378 IP. 1% of diluted extract was kept as western blot input. Next, between 5-10μg of primary
379 antibodies against CTCF (Cell Signaling Technology, #2899), FOSL1 (Cell Signaling Technology,
380 #5281), FOSL2 (Cell Signaling Technology, #19967), c-JUN (Cell Signaling Technology, #9165),
381 pan-TEAD (Cell Signaling Technology, #13295) and IgG control (Cell Signaling Technology,
382 #3900) were added in each IP and incubated overnight at 4°C on constant slow spinning. The
383 day after, 25μl of magnetic beads A/G (Thermo Scientific, #88803) previously rinsed in PBS +
384 0.5% BSA were added to each IP and incubated 4hrs at 4°C upon slow spinning. Next, beads-
385 antibody-proteins complexes were gently washed five times in cold TGEN buffer and eluted in
386 LSDB and 1X Laemmli buffer in a thermoblock for 10min at 98°C before proceeding with western
387 blot.
388
389 **Immunofluorescence (IF)**
390 Tissue microarrays (TMAs) were sectioned at 5 μm sections and immunostained on a Leica
391 BondRx auto-stainer according to the manufacturer's instructions. In brief, sections were
392 deparaffinized online and underwent antigen retrieval with either ER1 (Leica, AR9961; pH6) or
393 ER2 (Leica, AR9640; pH9) retrieval buffer at 100o for either 20 minutes. Sections were then
394 treated with 3% H2O2 to inhibit endogenous peroxidases. After blocking with Primary Antibody
395 Diluent (Leica, AR93520), slides were incubated with the first primary antibody and secondary
396 HRP polymer pair. Following secondary incubation, slides underwent HRP-mediated tyramide
397 signal amplification with a specific Opal® fluorophore. Once the Opal® fluorophore was covalently
398 linked to the antigen, primary and secondary antibodies were removed with a 95o retrieval step.
399 This sequence was repeated 5 more times with subsequent primary and secondary antibody
400 pairs, using a different Opal fluorophore for each primary antibody against human MITF (Sigma-
401 Aldrich, #HPA003259), TCF4 (Abcam, #ab223073), S100B (Abcam, #ab115803), p-EGFR (Cell
402 Signaling Technology, #4407), AXL (Cell Signaling Technology, #8661), and SOX10 (Sigma-

403 Aldrich, #383R-15). After antibody staining, sections were counterstained with spectral DAPI
404 (Akoya Biosciences, FP1490) and mounted with ProLong Gold Antifade (ThermoFisher Scientific,
405 P36935).
406 Semi-automated image acquisition was performed on an Akoya Vectra Polaris (PhenoImagerHT)
407 multispectral imaging system. Slides were scanned at 40X magnification using PhenoImagerHT
408 2.0 software in conjunction with Phenochart 2.0 and InForm 3.0 to generate unmixed whole slide
409 qptiff scans. Image files were uploaded to the NYUGSoM's OMERO Plus image data
410 management system (Glencoe Software).
411
412 **Computational analysis**
413 *ChIPseq, CUT&Tag and ATACseq*
414 Sequencing results were demultiplexed and converted in fastq using Illumina bcl2fastq software.
415 Next, fastq files were trimmed and filtered according to the qc report obtained with TrimGalore
416 (0.6.6, https://github.com/FelixKrueger/TrimGalore) and fastqc (0.11.7,
417 https://www.bioinformatics.babraham.ac.uk/projects/fastqc/). For ChIP samples, fastq trimming
418 was set for Illumina adaptors; for ATACseq and CUT&Tag, it was set for Nextera adaptors.
419 Alignment to Hg38 human genome was performed using bowtie2 (2.4.1)[65] and sam files were
420 converted into bam using samtools (1.16)[66]. Bigwig files were generated from bam files using
421 bamcoverage (deeptools 3.5.6)[67] and filtered out for duplicate and bad genomic regions. Peak
422 calling was performed using MACS2 (2.2.9.1)[68] using paired-end mode, IgG (ChIP and CUT&Tag)
423 was used as control, a q-value 0.05 threshold was set and both, narrowPeak and summit peaks
424 were filtered for blacklisted regions using bedtools (2.31.0)[69]. An Hg38 CTCF whole genome track
425 generated by JASPAR[70] was used to filter CTCF peaks and maintain only the ones containing the
426 CTCF motif. Peak annotation was performed with homer (4.10)[71] using narrowPeak files and
427 Hg38 genome parameters. DNA motif analysis of CTCF was done by first expanding of 200bp
428 MACS2 summit peaks with bedtools slop, then fasta sequence was obtained using bedtools

429 getfasta which were processed using MEME-ChIP[72]. DiffBind[73] was used to identify state-specific
430 peaks for CTCF, H3K27ac, ATAC and H3K9me3.
431
432 *HiC*
433 For HiC samples, fastq trimming, qc, alignment, valid pairs identification and matrix generation
434 were performed using HiC-Pro workflow (3.1.0)[74] as previously described[75].
435 Briefly, valid pairs outputs were converted into juicer and cool formats using hicpro2juicebox and
436 hicpro2higlass respectively (HiC-Pro). Matrix normalization was performed using cooler balance
437 (cooltools)[76] and addNorm (juicer tools)[77]. Copy number variations (CNVs) and structural variants
438 (SVs) were detected using HiNT[78] cnv and tl functions at 50kb BIN resolution and chromosomes'
439 segmentation were pooled into one file and converted in Log2 using python. Segments with a
440 $Log_2 \geq 0.5$ and $Log_2 \leq -0.5$ were considered amplified and deleted respectively. HiC-Pro valid pairs
441 were filtered for CNVs and SVs using bedtools pairtobed. Compartment calling was conducted
442 using eigs-cis function (cooltools) and 100kb BIN resolution matrixes. For compartment switch
443 analysis, compartment score data from multiple cell lines were combined in a single text-
444 delimited-file and delta switch was calculated as described in Narang et al[19]: compartments
445 flipping sign with an absolute difference ≥0.5 and an absolute delta ≥1.2 were considered
446 switched. Compartments' saddle-plot was generated with cooltools. To measure H3K9me3,
447 H3K27ac, ATAC and RNA RPKM enrichment in the compartments, bigwig files from these
448 markers were segmented in 100KB BIN and averaged in each compartment using deeptools.
449 Topological Associated Domains (TADs) identification was conducted using cooltools insulation
450 providing an input matrix of 10kb BIN resolution, a 120kb window and Li threshold. From the tsv
451 output, i) TADs boundaries were identified if considered 'true' under the 'is_boundary' column and
452 ii) if the distance between two boundaries is less or equal to 3Mb was considered as a domain[79].
453 Loops were called using both 10kb and 5kb BIN matrixes with Peakachu[80] and 10kb and 5kb

were merged using hicMergeLoops (HiCexplorer). TADs boundaries and loops anchors co-occupied by CTCF were retained for downstream analysis using bedtools intersect and hicValidateLocation (HiCexplorer) respectively. HiC pile up maps, intra-TAD and inter-TAD contacts data were generated using GENOVA r package[81]. CTCF occupancy at loops anchors and TADs boundaries was calculated and visualized using deeptools. Loops and TADs were annotated using bedtools intersect and pairtobed against GENCODEv44 Hg38 bed file downloaded from UCSC Genome Browser. Graphs were generated combining Prism10, R and phyton.

ABC-score model

Active-by-Contact (ABC) model[82] was generated following the authors guidelines (https://github.com/broadinstitute/ABC-Enhancer-Gene-Prediction) as previously described[75]. Briefly, cCRE were called and measured in activity using makeCandidateRegions and run.neighborhoods scripts in which ATACseq and H3K27ac bam and narrow.Peaks are integrated. Next, HiC matrix were processed using juicebox_dump and compute_powerlaw_fit_from_hic to extrapolate genome wide contacts. ABCscore for each active cCRE was measured using predict function in which cCRE, HiC contacts and RNAseq are integrated. Finally, cCRE were filtered using an ABCscore threshold of 0.02 and self-promoter contacts were excluded for downstream analysis. DESeq2[83] was used to identify differentially active cCRE across melanoma cell lines.

To identify chromatin hubs, sumABC (ΣABC) was calculated for each cCRE as the sum of all contacted genes per cCRE and it was calculated with R (4.4.1) using the corresponding formulas:

$$\Sigma ABC = \sum_{j=1}^{g_i} ABC_{i,j}$$

ABC = score

g = gene

Next, each cCRE was ranked based on the number of contacting genes with an expression level of Transcript Per Million (TPM) ≥1.

Polychrom

Chromatin 3D dynamics were simulated using a modified version of the Polychrom engine (OpenMM-based molecular dynamics, https://github.com/open2c/polychrom), implemented in our custom pipeline. Briefly, each chromosome is represented as a coarse-grained polymer, where individual 10 kb bins from Hi-C data correspond to "beads" connected by harmonic bonds (rest length = 1). Angular stiffness of each bead (k_θ) is computed from integrated epigenetic, Hi-C, and TAD information:

- Epigenetic terms: local enrichment of H3K27ac and H3K9me3 (BigWig tracks)
- Compartment identity (A/B): sign(E1) from eigenvector decomposition
- TAD topology: TAD size-normalized scaling factor
- Hi-C contact environment: short-range, long-range, and inter-TAD interactions

Stiffness was modeled as:

$$k_i = \exp\left(-0.40Z_{27} + 0.28Z_9 - 0.25sign(E1)\right) \times TAD_{factor} \times f(HiC)$$

followed by clipping to a biophysically stable range (0.3–4.0). Softness is defined as:

$$s_i = \frac{1}{k_i}$$

All forces used in the simulation include harmonic bonds, angular stiffness (per-bead k_θ), excluded volume via polynomial repulsion and high-confidence Hi-C–derived long-range harmonic restraints (above a quantile threshold). An initial random-walk polymer is energy minimized and then propagated in Langevin dynamics for 150k integration steps (timestep 40 fs). Snapshots are

saved every 5,000 steps using Polychrom's HDF5Reporter, generating bead-track annotation, full 3D trajectory, contact map, per-frame radius of gyration (Rg) and curvature-based softness. Outputs include genome-wide stiffness tracks, compartment-stratified distributions, TAD-level summaries, and effective chromosome stiffness calculated from mean curvature across all trajectory frames. To quantify chromatin deformability under nuclear constriction, we implemented an additional energy-minimization pipeline. For each sample, the final equilibrium chromatin configuration from the Polychrom simulation is subjected to increasing levels of axial compression inside a narrowing slit. Given a slit half-height *h*, all beads satisfying $|z| > h$ are energetically penalized by a soft-wall potential:

$$U_{slit} = \frac{1}{2} k_{wall} (|z| - h)^2$$

For each constriction level (typically *h* =1.0, 0.8, 0.6, 0.4, 0.3), the system undergoes NaN-safe local energy minimization and extraction of total system energy and principal radii of gyration (Rg1 ≤ Rg2 ≤ Rg3). This yields per-sample tables of Energy(h) and Rg(h). For each sample, deformability metrics were computed from the relaxed (largest slit size) and tight (smallest slit size) states:

- Constriction energy cost:

$$\Delta E = E_{tight} - E_{relaxed}$$

- Axial deformability (compression along Rg1):

$$frac_Rg1 = \frac{Rg1_{tight}}{Rg1_{relaxed}}$$

- Changes in chromatin anisotropy:

521 $$\Delta Flattening = (\frac{Rg3}{Rg1})_{tight} - (\frac{Rg3}{Rg1})_{relaxed}$$

522 These metrics quantify whether chromatin becomes shorter, flatter, or more anisotropic under
523 confinement. Statistical comparisons were performed in R using group-wise ANOVA and Kruskal–
524 Wallis tests.

525

526 *scRNAseq*

527 PIPseeker v1.0.0 (Fluent Biosciences) was used to generate single cell matrix, barcode and
528 features for each sample against Hg38 (human). Separate contig for GFP cDNAs was added to
529 the genomes to detect malignant cells expressing a reporter. Cell calling, qc (including doublets
530 removal) and clustering were done using Seurat5[84]. Melanoma cell states were assigned based
531 on the score of previously established signatures[39, 85] using AUCell[86].

532

533 *scATAC*

534 The complete processing of fastq from alignment to single cell ATAC peak calling was performed
535 using cellranger-atac-2.1.0 (https://github.com/10XGenomics/cellranger-atac). Next, scATACseq
536 cellranger matrix was processed using Signac[87] to analyze the overall ATAC distribution around
537 TSS, fragments length, number of peaks per cell. Given that, cells with at least 100-3000
538 fragments, a blacklist ratio < 0.4, a nucleosome signal < 2 and a TSS enrichment > 1 were retained
539 for downstream analysis. Malignant states were assigned to scATACseq object using Seurat5
540 FindTransferAnchors function and the scRNAseq matched object as a reference. Cell barcodes
541 passing the qc and belonging to the assigned states were used to filter the paired fastq files which
542 were then processed using the HiC analysis described above.

543

544 *CRISPR/Cas9 screen*

545 sgRNAs counts and dropout enrichment analysis comparing t0 with t21 were conducted using
546 MAGeCK (v0.5.9.5)[88].
547
548 *RNAseq*
549 Fastq were trimmed and evaluated for qc using TrimGalore (0.6.6) and fastqc (0.11.7). Then,
550 trimmed fastq were aligned to Hg38 human genome and annotated using STAR (2.7.7a)[89] using
551 –quantMode TranscriptomeSAM GeneCounts and –sjdbGTFfile GENCODEv44. Using R (4.4.3),
552 ReadsPerGene.out.tab were combined in a single table using data.table and processed for
553 normalization and differential expression analysis using respectively edgeR[90] and DESeq2[83].
554 Transcript per million (TPM) gene expression normalization was performed with rsem[91] using
555 Aligned.toTranscriptome.out.bam from STAR alignment as input.
556
557 *Methylation*
558 Raw IDAT files with 853,307 probes were imported and normalized in several consecutive steps
559 using *SeSAMe* (version 1.12.9)[92]. A signal intensity-associated P-value was calculated based on
560 out-of-band array hybridization (*pOOBAH*) and a cutoff of 0.05 was imposed. Background signal
561 and dye-bias were corrected with *noob* and *dyeBiasCorr,* respectively. The methylation level of
562 individual CpG sites was determined by calculating the beta (β) value, defined as the ratio of the
563 fluorescent signal from the methylated allele to the sum of the fluorescent signals of both the
564 methylated and unmethylated alleles. β values range from 0 (completely unmethylated) to 1.0
565 (fully methylated). β values were calculated using *getBetas.* Next, HM450 Hg38 probe manifest
566 was downloaded from TCGAbiolinks[93] and filtered for blacklisted regions. Genomic βvalues of
567 each cell line were then inferred at bed regions of interests using GenomicRanges[94]. Analysis
568 was conducted using R (4.4.1).
569
570 **Mouse experiments**

571 12-273BM GFPLuc cell derived xenografts (CDXs) intended for loHiC were generated by injecting
572 $1x10^4$ cells in 50% PBS + 50% Matrigel (Corning, #354234) intradermally into 8 weeks old
573 NOD/SCID/IL2yR- /- male mice (RRID:IMSR_JAX:005557). Tumors were harvested once a
574 ~500mm^3 volume was reached.
575 For metastatic dissemination studies, $1x10^5$ 501mel GFPLuc were resuspended in 100μl PBS
576 and instilled by ultrasound-guided (Visualsonics Vevo 770 Ultrasound Imaging System)
577 intracardiac injection into NOD/SCID/IL2yR- /- male mice 8-12 weeks old. Mouse distress and
578 body weight were monitored over the course of the experiment until the established endpoint of
579 ~20% weight loss. After euthanasia, mice organs were dissected and imaged for GFP
580 fluorescence on a Odissey M (LICORbio). GFP foci and signal intensity were quantified with
581 ImageJ.
582 All mice were purchased from Jackson Laboratory and maintained in the NYULH animal housing
583 according to the ethical compliance established by the NYU Institutional Animal Care and Use
584 Committee (IACUC). All the experiments were approved and conducted under the IACUC
585 protocol # IA16-00051.
586
587 **Data mining public datasets**
588 TCGA SKCM transcriptomic data were downloaded from cBioPortal[95], while SKCM
589 HumanMethylation450 array data were obtained through Bioconductor package TCGAbiolinks.
590 SKCM patients were classified as Melanocytic, Transitory, Neural-Crest and Undifferentiated
591 based on a previous study[51]. Analysis was conducted using R (4.4.1).
592 DepMap Public 25Q2[96] data was downloaded from the official website (https://depmap.org/portal).
593 scRNAseq expression values from melanoma states in human[85] were generated using a Seurat
594 object retrieved from a public drive of the Marine Lab
595 (https://rdr.kuleuven.be/dataset.xhtml?persistentId=doi%3A10.48804/GSAXBN).
596 ATACseq generated in TCGA tumors was retrieved from XenaBrowser[97].

H3K27ac Hi-ChIP ValidPairs derived from TCGA tumors[98] were downloaded from the NCI repository (https://gdc.cancer.gov/about-data/publications/TCGA-HiChIP-2024).

Data and Code Availability

Supplementary data, raw data and the code to process the data generated in this work will be available in Gene Expression Omnibus and in a dedicated Github link after peer reviewed publication.

604 **Results**

605 **Melanoma states exhibit distinct chromatin diffusion, density and domain maturation**

606 At the nanoscale level (~10nm), super-resolution imaging has revealed that chromatin is
607 organized into CPDs, whose functions are determined by size (50-200nm) and packing scaling
608 (D_n), which we previously showed influence the probability of a cell to adopt a certain
609 transcriptional state and nuclear physical properties[16, 62,99]. To investigate potential differences in
610 CPDs across melanoma cell states as a measure of their nuclear physical properties, we
611 performed high-resolution imaging on a panel of melanoma cell lines representing three main
612 phenotypic states: melanocytic (MEL, n = 4), intermediate (INT, n = 3), mesenchymal (MES, n =
613 4), and of melanocytic cells upon MITF silencing (siMS, n = 2) vs. non-targeting control (siNTC)
614 (**Fig. 1a**). Given that MITF directly regulates SOX10, siMS simultaneously abrogates the
615 expression of both master regulators of melanocytic identity, and we tested whether their
616 concomitant silencing elicits nuclear 3D changes. Partial Wave Spectroscopy (PWS) showed that
617 MES cells exhibit lower CPD scaling (measured as D_n) and more chromatin diffusion (measured
618 as D_e) than MEL cells, changes that were only partially recapitulated by siMS (**Fig. 1b**). As
619 expected, INT cells displayed intermediate values between MEL and MES (**Fig. 1b**). To
620 investigate if these differences were also observed in patient tissues, we integrated PWS with
621 Opal multiplexed immunofluorescence (mIF) staining for melanoma cells (S100B+) in melanocytic
622 (MITF+SOX10+) and mesenchymal (AXL, p-EGFR, TCF4) states in a patient tissue microarray
623 (TMA) (**Fig. 1c**) containing cores representative of 20 unique primary melanoma cells
624 (**Supplemental Table 1**). Following MEL and MES cell identification within the TMA (**Fig. 1d**,
625 **Supp Fig. 1a**), melanoma cells classified as MES-like showed decreased CPD scaling compared
626 to MEL-like cells (**Fig. 1e**) suggesting that CPD properties within melanoma cell states are also
627 found in vivo.

628 Heterochromatin and euchromatin have been previously linked to higher and lower mechanical
629 stiffness, respectively[100]. CPD maturation relies on H3K9me3 heterochromatin accelerating
630 packing in the CPD core, while euchromatin, characterized by higher H3K27ac, stabilizes the
631 peripheral CPD zone[101]. To gain more insight into CPD maturation related to cell states, we
632 performed sSMLM for H3K9me3 and H3K27ac in our panel of cell lines. In line with our
633 hypothesis, CPD maturation is reduced in MES cells, as indicated by a significant decrease in
634 H3K9me3-positive CPD size and number relative to MEL cells (**Fig. 1f-g**, **Supp Fig. 1b**), findings
635 further supported by a global genome-wide loss of H3K9me3 by ChIP-seq (**Fig. 1h**). No significant
636 differences were observed in H3K27ac by sSMLM (**Fig. 1g**, **Supp Fig.1b**), ChIP-seq (**Supp Fig.**
637 **1c**) nor upon siMS (**Supp Fig. 1d-e**).

638 Altogether, we demonstrate that MES cells are characterized by increased chromatin diffusion
639 and reduced chromatin density, explained by a reduction in CPD number, size, and maturation,
640 as well as global loss of the H3K9me3 mark, suggesting decreased nuclear stiffness. These
641 differences are only partially mimicked by MITF and SOX10 silencing (siMS), suggesting that
642 additional mechanisms are required to fully recapitulate the nuclear topology and biophysical
643 properties of MES cells during phenotype switching.

644

645 **Inactive compartments and heterochromatin are reshaped during melanoma phenotypic**
646 **switch.**

647 The genome has two major, micron-sized spatial compartments, A and B, associated with active
648 and inactive chromatin respectively[102, 103] within which CPDs are embedded [16]. Using Cooltools[76],
649 we examined melanoma cell lines by sub-chromosomal compartments A and B, further validated
650 by integrating H3K27ac and H3K9me3 ChIPseq, ATACseq, and RNAseq in our panel of cell lines.
651 As expected, A-type compartments are enriched for H3K27ac, ATAC, and RNA signal compared

652 to B compartments, which instead are enriched in H3K9me3 (**Supp Fig. 2a**). To identify state-
653 specific changes in A and B compartments, we performed one minus cosine similarity Kmeans
654 clustering and found a subset of A compartments specific to each phenotype (MEL and MES; **Fig.**
655 **2a**). Although no change in the global proportion of A and B compartments was observed across
656 states or upon siMS (**Supp. Fig. 2b**), saddle *cis* compartment quantification shows an increase
657 in B-to-B interactions in INT, MES, and siMS cells relative to MEL and siNTC, respectively (**Fig.**
658 **2b-c**). No significant differences were found across *trans* compartments interactions (**Supp Fig.**
659 **2c-d).** We analyzed compartment switching from A-to-B and B-to-A between states using a
660 recently published model[19]. Consistent with a switch, epigenetic and transcriptomics marks were
661 found significantly changed from A-to-B and B-to-A comparing MEL, INT and MES, but not in siMS
662 (**Supp Fig. 2e**). We found < 400 compartment switches between MEL and INT, while almost 2000
663 compartments switched between MEL and MES, predominantly from B-to-A which is triggered as
664 well by siMS (**Fig. 2d**). This is in line with the observed decrease in H3K9me3 (**Fig. 1h-i**) and
665 CPDs maturation by sSMLM (**Fig. 1f-g**). In line with our previous observation of decreased
666 H3K9me3 from MEL to MES, our 3D chromatin data indicate that the melanoma phenotypic
667 transition from MEL to INT and MES is marked by a B-to-A compartment switch, mimicked by
668 siMS.

669

670 **MES cells have a reduced number of topologically associated domains.**

671 To further interrogate 3D chromatin changes associated to cell states, we examined the number,
672 size and distribution of TADs (contact hubs of genes, promoters, and enhancers) and quantified
673 insulation scores. We found MES cell lines have significantly fewer (**Fig. 3a***, top*), larger (**Fig. 3a***,*
674 *bottom*) TADs than MEL and INT cell lines. However, MITF and SOX silencing (siMS) did not
675 impact TAD size or number (**Fig. 3a**). Next, TAD activity was evaluated by first averaging the TAD
676 boundary strength, measured by insulation score. MES cells showed an overall decrease in

677 insulation and average CTCF occupancy at MEL and INT TADs boundaries (**Fig. 3b, Supp. Fig.**
678 **3a-b**), whereas siMS display only decreased CTCF binding at boundaries but no change in
679 insulation (**Supp. Fig. 3c**). TAD contact frequency was measured using Aggregate Topological
680 Analysis (ATA), which revealed a global increase of contacts in the inter-TAD surroundings in INT
681 and MES cells (**Fig. 3c**). In parallel, we observed significantly more inter-TAD contacts between
682 +1, +2 and +3 neighbor TADs in INT and MES cells than in MEL cells (**Fig. 3d**). siMS had no
683 effect on intra and inter-TADs contacts (**Supp. Fig. 3d-e**).

684 Next, we identified loops and filtered for structural loops occupied by CTCF at both anchors.
685 Notably, INT cells have the highest number of loops compared to other states, while siMS
686 significantly increased the number of loops relative to siNTC (**Fig. 3e**). Similarly to TADs'
687 boundaries, CTCF occupancy at loops' anchors is reduced in MES, INT and siMS cells (**Fig. 3f,**
688 **Supp Fig. 3f**). Aggregate Peak Analysis (APA) shows an overall enrichment of contacts at the
689 loops' foreground (#contacts foreground - #contacts background) of the corresponding state,
690 except for INT cells that have higher activity, mimicked by siMS cells compared to siNTC (**Fig. 3g,**
691 **Supp. Fig. 3g**).

692 Finally, we intersected boundaries and loop anchors to identify unique TADs and loops across
693 states and in siNTC vs siMS (**Supp. Fig. 3h**), and cross-referenced them with differentially
694 expressed genes (DEGs) identified by RNAseq (**Fig. 3h**, **Supp. Fig. 3i, Supplemental Table 2**).
695 Remarkably, only a modest fraction of state-specific TADs were found associated to DEGs for all
696 states and siMS; i.e., only 1-10% of state-specific TADs result in DEGs (**Fig. 3i**, *left*). Similarly,
697 structural loops were poorly associated to DEGs; except for siNTC, siMS and MEL, with ~20-30%
698 of specific loops resulting in DEGs (**Fig. 3i**, *right*). This indicates that differences in TAD and loop
699 activity between states are disproportional to the changes in gene expression—particularly in
700 MES cells, suggesting the possibility that changes in chromatin structure during the MES-to-MEL
701 phenotypic transition are not just responsible for gene expression changes but may confer some

702 other advantage to MEL cells.

703 In sum, melanoma dedifferentiation from MEL to MES is associated with enlarged domains and
704 increased inter-TAD communications, in line with potentially enhanced nuclear and chromatin
705 flexibility. Intermediate (INT) cells present multi-state loops and thus an overall higher number of
706 loops, suggesting a 'poised' 3D chromatin state, which is in part recapitulated by siMS.

707

708 **State-specific chromatin architecture features are conserved *in vivo*.**

709 We have shown that melanoma phenotypic states display specific 3D chromatin architectures that
710 correlate with nuclear physical properties, irrespective of mutant drivers (i.e., BRAF, NRAS). To
711 complement these *in vitro* findings, we asked if melanoma states adopt similar state-specific 3D
712 chromatin architecture *in vivo* using: i) scRNAseq combined with loHiC and ii) bulk HiC on
713 chromatin from FFPE specimens from melanoma patients. We performed loHiC on a cell-derived
714 xenograft (CDX) from a patient-derived melanoma brain metastasis short term culture (12-
715 273BM) [104, 105], which was able to recapitulate the intra-tumor heterogeneity observed in clinical
716 specimens. MEL and MES states were identified by scRNAseq through Seurat and integrated into
717 the loHiC Signac clusters using Seurat bridge integration[84] (**Fig. 4a, Supp. Fig. 4a**). Next, we
718 performed pseudo-bulk HiC analysis on the MEL and MES clusters for which we obtained a good,
719 genome-wide HiC contact coverage (**Supp. Fig. 4b**), and confirmed their malignant status using
720 copy number variation analysis (**Supp. Fig. 4c**). Remarkably, we validated most of our in vitro
721 observations, such as increase in BB compartment interactions (**Fig. 4b, Supp. Fig. 4d**), fewer
722 and larger TADs (**Fig. 4c**), weaker insulation (**Fig. 4d**) and decreased intra-TAD contacts in MES
723 vs MEL cell states (**Supp. Fig. 4e**). Similarly, bulk HiC in a small cohort of patients' FFPE tumor
724 samples broadly classified as MEL or MES based on histopathological characteristics
725 (**Supplemental Table 3**) showed a trend to a reduction in the number of TADs in MES tumors

726 (**Fig. 4e**). Overall, these data indicate that state-specific 3D chromatin features are not an artifact
727 of in vitro culture but an actual feature of melanoma tumors.
728
729 **Compression during migration induces a MES-like rewiring of nuclear architecture in MEL**
730 **cells, suppresses heterochromatin levels, and enhances their metastatic potential.**
731 While mechanical forces are known to modulate chromatin accessibility[31, 32,33] and viceversa[25, 100,
732 106-108], the reciprocal influence of 3D chromatin conformation on nuclear flexibility in the context of
733 phenotype switching is poorly understood. We have shown that MES cells, compared to MEL
734 cells, possess a more 'relaxed' nuclear architecture, characterized by a lower number and less
735 mature of CPDs **(Fig. 1f-g**), B-to-A compartment switching (**Fig. 2d**), fewer number of TADs with
736 weaker insulation (**Fig. 3a-b**), and reduced heterochromatin (**Fig. 1g-i**). We hypothesized that this
737 'loose' nuclear conformation allows MES cells to better withstand the mechanical stress of
738 invasion or intra/extravasation, and that reduced physical constriction can in turn remodel the 3D
739 genome towards a pro-metastatic state.
740 To determine this, we integrated HiC, H3K27ac, and H3K9me3 profiles to model chromosome 1
741 chromatin as a Hamiltonian coarse-grained polymer bead chain using Polychrom (Open2C).
742 Here, we simulate angle bending upon artificial scaled compression forces to measure stiffness
743 and cost of motion of the polymer. The radius of gyration (Rg) measures the extension and
744 compaction capacity: stiffer regions will adopt extended and rigid conformations increasing Rg,
745 while softer regions can collapse reducing Rg and additionally facilitate *cis*-long interactions
746 (**Supp. Fig. 5a**). In line with our hypothesis, our simulation predicts that MES cells have lower
747 TAD and chromosome stiffness (**Fig. 5a),** as well as reduced energy cost upon simulated
748 constriction and a trend to increased deformability (**Fig. 5b**, **Supp. Fig. 5b**). To experimentally
749 prove this finding, MEL and MES cells were seeded in 3μm-pores transwells for 72hrs in complete
750 media to allow cells to migrate and constrict spontaneously. Next, both non-migrated (Pre = on
751 top side of the transwell) and migrated (Post = on lower side of the transwell) cells were processed

752 for HiC, RNAseq, CUT&Tag (H3K27ac, CTCF and H3K9me3), and ATACseq. Post-migration,
753 MEL cells were associated with gained MES-like features such as lower melanocytic gene
754 expression (i.e., MITF, SOX10; **Fig. 5c, Supp. Fig. 5c**) reduced H3K9me3 levels (**Fig. 5c-d**),
755 increased BB compartments interactions (**Fig. 5e, Supp. Fig. 5d-e**), fewer TADs (**Fig. 5f**), and
756 decreased insulation and CTCF binding at TAD boundaries (**Fig. 5g**In contrast, chromatin and
757 gene expression of MES cells were only modestly affected (i.e., EGFR, AXL; **Fig. 5c**), except for
758 an increased melanoma mesenchymal signature, as if migration 'exacerbates' MES cells identity
759 (**Supp. Fig. 5f**).
760 Polychrom simulation in Pre and Post cells predicted a significant decrease in stiffness in Post
761 MEL relative to Pre MEL, but not in Post MES cells relative to its Pre counterpart (**Fig. 5h**).
762 Consistent with this finding, CPD scaling (D_n) measured by PWS was significantly reduced in Post
763 cells, particularly in MEL cells (**Fig. 5i**, **Supp Fig. 5g**). In parallel, MEL Post cells displayed a
764 significant reduction in mature large H3K9me3 CPDs and a concomitant increase in small ones
765 (**Fig. 5j**) together with a global decrease in H3K9me3 by sSMLM (**Fig. 5k**) which were not
766 observed in MES Post cells (**Supp Fig. 5h**). While constriction did not change their proliferative
767 capacity (**Supp. Fig. 5i**), Post MEL cells exhibited increased metastatic potential to the liver upon
768 intracardiac injection relative to their Pre counterparts (**Fig. 5l, Supp. Fig. 5j**).
769 Next, we tested whether Post cells were a product of selection of a pre-existing subpopulation in
770 the initial culture, or whether physical constriction during migration actively results in cells with
771 Post features. To do that, we infected MEL cells with a doxycycline inducible CBX5-GFP construct
772 at 0.3 MOI (~ 0.3 plasmid per cell) as a reporter of H3K9me3 content within the cells. Confirming
773 the value of this construct as a marker of heterochromatin, we observed increased H3K9me3
774 levels in FACS sorted CBX5-GFP^{High} cells compared to CBX5-GFP^{Low}, and a decrease of these
775 markers upon post migration (**Fig. 5m**). Flow cytometry on Pre and Post CBX5-GFP^{High} cells
776 showed the emergence of a CBX5-GFP^{Low} subpopulation Post migration (**Fig. 5n**). These data

777 suggest that physical confinement during migration does not passively select but *actively* triggers
778 a H3K9me3 low subpopulation.
779 We further tested whether reducing H3K9me3 global content in MEL cells is sufficient to increase
780 nuclear flexibility and cell migration observed in MES cells. Only 12-24hrs of treatment with the
781 histone methyltransferase (HMT) SUV39H1/2 inhibitor, Chaetocin increased cell migration (**Fig.**
782 **5o, Supp Fig. 5k**) and reduced H3K9me3 without affecting the levels of melanocytic markers
783 such as MITF and SOX10 (**Supp Fig. 5l**). In line with our hypothesis of heterochromatin being a
784 physical barrier to migratory constriction, a short pulse of Chaetocin (24hrs) was sufficient to
785 significantly decrease D_n as a proxy of nuclear stiffness (**Fig. 5p**), and sorted CBX5-GFP^{Low} (low
786 H3K9me3) cells displayed higher migratory capacity than CBX5-GFP^{High} (high H3K9me3) cells
787 relative to their non-migrated counterpart (PreM) (**Fig. 5q**).
788 These data indicate that MEL cells gain MES features as they intravasate and that treatments
789 that make MEL 3D chromatin ressemble the MES state are sufficient to confer increased
790 migratory potential before changes in gene expression are observed.
791
792 **CTCF genomic occupancy reveals a transcriptional activator function specific to**
793 **mesenchymal cells.**
794 We observed that MES cells have a global reduction of CTCF at TAD boundaries compared to
795 MEL cells (**Fig. 3b**), which is in line with an overall CTCF protein decrease in MES (**Supp. Fig.**
796 **6a**). However, mean CTCF occupancy at TSSs is higher in MES compared to MEL and INT cells
797 (**Fig. 6a**), suggesting a CTCF relocation from insulators to regulatory elements. To test this
798 hypothesis, we first identified all active candidate *cis* regulatory elements (cCREs) by integrating
799 ATACseq, H3K27ac ChIPseq, RNAseq and HiC using the Activity-by-Contact (ABC) model[82] in
800 all cell lines. Next, we intersected CTCF peaks with the ABCmodel identified cCREs[82] to define
801 the proportion of CTCF binding at structural-like (ABC-) vs. enhancer–promoter (ABC+) regions.

802 This analysis demonstrated a global increase of CTCF binding to cCRE in MES and siMS cells
803 compared to MEL cells (**Fig. 6b**). In line with the reduced insulator function in MES cells, HiC
804 pileup map analysis at CTCF peaks shows a strong increase in global contacts as well as between
805 adjacent 5' and 3' regions (span in graph) in MES cells, indicating a reduced level of conventional
806 insulation activity compared to MEL, INT and siMS cells (**Fig. 6c-d, Supp. Fig. 6b**). Conversely,
807 differential binding analysis of CTCF between MEL and MES cells (**Supp. Fig. 6c**) showed
808 increased occupancy of MES CTCF at cCREs relative to structural-like (CTCF-only) anchors (**Fig.**
809 **6e**). These MES-specific CTCF bound regions are co-occupied by MES TFs such as TEAD4 and
810 FOSL2 (**Fig. 6f**) and associated mostly with enhancers (n = 1,479 ABC cCREs) (**Supp. Fig. 6d**),
811 suggesting that CTCF may exert a direct gene regulatory function in concert with AP1/TEADs in
812 MES cells. Accordingly, CTCF and AP1/TEADs co-immunoprecipitated (**Fig. 6g**), further
813 supporting these TFs binding as part of CTCF complexes. Moreover, TF motif footprint analysis
814 demonstrates a significant increase in CTCF motif accessibility in MES and siMS compared to
815 MEL and siNTC (MEL vs MES, Lg_2FC = -0.35251; siNTC vs siMS, Lg_2FC = -0.40685) (**Fig. 6h**).
816 To identify CTCF regulated genes in MES cells, we looked at the activity and genes directly
817 contacted by the ABC cCREs overlapping with CTCF MES peaks (**Supp Fig. 6e**), finding 5,081
818 cCRE-associated genes (**Supplemental Table 4**). We confirmed that putative CTCF-regulated
819 MES genes are upregulated in MES cell lines[51] and patient samples[85] relative to MEL cells (**Supp.**
820 **Fig. 6f-g**). To determine if MES genes depend on CTCF, we performed a brief knockdown of
821 CTCF (24hrs) using siRNA followed by RNA-seq in MM099 (MES) (**Fig. 6i**, **Supp. Fig. 6h**).
822 Notably, we found a significant overlap (n = 852) between CTCF ABC-predicted contacted genes
823 (n= 5,081) and siRNA differentially expressed genes (n = 4,037) (**Supp. Fig. 6i**). Strikingly, CTCF
824 depletion leads to a significant increase in MEL and decrease in MES gene signatures[53] (**Fig. 6j**),
825 and siCTCF upregulated and downregulated genes are found significantly associated to MEL and
826 MES states respectively in patients (**Supp. Fig. 6j**), suggesting that CTCF is indeed required to
827 maintain MES identity.

828 Altogether, our data suggest that CTCF partially relocates from TAD boundaries to enhancer–
829 promoter regions in MES cells, where —together with MES TFs AP1/TEADs— it may directly
830 regulate a subset of MES relevant GRNs. Therefore, melanoma state transitions can involve
831 changes in CTCF deposition and activity.

832

833 **State-specific chromatin hubs are highly active in mesenchymal cells, functionally**
834 **involved in invasion and associated with patients' survival.**

835 We demonstrated that melanoma cells states have profound differences in nuclear architecture
836 irrespective of the mutational driver and burden (i.e., CNVs, SVs). These differences are
837 associated with changes in both the transcriptional output and physical properties (i.e., stiffness)
838 tuning metastatic potential. We hypothesized that MES cell increased chromatin flexibility and
839 inter-domain contacts may favor an increase in cis-CREs (cCREs) connectivity and the formation
840 of new chromatin hubs. To examine global connectivity, valid paired interactions were divided in
841 cis-short (distance < 20 Kb), cis-long (distance > 20 Kb), and trans (inter-chromosomal contacts).
842 To account for DNA mutations/arrangements, we ran EagleC[109] and HiNT[78] to detect structural
843 variants (SVs) and copy number variations (CNVs) respectively; valid DNA pairs spanning SVs
844 and CNVs breakpoints were excluded. No significant variations in the number of CNVs and SVs
845 were detected among states and upon siMS (**Supp Fig. 7a-b**).

846 In line with our hypothesis, MES cells have a significant increase in cis-long range interactions
847 compared to INT and MEL cells, and a reduction in *cis*-short range contacts (**Fig. 7a**). However,
848 siMS treatment does not result in significant variations in global contacts (**Supp. Fig. 7c**).
849 Moreover, HiC pileup map analysis at global TSS shows an augmented connectivity at promoters
850 in MES cells (**Fig. 7b**), an indication of enhanced regulatory activity, which is not mimicked by
851 siMS (**Supp. Fig. 7d**). Next, to map the global cCRE connectivity in melanoma states at the
852 granular level, we applied the previously described ABC-model[82] to our panel of cell lines, which

853 identified 215,858 cCREs after excluding self-promoter contacts and retaining cCREs with an
854 ABCscore ≥ 0.02 (**Supplemental Table 5**).

855 To identify state-specific cCREs, we performed DESeq2 analysis of cCREs based on the
856 ABCscore among the states to identify 11,581 MEL-specific cCRE, 3,987 INT-specific cCRE and
857 29,189 MES-specific cCRE (**Fig. 7c, Supp. Fig. 7e**). Within the state-specific cCRE, we identified
858 chromatin hubs, defined as cCREs able to connect multiple genes concurrently. We ranked
859 cCREs based on the number of genes contacted, the sum of ABCscore provided and the number
860 of contacted genes with a TPM expression ≥ of 1, identifying hubs specific of each state (**Fig. 7d,**
861 **Supp. Fig. 7f**, **Supplemental Table 6**). In line with our hypothesis, MES cells show the greatest
862 number of hubs compared to INT and MEL. State-specific hub anchors display significantly lower
863 DNA methylation in the corresponding state, suggesting they are epigenetically active (**Fig. 7e**).
864 Reduced DNA methylation was also observed at MES hubs in MES-like specimens of both
865 primary and metastatic melanoma (**Fig. 7f, Supp Fig. 7g**) and this reduction can be detected in
866 patients' samples[98] (**Fig. 7g, Supp. Fig. 7h-i**), suggesting that these hubs are active in patients'
867 tumors and from early tumor stages. To further support the in vivo conservation values of the
868 identified hubs, 12-273BM derived xenograft cells processed with loHiC (**Fig. 4a**) show ATAC
869 accessibility enrichment at hubs of the corresponding identified states (**Fig. 7h**). Next, DNA
870 footprinting of hub anchors revealed a significant enrichment in AP1/TEAD transcription factors
871 as well as CTCF (**Fig. 7i, Supp. Fig 7j, Supplemental Table 7**). Accordingly, MES hub
872 connectivity and activity are significantly affected by CTCF silencing (**Fig. 7j, Supp. Fig. 7k**),
873 further supporting CTCF-AP1/TEAD complexes as key regulators of MES specific GRNs.

874 Finally, we assessed the functional role of MES chromatin hubs by a drop-out screen using a
875 custom pooled CRISPR interference library against 43 top MES hubs. To test which chromatin
876 hubs are important for MES identity and migratory capacity, MES cells were transduced with a
877 doxycycline-inducible dCas9-KRAB-MeCP2 and the CRISPRi library and seeded for migration on

878 3.0μm pore transwell inserts. Post-migration cells were collected and re-seeded on a transwell
879 assay multiple times. Twenty-one days after consecutive migration cycles, DNA sequencing
880 revealed two hubs being significantly depleted by all 5 independent sgRNAs/hub (p-value<0.05)
881 compared to time zero (t0) (**Fig. 7k**). Strikingly, ATAC-seq accessibility of these two hubs is
882 significantly associated with shorter patient survival across various cancer types[110] (**Fig. 7l**).
883 Together, our results precisely map the most active cCREs in the main melanoma phenotypic
884 states. Particularly in MES cells, it revealed the bivalent function of chromatin architecture in which
885 CTCF gets recruited at hubs and cCREs of genes involved in MES identity at the expense of
886 domains' boundaries, simultaneously promoting a more flexible nuclear architecture which favors
887 cell migration and intravasation.
888

889 **Discussion**

890 State transitions and phenotypic plasticity have been linked to cancer metastasis and therapeutic
891 resistance. In particular, the acquisition of a de-differentiated, mesenchymal identity is a common
892 feature across tumors of various origins, such as carcinomas[111, 112], glioblastoma[113] or
893 melanoma[114]. To date, most studies have attributed associated transcriptional programs with
894 confer cancer cells with a selective advantage under multiple stressors as they invade, colonize
895 distal tissues, or survive treatment. While previous studies have been limited to a two-dimensional
896 analysis of state-specific epigenomes, we are the first to dissect the contribution of higher order
897 chromatin structures and nuclear architecture to mesenchymal (MES) identity, using melanoma
898 as a paradigmatic model of metastasis. Contrary to differentiated MEL state, we demonstrate that
899 the MES state encompasses a loose chromatin architecture and nuclear conformation which
900 supports not just a distinct transcriptional and epigenetic program but mechanical properties such
901 as nuclear deformability as an adaptive response to migratory constriction and metastasis. MES
902 nuclear topology results in part from a relocation of CTCF from TADs boundaries to MES-specific
903 chromatin hubs and cCREs, and enhanced cis-long interactions (larger TADs, more inter-TADs

904 contacts) and reduced H3K9me3 constitutive heterochromatin (small, immature CPDs) relative to
905 differentiated, MEL cells. MES cells represent an intriguing, de-differentiated cancer cell state
906 conserved across multiple cancer types[115] . Our data suggests that multiple tumor types from
907 various cellular origin may similarly converge from a differentiated state, with a 'rigid' chromatin
908 architecture locked by lineage-specific GRNs, to a pan-cancer undifferentiated (MEL-like) state,
909 broadly characterized by loose chromatin, nuclear elasticity and enhanced deformation upon
910 constriction, as we demonstrate in melanoma.
911 Supporting this model, silencing of the master melanocytic TFs MITF and SOX10 GRNs can
912 'push' melanoma cells toward an intermediate (INT-like) state as previously reported[46], but this is
913 insufficient in allowing cells to adopt MES nuclear architecture and mechanical features, which
914 suggests the requirement of additional stimuli. We showed that upon physical constriction such
915 as the one experienced during migration, melanocytic cells shift to a MES-like nuclear molecular
916 conformation, characterized by reduced CTCF occupancy and insulation at TADs' boundaries,
917 lower heterochromatin and stiffness, and decreased MITF and SOX10 levels, which confers them
918 with enhanced metastatic potential. This bidirectional crosstalk between 3D chromatin and
919 nuclear compression links for the first time epigenetic features, gene expression programs and
920 mechanical properties to cancer phenotypic plasticity and metastasis.
921 Traditionally, cancer cell phenotypes have been simply defined by differential transcriptional
922 states[116], where lack of genetic drivers indicates that, at least in part, they are epigenetically
923 driven[117, 118]. However, the role of epigenetic regulatory mechanisms in defining these
924 transcriptional states remains poorly understood, partly due to the limited application of in vivo
925 epigenetic technologies at single-cell resolution (mostly ATACseq)[119]. Although some state-
926 specific gene' functions clearly map to a corresponding state (e.g., ATF4 in stress response, E2Fs
927 in mitosis, MMPs in invasion, PD-L1 in immune evasion)[43], many others are harder to interpret
928 because their expression overlaps across states[116]. Instead, these overlapping genes may reflect
929 indirect downstream adaptations to upstream epigenetic changes, such as alterations in

930 chromatin architecture, rather than representing state-specific functional programs. In support of
931 this, we generated the first atlas of melanoma cell state regulatory element (n=215,858) activity
932 and their connections with other genes, which can inform future cancer epigenetic-related work.
933 Here, melanoma states exhibit profound, global differences in 3D chromatin organization that are
934 not explained solely by differential gene expression[120], but also by distinct nuclear organization
935 and physical properties *in vitro* and *in vivo*. These results contribute to the ongoing debate on the
936 role of chromatin architecture in global versus gene-specific transcriptional regulation[121]. Our
937 findings support a model of converging, transcription-dependent and independent roles of
938 chromatin architecture, exemplified by the repurposing of CTCF as both a structural and
939 transcription factor, and the emergence of chromatin hubs as regulatory network organizers.
940 Untangling CTCF gene regulatory function is demanding due to its polyhedric role as activator,
941 repressor and genome organization protein[122], as shown in mouse embryonic stem cells where it
942 acts as activator of a subset of genes together with its paralog CTCFL[123]. In cancer cells, CTCF
943 can shift from a structural to a gene-regulatory role, as seen in MES cells where it binds less to
944 insulators and more to CREs, promoting *cis*-long interactions, inter-TAD connectivity and
945 chromatin hubs formation, regulatory headquarters required for the expression of cancer cell
946 identity genes[23, 24, 57]. In agreement, a brief depletion of CTCF affects MES hub connectivity and
947 their target genes, and our CRISPRi screening revealed a previously unreported role of hubs in
948 controlling MES cells' biology. The two identified hubs control 72 genes involved in cell
949 proliferation (i.e., NCAPGP2, CTDP1, PARD6G)[124-126], migration (i.e., NFATC1, TJP1)[127, 128] and
950 survival (UBE3A)[129]. Yet, it is unclear if chromatin hubs solely control gene expression or also
951 nuclear flexibility. In fact, although physical constriction is sufficient to reduce CTCF at MEL
952 boundaries, it is insufficient to recruit it at MES CREs and hubs, which may require TF partners[120]
953 such as AP1/TEADs and CTCFL, all of which have been shown to promote a MES state in
954 melanoma[47, 130-132].

955 In addition, we demonstrate that MES cells display a reduced maturation and size of physical
956 CPDs, which directly correlates with mechanical stability. For example, stable mature domains
957 have been shown to lower the probability of blebbing during cell migration, with predominantly
958 'domain-less' chromatin forming the blebs.[34] In addition, mechanical stressors and forces acting
959 on cancer cells are expected to affect CPDs and their encoded transcriptional memory through a
960 selective process favoring immature and smaller CPDs (low H3K9me3) rather than mature (high
961 H3K9me3). Due to their greater steric hindrance, increased crowding upon constriction can
962 convert mature CPDs into immature ones, destabilizing H3K9me3, CBX5 (HP1a)[13, 14, 133] and
963 CTCF insulation which is required to contain heterochromatin nucleation[12]. Cell differentiation
964 requires H3K9me3 deposition to silence lineage unrelated genes expression[134] within mature
965 CPDs to allow transcriptional memory[16, 101]. Therefore, MES cells may represent a phenotypic
966 state in which mechanical confinement, coupled with the loss of lineage-determining GRNs (e.g.,
967 MITF and SOX10 in melanoma), leads to erosion of the transcriptional memory that encodes
968 tumor lineage identity (i.e., the melanocytic-like state), as reflected by CPD immaturity, increased
969 long-range cis contacts, TAD expansion, and reduced CTCF-mediated insulation. Based on this
970 model, cells in the MES state may lose plasticity by efficiently propagating a stabilized epigenetic
971 and 3D chromatin configuration through cell division, resulting in maintenance of MES identity
972 during tumor progression. This is consistent with observations in glioblastoma, where the MES
973 phenotype is highly heritable across cell generations[7]. Similarly, while MEL to MES
974 dedifferentiation has been extensively reported[51, 135], there is little to no evidence for the opposite
975 process (i.e., from a de-differentiated to a differentiated state).
976 Finally, our study provides the first evidence of a direct link between 3D chromatin and nuclear
977 biophysical properties and cancer cell states in actual tumor samples. By combining state-of-the-
978 art bulk and single cell high-resolution microscopy (PWS, sSMLM), epigenomics and molecular
979 and cell biology techniques, we demonstrate their potential for clinical translation. For instance,
980 we integrate PWS and multiplex IF (Opal) staining -which are relatively inexpensive and rapid

981 techniques- on a curated TMA containing. Our future work will integrate 3D genome and nuclear-
982 property data across larger cohorts to train AI models on H&E images, enabling machine-
983 learning–based identification of cancer cell states and linking intra-tumor heterogeneity to patient
984 outcomes. Our findings identify nuclear chromatin organization as an essential driver of cancer
985 cell plasticity, representing a novel intersection between mechanical properties, epigenetics and
986 gene expression in tumor progression.
987

988 **Acknowledgments**

989 This work was supported by U54CA263001 (E.H. and I.O) and R01CA274100 (E.H.), from
990 NCI/NIH and career awards of the National Cancer Center (NCC), Melanoma Research Alliance
991 (MRA) and Melanoma Research Foundation (MRF) to P.B. We thank the Genomics Technology
992 Center (GTC) particularly Mr. Paul Zappile for supervising all the sequencing, the Preclinical
993 Imaging Core, the Experimental Pathology Core (Dr. Cynthia Loomis and Mr. Gyles Ward for Opal
994 panel optimization) and the Flow Cytometry core, all of which are supported by Cancer Center
995 Support Grant (CCSG) from NCI/NIH to the NYULH Perlmutter Cancer Center (P30CA016087;
996 PI: Alec Kimmelman). V.B. was supported by U54 (CA268084) and L.A. by a K23
997 (1K23DK144661) NIH/NCI awards. This research used resources of the Center for Physical
998 Genomics and Engineering at Northwestern University, and philanthropic support from K. Hudson
999 and R. Goldman, S. Brice and J. Esteve, M. E. Holliday and I. Schneider, the Christina Carinato
1000 Charitable Foundation, and D. Sachs.

1001

1002 **Author contributions**

1003 P.B. and E.H. conceived and design the work. P.B. performed and analyzed most of the omics
1004 experiments (HiC, ChIPseq, ATACseq, loHiC, CUT&Tag, scRNAseq, CRISPR screen,
1005 Methylation, Polychrom model and public datasets mining). V.B, C.D. and L.A. designed and

conceived the microscopy and biophysical experiments, and C.D. and L.A. performed the experiments. K.I.M and N.A. performed PWS and sSMLM imaging, analysis and visualization. J.S. and C.Do provided helpful insights for the HiC analysis. A.F.Y. and P.B. performed the chromatin hubs CRISPR screen and analysis, and *in vivo* mouse experiments. I.A. and S.L. shared the loHiC protocol and S.L. provided analysis support. I.O. and M.I. provided patient data and material under IRB protocol #H10362 and designed the TMA. A.S.M. provide a pathology evaluation of the TMA. T.M. analyzed the TMA staining. S.N.E., D.C. and N.E.T. provided the cell line methylation data. A.R., C.K. and R.S. provided the methylation data of a cohort of primary melanoma of the international consortium InterMEL. S.N.E., D.C., N.E.T., K.D., A.R., C.K., R.S. and E.H. are part of InterMEL. P.B., E.H., C.D., L.A. and V.B. interpret the results. P.B. and E.H. wrote the manuscript with important inputs from C.D., L.A. and V.B. All authors approved and revised the final manuscript.

1019 **Figures**

1020 **Figure 1: Melanoma cell states are characterized by distinguished chromatin nanoscale**
1021 **structures.**

1022 **a.** Biorender illustration of the melanoma cell lines classified into states based on our and previous
1023 studies[45].

1024 **b**. PWS quantification of Chromatin Packing Domain scaling (D_n) and diffusion (D_e) in a large
1025 panel of melanoma cell lines colored as melanocytic (MEL, red), intermediate (INT, grey) and
1026 mesenchymal (MES, green). Each dot represents a single cell, in black is shown the median bar.
1027 One-way ANOVA test p-values are shown and summarized as pairwise comparisons MEL vs
1028 MES.

1029 **c**. Whole slide snapshot of the Opal staining conducted in two TMAs (A-B) for S100B, SOX10,
1030 MITF, AXL and phospho-EGFR (pEGFR). Scale bars are referred to 5mm size.

1031 **d**. Representative MEL-like and MES-like cells identified in two melanoma TMAs by confocal
1032 microscopy using a combination of markers to measure PWS in melanoma cell states.

1033 **e**. Dot plot showing D_n measurements in MEL-like (n=109) and MES-like (n=67) cells in two
1034 melanoma TMAs. Each dot represents a single cell. Student unpaired t-test p-value comparison
1035 is shown.

1036 **f**. Relative H3K9me3 cluster size in different melanoma cell lines representative of MEL, INT,
1037 MES, siNTC and siMS groups. Each dot is the mean measurement in a single cell. One-way
1038 ANOVA test was conducted. Significant p-value summarizing MEL vs MES is shown.

1039 **g**. Representative sSMLM images for H3K9me3 and H3K27ac staining in three different
1040 melanoma cell lines colored based on their state of belonging (MEL = red, INT = grey, MES =
1041 green).

1042 **h**. H3K9me3 ChIP-seq global metaprofile in MEL, INT and MES cells. Each profile is the average
1043 of at least three biological replicates (different cell lines).

1044 **i**. (Left) Immunoblot for different proteins in a large panel of melanoma cell lines marked in red
1045 (MEL), grey (INT) and green (MES). MITF and EGFR are enriched in MEL/INT and MES cells
1046 respectively. (Right) H3K9me3 relative quantification to total histone H3 based on the blot on the
1047 left. Unpaired t-test was performed for pairwise comparisons. P-values are displayed.

1048

1049 **Figure 2: Nuclear compartments switch occurs during phenotype switching.**

1050 **a.** Whole genome *cis* compartments A and B clustering in melanoma cell lines. In red and green
1051 are marked A compartments specific of melanocytic and mesenchymal states respectively. Color
1052 scale represents compartment score z-score normalized by column. Ward hierarchical clustering
1053 dendrogram is shown on the left.

1054 **b**. States, siNTC and siMS *cis* compartments saddle plots. 20% quantile areas at the corners
1055 were measured (as marked by dotted white squared) as representative of more radical
1056 interactions across A and B.

1057 **c**. Group histogram of *cis* AA, BB, and AB:BA interactions in states (left), siNTC and siMS (right).
1058 Two-way ANOVA test was used, p-values are displayed.

1059 **d**. Compartment switch analysis from BA, AB, AA and BB in melanoma states, siNTC and siMS.
1060 Significant switches are shown in black, the number of switch events are displayed in the
1061 corresponding areas.

1062

1063 **Figure 3: Structural domains and loops properties of melanoma cell states.**

1064 **a.** Column dot plot of the number (top) and size (bottom) of TADs identified in melanoma states,
1065 siNTC and siMS. One-way ANOVA significant p-values are shown. Each dot represent a biological
1066 replicate.

1067 **b**. Insulation score (top) and CTCF binding (bottom) profiles of melanoma states compared at
1068 melanocytic, intermediate and mesenchymal TAD boundaries. Summit values are quantified and
1069 statistically compared in the sided column dot plots. One-way ANOVA test p-values are displayed.
1070 Each dot is representative of a biological replicate.

1071 **c**. Aggregate TAD analysis heatmap showing the relative difference in contacts of MES, INT and
1072 siMS cells against MEL/siNTC at melanocytic, intermediate and mesenchymal TADs.

1073 **d**. Bar dot plot quantifying the *cis* interactions in INT and MES cells relative to MEL cells as intra-
1074 TADs (0) and inter-TADs between neighbor TADs (+1, +2, +3). One-way ANOVA test was
1075 conducted independently in each TAD group (0, +1, +2, +3). P-values are shown. Each dot
1076 represent an independent interaction.

1077 **e**. Structural loop quantification in melanoma states (left), siNTC and siMS (right). One-way
1078 ANOVA and paired t-test were conducted for left and right plots respectively. Dots represent
1079 biological replicates.

1080 **f**. CTCF mean genomic occupancy at melanocytic, intermediate and mesenchymal loops' anchors
1081 in melanoma states.

1082 **g**. HiC contacts frequency at loops anchors (foreground) at melanocytic, intermediate and
1083 mesenchymal loops relative to the background (Foreground contacts) in melanoma states, siNTC
1084 and siMS. One-way and paired t-test analysis were performed for melanoma states, and
1085 siNTC/siMS plots respectively. P-values are shown.

1086 **h**. Differentially expressed genes (DEGs) heatmap identified in melanoma states. Color bar
1087 represents z-score of TPM expression normalized by row. **i**. Bar plot quantification of the

1088 percentage of TADs (left) and loops (right) associated with DEGs that overlap with state-specific
1089 TADs and loops respectively.

1090

1091 **Figure 4: Melanoma states 3D chromatin differences are found *in vivo***

1092 **a**. Seurat UMAP representing the bridge integration of melanoma cell states between scRNAseq
1093 (left) and loHiC (right) obtained from a cell derived xenograft (CDX) of 12-273BM short-term
1094 patients' culture.

1095 **b**. cis compartment interactions quantified in MEL and MES states identified in CDX tumors.

1096 **c**. Column dot plot showing the quantification of the number (left) and size (right) of TADs in MEL
1097 and MES states by loHiC.

1098 **d**. Genome-wide insulation score profile at TADs' boundaries in loHiC MEL and MES states.

1099 **e**. TADs' number (left) and size (right) quantified in a small cohort of FFPE MEL (n=3) and MES
1100 (n=4) tumors processed with HiC. Unpaired t-test was conducted and resulted p-values are
1101 shown. Each dot represent a patient sample.

1102

1103 **Figure 5: Nuclear constriction actively rewire 3D chromatin in a state-specific manner.**

1104 **a.** Column dot plot quantification of chromatin stiffness predicted by polychorm in chromosome 1
1105 (left) and the median stiffness per TAD of chromosome 1 (right) in melanoma states and siMS. P-
1106 values obtained from one-way ANOVA study are shown. Each dot is a biological replicate.

1107 **b**. Predicted energy cost of chromosome 1 subjected to a simulated constriction gradient. One-
1108 way ANOVA test was conducted for statistical comparison. Significant p-values are shown.

1109 **c**. Representative immunoblot for multiple targets detected in whole cell protein extracts from
1110 501mel (MEL) and MM099 (MES) Pre and Post migration. ACTB and H3 serves as loading
1111 controls. Relative molecular weights are shown on the right.

1112 **d**. Bigwig comparison between Pre and Post genomic occupancy at chromosome 1 of H3K9me3
1113 and H3K27ac in 501mel and MM099. Tracks are equally scaled spanning a range displayed on
1114 top left.

1115 **e**. Grouped histogram quantification of the 20% quantile *cis* compartments AA, BB, AB:BA
1116 interactions in 501mel and MM099 Pre and Post migration. Brackets are shown to highlight BB
1117 comparison between Pre and Post.

1118 **f**. Quantification of the number (left) and size (right) of TADs in 501mel and MM099, Pre and Post
1119 migration.

1120 **g**. Insulation score (top) and CTCF occupancy (bottom) profiled in Pre and Post cells at TADs
1121 boundaries of 501mel and MM099 cells.

1122 **h**. Stiffness quantification of whole chromosome 1 (left) and median TAD stiffness of chromosome
1123 1 (right) in Pre and Post 501mel and MM099 cells. One-way ANOVA test was conducted.

1124 **i**. D_n measurement by PWS in 501mel and MM099 Pre and Post cells. Unpaired t-test
1125 comparisons between Pre and Post were conducted and significant p-value is shown. Each dot
1126 represents a single cell considered as biological replicate.

1127 **j**. H3K9me3 domain proportion in 501mel Pre and Post cells. Based on their radii size, domains
1128 were classified in small (≤0.55nm), medium (55-80nm) and large (>80nm). Each dot represents
1129 the average of independent measurements in single cells. Chi-square test of independence was
1130 conducted. Summary p-value is shown.

1131 **k**. Representative images captured by sSMLM for H3K9me3 and H3K27ac in 501mel Pre and
1132 Post migration.

1133 **l**. Box dot plot quantification of liver metastasis area (%) derived from NSG animals injected
1134 systemically (intracardiac) with 501mel Pre and Post. Each dot represents a biological replicate.
1135 Unpaired t-test was performed and p-value is shown.

1136 **m**. Immunoblot comparing Pre and Post 501mel$^{CBX5\text{-}GFP}$ whole cell protein extracts carrying low
1137 or high levels of CBX5-GFP. Protein targets and relative molecular weights are shown at left and
1138 right respectively. Vinculin and H3 serve as loading controls.

1139 **n**. CBX5-GFP quantification by flow cytometry (FITC-A) in Pre and Post migration 501mel CBX5-
1140 GFP High. Dotted lines serve as visual reference to appreciate the appearance of low and
1141 decrease of high CBX5-GFP cells after migration. Three biological replicates are shown.

1142 **o**. (Left) Representative image of post migration cells upon DMSO or Chaetocin. (Right) Bar dot
1143 plot quantification of 501mel migratory cells upon DMSO or Chaetocin (5nM) based on crystal
1144 violet staining of transwell. Paired t-test p-value is shown. Each dot represent a biological
1145 replicate, and each replicate is the average of three technical replicates.

1146 **p**. Dot plot quantification of D_n measured by PWS in 501mel cells treated with DMSO (control) or
1147 Chaetocin. Each dot represent a single cell. Mean and standard deviations are shown in red.
1148 Unpaired t-test was performed, p-value is shown.

1149 **q**. Relative cell number of post migratory cells to pre migration of 501mel$^{CBX5\text{-}GFP}$ High and Low.
1150 Each dot is a biological replicate. Paired t-test was conducted, p-value is displayed.

1151

1152 **Figure 6: CTCF is a mesenchymal identity transcriptional regulator.**

1153 **a**. Metaprofile occupancy of CTCF at transcription start sites (TSS) in MEL, INT and MES cells.

1154 **b.** Grouped bar plot representing CTCF occupancy at candidate *cis* regulatory elements (cCRE)
1155 or structural-like (CTCF-only) regions in melanoma states, siNTC and siMS. Each dot represents
1156 a biological replicate.

1157 **c**. Aggregate region analysis at melanocytic, intermediate and mesenchymal CTCF peaks in INT
1158 and MES cells and their comparison against MEL, measured as Log_2 Fold Change of
1159 observed/expected HiC contacts. Span and center areas used for statistical comparisons are
1160 marked by dotted black squares.

1161 **d**. Center and span areas quantification and statistical analysis by one-way ANOVA in MEL,
1162 siNTC, siMS, INT and MES cells at melanocytic, intermediate and mesenchymal CTCF peaks.
1163 Each dot represents a biological replicate.

1164 **e**. Peak annotation of CTCF regions specific of MEL and MES states.

1165 **f**. MITF/SOX10[46] and FOLS2/TEAD4[136] occupancy at CTCF MES-specific regions.

1166 **g**. Immunoblot of CTCF, FOSL1, FOSL2, JUN and pan-TEAD co-immunoprecipitations using
1167 MM099 nuclear insoluble extracts. 1% of input and IgG were used as internal controls. Relative
1168 molecular weight are shown on the right.

1169 **h**. Volcano plots representing the differential binding of transcription factors predicted by TOBIAS
1170 footprint analysis. Colored spots are the significantly enriched motifs in the colored matched
1171 conditions. Some of the motifs are shown.

1172 **i**. siCTCF RNAseq volcano plot of DEGs found downregulated or upregulated in MM099. In red
1173 are the genes statistically significant (adjusted p-value <0.05).

1174 **j**. Gene Set Enrichment Analysis plot of Mesenchymal and Melanocytic Widmer signatures in
1175 MM099 siCTCF. Adjusted p-values and normalized enrichment scores (NES) are shown.

1176

1177 **Figure 7: Mesenchymal cells nuclear organization shape chromatin hubs important for**
1178 **migration and cell identity.**

1179 **a.** Quantification of cis-short (<20Kb), cis-long (>20Kb) and trans HiC contacts by column dot plot
1180 in MEL, INT and MES cell lines. One-way ANOVA test was performed, significant p-values are
1181 shown. Each dot represents a biological replicate.

1182 **b**. (Left) HiC pileup region analysis of genome-wide TSS in INT and MES relative to MEL cells.
1183 (Right) Corresponding quantification at the center of the heatmap marked by the dotted black
1184 square area. Each dot is a biological replicate statistically evaluate by one-way ANOVA.

1185 **c**. Heatmap of the cCRE differentially active in melanoma states. Color scale measure ABCscore
1186 z-score normalized per row.

1187 **d**. Dot plot distribution of differentially active cCRE in MEL (n=11,581), INT (n=3,987) and MES
1188 (n=29,189) cells based on cCRE average sum of ABCscore relative to the number of contacted
1189 genes. Color bar measure the number of genes with a TPM expression ≥1 contacted by each
1190 cCRE.

1191 **e**. Methylation quantification of 500 MES hubs in melanoma cell lines. Methylation levels were
1192 averaged from all 500 hubs and one-way ANOVA test was conducted.

1193 **f**. Bar dot plot showing the average methylation of 500 MES hubs in primary melanoma samples
1194 (n=100) classified as MEL (melanocytic), mixed and NC/MES (neural-crest, mesenchymal). Each
1195 dot represent an independent biological sample, one-way ANOVA p-value comparison MEL vs
1196 NC/MES is shown.

1197 **g**. H3K27ac Hi-ChIP contact aggregate analysis at MES hubs (n=500) in three melanoma patients
1198 from the TCGA consortium generated by Yost et al.[98] and classified in INT based on Tsoi et al.[51].

1199 **h**. Pseudobulk ATACseq enrichment at MEL, INT and MES hubs regions in MEL and MES cells
1200 identified by loHiC in 12-273BM derived xenograft.

1201 **i**. Volcano plot of the differential TF motifs activity in MES vs MEL/INT hubs according to TOBIAS.
1202 Some relevant motifs are shown, in red are the statistically significant motifs found.

1203 **j**. HiC aggregate contact analysis at MES hubs (n=500) in MM099 siNTC and siCTCF.

1204 **k**. Dot plot representing the CRISPR interfering MES hubs functional ranking in MM099 based on
1205 their fold change enrichment from time zero (T0) to 21 days (T21) upon silencing. In red are
1206 marked significantly dropped targets. GAPDH serves as internal positive control.

1207 **l**. Kaplan-Meier showing the overall survival of TCGA patients (n=404) based on their levels of
1208 ATACseq accessibility at two MES hubs found significantly depleted by a CRISPR screen. 50%
1209 quartile was used to segregate high (n=202) vs low (n=202) accessibility. Mantel-Cox test p-
1210 values are shown.

1211

1212 **Supplemental Figure 1:**

1213 **a.** Snapshot captured by confocal microscopy showing the staining of different markers using
1214 Opal in cells classified as MEL-like and MES-like found in two melanoma TMAs.

1215 **b**. sSMLM images of H3K9me3 and H3K27ac nuclear distribution in SKMEL-5 (MEL), MM057
1216 (INT) and MM099 (MES).

1217 **c**. Average H3K27ac distribution genome-wide in MEL, INT, MES. Each profile represents the
1218 average of at least three independent cell lines.

1219 **d**. H3K9me3 staining in 501mel siNTC and siMS captured by sSMLM.

1220 **e**. H3K9me3 and H3K27ac ChIP-seq genome-wide distribution in 501mel siNTC and siMS.

1221

1222 **Supplemental Figure 2:**

1223 **a.** Normalized genomic occupancy (RPKM) of H3K9me3, H3K27ac, ATAC and RNA at active (A)
1224 and inactive (B) compartments in MEL, INT, MES, siNTC and siMS cells. Standard deviations

1225 bars are based on individual compartment BIN of 100kb spanning the whole genome. Unpaired t
1226 test was performed comparing A vs B per each marker (H3K9me3, H3K27ac, ATAC and RNA).

1227 **b**. Grouped column bar dot plot of the percentage of A and B compartments in *cis* and *trans*
1228 identified in melanoma states (top) and siNTC vs siMS (bottom). Two-way ANOVA test was
1229 performed to find significant differences. Each dot represents a biological replicate.

1230 **c**. HiC *trans* compartment saddle plots of melanoma states (top) and siNTC vs siMS (bottom).
1231 Values of 20% quantile areas are shown.

1232 **d**. Quantification of trans compartment AA, AB:BA and BB interactions shown in panel c. Each
1233 dot is a biological replicate. Unpaired t-test p-value of BB interactions in siNTC and siMS is shown.

1234 **e**. Column dot plot showing the RPKM enrichment of H3K9me3, H3K27ac, ATAC (left) and RNA
1235 (right) at compartments switching from A to B or B to A found in compartment switch analysis
1236 between states, siNTC and siMS. (Left) Each dot represent a single compartment of 100kb BIN.
1237 (Right) Each dot represent the average of normalized RNA reads, standard deviations bars are
1238 generated by compartments replicates. Unpaired t-test comparison was used. Significant p-
1239 values are displayed.

1240

1241 **Supplemental Figure 3:**

1242 **a.** Insulation score metaprofiles at MEL, INT and MES TADs boundaries across all melanoma cell
1243 lines.

1244 **b**. CTCF occupancy at MEL, INT and MES TADs boundaries in all cell lines. For a-b panels, red,
1245 grey and green colors mark melanocytic, intermediate and mesenchymal cells respectively.

1246 **c**. Insulation (top) and CTCF (bottom) profiles at siNTC, siMS, MEL, INT and MES TADs
1247 boundaries.

1248 **d**. HiC aggregate contact analysis of siMS cells at both siNTC and siMS TADs relative to siNTC
1249 cells.

1250 **e**. Relative intra-TAD (0) and inter-TAD (+1,+2,+3) HiC contacts in siMS relative to siNTC.

1251 **f**. Mean CTCF distribution in siNTC and siMS cells at MEL, INT, MES, siNTC and siMS loops.

1252 **g**. HiC aggregate peak analysis at MEL, INT and MES loops anchors in siMS, INT and MES cells
1253 relative to MEL/siNTC cells.

1254 **h**. Percentage of TADs (left) and loops (right) that are found common (shared) or specific of each
1255 state, siNTC and siMS. **i**. Volcano plot showing the DEGs found upon siMS in 501mel. MITF and
1256 SOX10 are shown. In red are DEGs with a significant adjusted p-value.

1257

1258 **Supplemental Figure 4:**

1259 **a.** Signac ATAC accessibility at *MITF* (top) and *EGFR* (bottom) loci in 12-273BM melanoma states
1260 identified by loHiC.

1261 **b**. HiC contact heatmap from chromosome 1 to X in MEL and MES cells profiled by loHiC. Color
1262 scale represents the log1p of contacts.

1263 **c**. Copy number variations (CNVs) analysis plot predicted by HiC in MEL and MES cells profiled
1264 by loHiC. Pearson correlation coefficient and p-value comparing CNVs in MEL vs MES are shown.

1265 **d**. Saddle plot of *cis* compartments in MEL and MES cells identified by loHiC.

1266 **e**. Bar dot plot of the HiC contacts intra-TAD (o) and inter-TAD (+1,+2,+3) in MES cells relative to
1267 MEL cells. Paired t-test was conducted comparing MEL vs MES at each TAD neighbor.

1268

1269 **Supplemental Figure 5:**

1270 **a.** 3D rendering of chromosome 1 modeled as a polymer chain using polychrom and based on
1271 the three principal components. Each bead is a 10kb BIN color scaled based on the predicted
1272 bead average softness. In grey are beads falling into blacklisted regions. The average
1273 chromosome 1 radius of gyration (Rg) per cell line are shown.

1274 **b**. Quantification of Rg changes upon a simulation of constriction of chr1 polymer chain. One-way
1275 ANOVA test was performed. Each dot represent a biological replicate.

1276 **c**. Column dot plot quantify the z-score enrichment of melanocytic and mesenchymal Widmer
1277 signatures[53] in 501mel Pre and Post migration. Unpaired t-test comparing Pre and Post for each
1278 signature was performed. Each dot is representative of an independent biological replicate.

1279 **d**. *cis* compartments saddle plot of Pre and Post 501mel and MM099 cells. 20% quantiles are
1280 shown.

1281 **e**. Scatter plot of compartment switching between Pre and Post cells in 501mel (top) and MM099
1282 (bottom). In black are highlighted significantly switching compartments.

1283 **f**. Melanocytic and mesenchymal Widmer signatures enrichment in MM099 Pre and Post
1284 quantified as averaged z-score. Three biological replicates were used. Unpaired statistical t-test
1285 was conducted.

1286 **g**. Chromatin diffusion (D_e) quantification in 501mel and MM099 Pre and Post migration. Unpaired
1287 t-test was conducted in Pre vs Post and Pre vs Pre pairwise comparisons. Resulted p-values are
1288 shown.

1289 **h**. Representative images captured by sSMLM for H3K9me3 and H3K27ac staining in MM099
1290 Pre and Post migration.

1291 **i**. Proliferation curve of 501mel Pre and Post measured as percentage of well confluence from
1292 time 0 till 96hrs. Each dot is the average of three biological replicates. Unpaired t-test was
1293 conducted to compare the end point.

1294 **j**. Snapshot of GFP fluorescence representing metastatic foci in livers of NSG injected intracardiac
1295 with 501mel Pre (n=7) or Post (n=7).

1296 **k**. (Left) Representative images of SKMEL-28 (MEL) post migratory cells upon 12hrs of DMSO
1297 (control) or Chaetocin treatment. (Right) SKMEL-28 post migratory relative quantification to the
1298 DMSO. Each dot represent an independent biological replicate. Paired t-test was performed. P-
1299 values is shown.

1300 **l**. Immunoblot showing H3K9me3, MITF and SOX10 variation upon 24hrs DMSO or Chaetocin
1301 (CHAE) treatments in 501mel and SKMEL-28. H3 and VINCULIN serve as internal loading
1302 controls. Relative molecular weights are shown on the right.

1303

1304 **Supplemental Figure 6:**

1305 **a.** (Left) Immunoblot for CTCF, MITF and EGFR across multiple melanoma cell lines used in this
1306 study. Vinculin serve as loading controls. Relative molecular weights are shown on the left. MEL,
1307 INT and MES cells are labeled in red, grey and green respectively. (Right) CTCF protein
1308 quantification based on the immunoblot shown on the right. One-way ANOVA test was used to
1309 assess statistical significance between MEL, INT and MES cells. Each dot represent a protein
1310 band of a biological replicate.

1311 **b.** Aggregate region analysis of siMS HiC contacts relative to siNTC at CTCF bound regions of
1312 MEL, INT and MES cells. **c**. CTCF state-specific regions identified with Diffbind and profiled for
1313 CTCF in all cell lines as averaged profile (top) and heatmap (bottom).

1314 **d**. Pie chart representing the percentage of CTCF MES-specific regions (n=1,274) annotated as
1315 CTCF-only (structural), intragenicEnh (intragenic enhancer), intergenicEnh (intergenic enhancer)
1316 or promoter.

1317 **e**. ABCscore quantified with a column dot plot. Each dot represent the average ABCscore value
1318 of cCREs (n=1,479) identified with the ABC model found to overlap with CTCF MES-specific
1319 regions. One-way ANOVA test was conducted, a summary p-value of the comparison MES vs all
1320 is shown.

1321 **f**. GSEA enrichment plot of the 5,081 genes found to be contacted by CTCF in MES cells and
1322 scored in Tsoi et al.[51] short-term culture cells classified as MEL (n=17) and MES (n=10). NES and
1323 adjusted p-values are shown.

1324 **g**. 5,081 genes signature score (ABC_5k) in melanocytic and mesenchymal cells found in
1325 melanoma patients by Pozniak et al.[85] Unpaired t-test p-value is displayed.

1326 **h**. Immunoblot for CTCF and ACTB (loading control) in whole cell protein extracts of MM099
1327 siNTC and siCTCF cells. Relative molecular weights are shown on the right.

1328 **i**. Venn diagram of the overlap between significantly DEGs siCTCF and ABC-5k. Hypergeometric
1329 test was conducted, representation factor and p-value are shown.

1330 **j**. Violin plot of the downregulated (Down) and upregulated (Up) genes upon siCTCF in
1331 melanocytic and mesenchymal melanoma cell states of patients' samples[85]. Unpaired t-test p-
1332 values are shown.

1333

1334 **Supplemental Figure 7:**

1335 **a**. Quantification of the number of CNVs as a grouped column plot across MEL, siNTC, siMS, INT
1336 and MES samples. Two-way ANOVA test was conducted.

1337 **b**. Column dot plot of the number of structural variants (SVs) found in the melanoma cell lines
1338 used in this study. One-way ANOVA test was performed.

1339 **c**. Fraction of *cis*-short, *cis*-long and *trans* HiC contacts in siNTC and siMS cells. Paired t-test was
1340 used.

1341 **d**. HiC aggregate region analysis at all TSS in siMS relative to siNTC.

1342 **e**. PCA plot of the most variable cCREs identified with DESeq2.

1343 **f**. ABC quantification of the top 500 state-specific cCRE Hubs across all cell lines. Bar plots show
1344 the average of all hubs. Standard error of the means bar are shown. Red, grey and green mark
1345 melanocytic, intermediate and mesenchymal cell lines respectively.

1346 **g**. Bar dot plot quantify the average methylation of 500 MES hubs in TCGA melanoma patients
1347 (n=470) classified in MEL, INT, NC (neural crest) and MES according to Tsoi[51]. One-way ANOVA
1348 p-value summarizing NC and MES vs INT and MEL comparisons is shown.

1349 **h**. HiC aggregate pile up heatmap of contacts at MES hubs in FFPE patients' specimen classified
1350 in MEL (n=3) and MES (n=4).

1351 **i**. Quantification of HiC contacts at the foreground of MEL and MES hubs in MEL and MES
1352 melanoma patients (n=7). Unpaired t-test p-values are shown.

1353 **j**. CTCF average genomic occupancy at MES hubs (n=500) in individual mesenchymal cell lines.

1354 **k**. Volcano plot of the differential MES cCREs activity in siCTCF MM099 cells predicted by
1355 RNAseq. In blue are marked the significantly dysregulated cCREs, in red the hubs. Y-axis dotted
1356 line show the significant p-value threshold. On top are marked the number of significantly active
1357 MES hubs (42 down, 136 up). Multiple t-test with Benjamini/Hochberg correction was used.

1358 For panels a,b,c,e,g and j, each dot is representative of a biological replicate.

1359

1360 **Supplementary information and material**

1361 **Supplemental Table 1:** Clinical and molecular information of the tumors' cores of the tissue
1362 microarray.

1363

1364 **Supplemental Table 2:** Differential expression analysis outputs in melanocytic, intermediate,
1365 mesenchymal and siMS. In yellow are marked the significantly positive associated gene to the
1366 corresponding condition.

1367

1368 **Supplemental Table 3:** Clinical and pathological information of the FFPE blocks processed for
1369 HiC.

1370

1371 **Supplemental Table 4:** List of genes contacted by CTCF in MES cells predicted by the ABC
1372 model.

1373

1374 **Supplemental Table 5:** List of all cCREs identified by the ABC model, their target genes and
1375 activity in melanoma cell states.

1376

1377 **Supplemental Table 6:** Ranked list of cCREs found significantly associated to MEL, INT and
1378 MES cells.

1379

1380 **Supplemental Table 7:** Transcription factor motif list analyzed for enrichment at hubs comparing
1381 MES vs MEL and INT cells.

1382

1383 **Supplemental reagents:** Complete list of reagents used in this work.

Bibliography

1. Hanahan D, Weinberg RA. The hallmarks of cancer. Cell. 2000;100(1):57-70. doi: 10.1016/s0092-8674(00)81683-9. PubMed PMID: 10647931.
2. Gupta GP, Massague J. Cancer metastasis: building a framework. Cell. 2006;127(4):679-95. doi: 10.1016/j.cell.2006.11.001. PubMed PMID: 17110329.
3. Lambert AW, Pattabiraman DR, Weinberg RA. Emerging Biological Principles of Metastasis. Cell. 2017;168(4):670-91. doi: 10.1016/j.cell.2016.11.037. PubMed PMID: 28187288; PMCID: PMC5308465.
4. Naxerova K. Evolutionary paths towards metastasis. Nat Rev Cancer. 2025;25(7):545-60. Epub 20250422. doi: 10.1038/s41568-025-00814-x. PubMed PMID: 40263543.
5. Hanahan D. Hallmarks of Cancer: New Dimensions. Cancer Discov. 2022;12(1):31-46. doi: 10.1158/2159-8290.CD-21-1059. PubMed PMID: 35022204.
6. Ciriello G, Magnani L, Aitken SJ, Akkari L, Behjati S, Hanahan D, Landau DA, Lopez-Bigas N, Lupianez DG, Marine JC, Martin-Villalba A, Natoli G, Obenauf AC, Oricchio E, Scaffidi P, Sottoriva A, Swarbrick A, Tonon G, Vanharanta S, Zuber J. Cancer Evolution: A Multifaceted Affair. Cancer Discov. 2024;14(1):36-48. doi: 10.1158/2159-8290.CD-23-0530. PubMed PMID: 38047596; PMCID: PMC10784746.
7. Schiffman JS, D'Avino AR, Prieto T, Pang Y, Fan Y, Rajagopalan S, Potenski C, Hara T, Suva ML, Gawad C, Landau DA. Defining heritability, plasticity, and transition dynamics of cellular phenotypes in somatic evolution. Nat Genet. 2024;56(10):2174-84. Epub 20240924. doi: 10.1038/s41588-024-01920-6. PubMed PMID: 39317739; PMCID: PMC11527590.
8. Esteller M, Dawson MA, Kadoch C, Rassool FV, Jones PA, Baylin SB. The Epigenetic Hallmarks of Cancer. Cancer Discov. 2024;14(10):1783-809. doi: 10.1158/2159-8290.CD-24-0296. PubMed PMID: 39363741.
9. Yan G, Monnier S, Mouelhi M, Dehoux T. Probing molecular crowding in compressed tissues with Brillouin light scattering. Proc Natl Acad Sci U S A. 2022;119(4). doi: 10.1073/pnas.2113614119. PubMed PMID: 35046032; PMCID: PMC8795543.
10. Li Y, Chen M, Hu J, Sheng R, Lin Q, He X, Guo M. Volumetric Compression Induces Intracellular Crowding to Control Intestinal Organoid Growth via Wnt/beta-Catenin Signaling. Cell Stem Cell. 2021;28(1):170-2. doi: 10.1016/j.stem.2020.12.003. PubMed PMID: 33417868.
11. Alric B, Formosa-Dague C, Dague E, Holt LJ, Delarue M. Macromolecular crowding limits growth under pressure. Nat Phys. 2022;18(4):411-6. Epub 20220224. doi: 10.1038/s41567-022-01506-1. PubMed PMID: 37152719; PMCID: PMC10162713.
12. Ong CT, Corces VG. CTCF: an architectural protein bridging genome topology and function. Nat Rev Genet. 2014;15(4):234-46. Epub 20140311. doi: 10.1038/nrg3663. PubMed PMID: 24614316; PMCID: PMC4610363.
13. Miron E, Oldenkamp R, Brown JM, Pinto DMS, Xu CS, Faria AR, Shaban HA, Rhodes JDP, Innocent C, de Ornellas S, Hess HF, Buckle V, Schermelleh L. Chromatin arranges in chains of mesoscale domains with nanoscale functional topography independent of cohesin. Science Advances. 2020;6(39). doi: 10.1126/sciadv.aba8811. PubMed PMID: WOS:000575531700008.
14. Li Y, Eshein A, Virk RKA, Eid A, Wu WL, Frederick J, VanDerway D, Gladstein S, Huang K, Shim AR, Anthony NM, Bauer GM, Zhou X, Agrawal V, Pujadas EM, Jain S, Esteve G, Chandler JE, Nguyen TQ, ..., Backman V. Nanoscale chromatin imaging and analysis platform bridges 4D chromatin organization with molecular function. Science Advances. 2021;7(1). doi: 10.1126/sciadv.abe4310. PubMed PMID: WOS:000605159200040.
15. Li WS, Carter LM, Almassalha LM, Gong R, Pujadas-Liwag LM, Kuo T, MacQuarrie KL, Carignano M, Dunton C, Dravid V, Kanemaki MT, Szleifer I, Backman V. Mature chromatin packing domains persist after RAD21 depletion in 3D. Science Advances. 2025;11:eadp0855.
16. Almassalha LM, Carignano M, Pujadas-Liwag EM, Li WS, Gong R, Acosta N, Dunton C, Gonzalez P, Carter L, Kakkaramadam R, Kröger M, Su P, Frederick J, Yu IC, Medina K, Pritchard

1434 J, Skol A, Nap R, MacQuarrie KL, ..., Backman V. Chromatin conformation, gene transcription,
1435 and nucleosome remodeling as an emergent system. Science Advances. 2025;11:eadq6652.
1436 17. Deng S, Feng Y, Pauklin S. 3D chromatin architecture and transcription regulation in
1437 cancer. J Hematol Oncol. 2022;15(1):49. Epub 20220504. doi: 10.1186/s13045-022-01271-x.
1438 PubMed PMID: 35509102; PMCID: PMC9069733.
1439 18. Xu J, Song F, Lyu H, Kobayashi M, Zhang B, Zhao Z, Hou Y, Wang X, Luan Y, Jia B,
1440 Stasiak L, Wong JH, Wang Q, Jin Q, Jin Q, Fu Y, Yang H, Hardison RC, Dovat S, ..., Yue F.
1441 Subtype-specific 3D genome alteration in acute myeloid leukaemia. Nature. 2022;611(7935):387-
1442 98. Epub 20221026. doi: 10.1038/s41586-022-05365-x. PubMed PMID: 36289338; PMCID:
1443 PMC10060167.
1444 19. Narang S, Ghebrechristos Y, Evensen NA, Murrell N, Jasinski S, Ostrow TH, Teachey DT,
1445 Raetz EA, Lionnet T, Witkowski M, Aifantis I, Tsirigos A, Carroll WL. Clonal evolution of the 3D
1446 chromatin landscape in patients with relapsed pediatric B-cell acute lymphoblastic leukemia. Nat
1447 Commun. 2024;15(1):7425. Epub 20240828. doi: 10.1038/s41467-024-51492-6. PubMed PMID:
1448 39198446; PMCID: PMC11358475.
1449 20. Mathur R, Wang Q, Schupp PG, Nikolic A, Hilz S, Hong C, Grishanina NR, Kwok D,
1450 Stevers NO, Jin Q, Youngblood MW, Stasiak LA, Hou Y, Wang J, Yamaguchi TN, Lafontaine M,
1451 Shai A, Smirnov IV, Solomon DA, ..., Costello JF. Glioblastoma evolution and heterogeneity from
1452 a 3D whole-tumor perspective. Cell. 2024;187(2):446-63 e16. doi: 10.1016/j.cell.2023.12.013.
1453 PubMed PMID: 38242087; PMCID: PMC10832360.
1454 21. Akdemir KC, Le VT, Kim JM, Killcoyne S, King DA, Lin YP, Tian Y, Inoue A, Amin SB,
1455 Robinson FS, Nimmakayalu M, Herrera RE, Lynn EJ, Chan K, Seth S, Klimczak LJ, Gerstung M,
1456 Gordenin DA, O'Brien J, ..., Andrew Futreal P. Somatic mutation distributions in cancer genomes
1457 vary with three-dimensional chromatin structure. Nat Genet. 2020;52(11):1178-88. Epub
1458 20201005. doi: 10.1038/s41588-020-0708-0. PubMed PMID: 33020667; PMCID: PMC8350746.
1459 22. Dubois F, Sidiropoulos N, Weischenfeldt J, Beroukhim R. Structural variations in cancer
1460 and the 3D genome. Nat Rev Cancer. 2022;22(9):533-46. Epub 20220628. doi: 10.1038/s41568-
1461 022-00488-9. PubMed PMID: 35764888; PMCID: PMC10423586.
1462 23. Breves SL, Di Giammartino DC, Nicholson J, Cirigliano S, Mahmood SR, Lee UJ,
1463 Martinez-Fundichely A, Jungverdorben J, Singhania R, Rajkumar S, Kirou R, Studer L, Khurana
1464 E, Polyzos A, Fine HA, Apostolou E. Three-dimensional regulatory hubs support oncogenic
1465 programs in glioblastoma. Mol Cell. 2025;85(7):1330-48 e6. Epub 20250326. doi:
1466 10.1016/j.molcel.2025.03.007. PubMed PMID: 40147440; PMCID: PMC12009607.
1467 24. Gambi G, Boccalatte F, Rodriguez Hernaez J, Lin Z, Nadorp B, Polyzos A, Tan J,
1468 Avrampou K, Inghirami G, Kentsis A, Apostolou E, Aifantis I, Tsirigos A. 3D chromatin hubs as
1469 regulatory units of identity and survival in human acute leukemia. Mol Cell. 2025;85(1):42-60 e7.
1470 Epub 20241223. doi: 10.1016/j.molcel.2024.11.040. PubMed PMID: 39719705; PMCID:
1471 PMC11934262.
1472 25. Strom AR, Biggs RJ, Banigan EJ, Wang X, Chiu K, Herman C, Collado J, Yue F, Ritland
1473 Politz JC, Tait LJ, Scalzo D, Telling A, Groudine M, Brangwynne CP, Marko JF, Stephens AD.
1474 HP1alpha is a chromatin crosslinker that controls nuclear and mitotic chromosome mechanics.
1475 Elife. 2021;10. Epub 20210609. doi: 10.7554/eLife.63972. PubMed PMID: 34106828; PMCID:
1476 PMC8233041.
1477 26. Heo SJ, Driscoll TP, Thorpe SD, Nerurkar NL, Baker BM, Yang MT, Chen CS, Lee DA,
1478 Mauck RL. Differentiation alters stem cell nuclear architecture, mechanics, and mechano-
1479 sensitivity. Elife. 2016;5. Epub 20161130. doi: 10.7554/eLife.18207. PubMed PMID: 27901466;
1480 PMCID: PMC5148611.
1481 27. Patta I, Zand M, Lee L, Mishra S, Bortnick A, Lu H, Prusty A, McArdle S, Mikulski Z, Wang
1482 HY, Cheng CS, Fisch KM, Hu M, Murre C. Nuclear morphology is shaped by loop-extrusion
1483 programs. Nature. 2024;627(8002):196-203. Epub 20240214. doi: 10.1038/s41586-024-07086-
1484 9. PubMed PMID: 38355805; PMCID: PMC11052650.

28. Scott AK, Rafuse M, Neu CP. Mechanically induced alterations in chromatin architecture guide the balance between cell plasticity and mechanical memory. Front Cell Dev Biol. 2023;11:1084759. Epub 20230418. doi: 10.3389/fcell.2023.1084759. PubMed PMID: 37143893; PMCID: PMC10151697.
29. Shivashankar GV. Mechanical forces and the 3D genome. Curr Opin Struct Biol. 2023;83:102728. Epub 20231109. doi: 10.1016/j.sbi.2023.102728. PubMed PMID: 37948897.
30. Denais CM, Gilbert RM, Isermann P, McGregor AL, te Lindert M, Weigelin B, Davidson PM, Friedl P, Wolf K, Lammerding J. Nuclear envelope rupture and repair during cancer cell migration. Science. 2016;352(6283):353-8. Epub 20160324. doi: 10.1126/science.aad7297. PubMed PMID: 27013428; PMCID: PMC4833568.
31. Shroff NP, Xu P, Kim S, Shelton ER, Gross BJ, Liu Y, Gomez CO, Ye Q, Drennon TY, Hu JK, Green JBA, Campas O, Klein OD. Proliferation-driven mechanical compression induces signalling centre formation during mammalian organ development. Nat Cell Biol. 2024;26(4):519-29. Epub 20240403. doi: 10.1038/s41556-024-01380-4. PubMed PMID: 38570617.
32. Tse JM, Cheng G, Tyrrell JA, Wilcox-Adelman SA, Boucher Y, Jain RK, Munn LL. Mechanical compression drives cancer cells toward invasive phenotype. Proc Natl Acad Sci U S A. 2012;109(3):911-6. Epub 20111227. doi: 10.1073/pnas.1118910109. PubMed PMID: 22203958; PMCID: PMC3271885.
33. Dupont S, Wickstrom SA. Mechanical regulation of chromatin and transcription. Nat Rev Genet. 2022;23(10):624-43. Epub 20220523. doi: 10.1038/s41576-022-00493-6. PubMed PMID: 35606569.
34. Pujadas Liwag EM, Acosta N, Almassalha LM, Su YP, Gong R, Kanemaki MT, Stephens AD, Backman V. Nuclear blebs are associated with destabilized chromatin-packing domains. J Cell Sci. 2025;138(3). Epub 20250211. doi: 10.1242/jcs.262161. PubMed PMID: 39878045; PMCID: PMC11883274.
35. Gupta PB, Onder TT, Jiang G, Tao K, Kuperwasser C, Weinberg RA, Lander ES. Identification of selective inhibitors of cancer stem cells by high-throughput screening. Cell. 2009;138(4):645-59. Epub 20090813. doi: 10.1016/j.cell.2009.06.034. PubMed PMID: 19682730; PMCID: PMC4892125.
36. Rhim AD, Mirek ET, Aiello NM, Maitra A, Bailey JM, McAllister F, Reichert M, Beatty GL, Rustgi AK, Vonderheide RH, Leach SD, Stanger BZ. EMT and dissemination precede pancreatic tumor formation. Cell. 2012;148(1-2):349-61. doi: 10.1016/j.cell.2011.11.025. PubMed PMID: 22265420; PMCID: PMC3266542.
37. Yu M, Bardia A, Wittner BS, Stott SL, Smas ME, Ting DT, Isakoff SJ, Ciciliano JC, Wells MN, Shah AM, Concannon KF, Donaldson MC, Sequist LV, Brachtel E, Sgroi D, Baselga J, Ramaswamy S, Toner M, Haber DA, Maheswaran S. Circulating breast tumor cells exhibit dynamic changes in epithelial and mesenchymal composition. Science. 2013;339(6119):580-4. doi: 10.1126/science.1228522. PubMed PMID: 23372014; PMCID: PMC3760262.
38. Pastushenko I, Brisebarre A, Sifrim A, Fioramonti M, Revenco T, Boumahdi S, Van Keymeulen A, Brown D, Moers V, Lemaire S, De Clercq S, Minguijon E, Balsat C, Sokolow Y, Dubois C, De Cock F, Scozzaro S, Sopena F, Lanas A, D'Haene N, Salmon I, Marine JC, Voet T, Sotiropoulou PA, Blanpain C. Identification of the tumour transition states occurring during EMT. Nature. 2018;556(7702):463-8. Epub 20180418. doi: 10.1038/s41586-018-0040-3. PubMed PMID: 29670281.
39. Karras P, Bordeu I, Pozniak J, Nowosad A, Pazzi C, Van Raemdonck N, Landeloos E, Van Herck Y, Pedri D, Bervoets G, Makhzami S, Khoo JH, Pavie B, Lamote J, Marin-Bejar O, Dewaele M, Liang H, Zhang X, Hua Y, Wouters J, Browaeys R, Bergers G, Saeys Y, Bosisio F, van den Oord J, Lambrechts D, Rustgi AK, Bechter O, Blanpain C, Simons BD, Rambow F, Marine JC. A cellular hierarchy in melanoma uncouples growth and metastasis. Nature. 2022;610(7930):190-8. Epub 20220921. doi: 10.1038/s41586-022-05242-7. PubMed PMID: 36131018; PMCID: PMC10439739.

40. Bajaj S, Donnelly D, Call M, Johannet P, Moran U, Polsky D, Shapiro R, Berman R, Pavlick A, Weber J, Zhong J, Osman I. Melanoma Prognosis: Accuracy of the American Joint Committee on Cancer Staging Manual Eighth Edition. J Natl Cancer Inst. 2020;112(9):921-8. doi: 10.1093/jnci/djaa008. PubMed PMID: 31977051; PMCID: PMC7492758.
41. Sun Q, Lee W, Mohri Y, Takeo M, Lim CH, Xu X, Myung P, Atit RP, Taketo MM, Moubarak RS, Schober M, Osman I, Gay DL, Saur D, Nishimura EK, Ito M. A novel mouse model demonstrates that oncogenic melanocyte stem cells engender melanoma resembling human disease. Nat Commun. 2019;10(1):5023. Epub 20191104. doi: 10.1038/s41467-019-12733-1. PubMed PMID: 31685822; PMCID: PMC6828673.
42. Vallius T, Shi Y, Novikov E, Pant SM, Pelletier R, Chen YA, Tefft JB, Johnson AN, Maliga Z, Wan G, Murphy G, Santagata S, Semenov YR, Liu D, Lian CG, Sorger PK. Spatial determinants of tumor cell dedifferentiation and plasticity in primary cutaneous melanoma. bioRxiv. 2025. Epub 20250624. doi: 10.1101/2025.06.21.660851. PubMed PMID: 40667360; PMCID: PMC12262277.
43. Rambow F, Marine JC, Goding CR. Melanoma plasticity and phenotypic diversity: therapeutic barriers and opportunities. Genes Dev. 2019;33(19-20):1295-318. doi: 10.1101/gad.329771.119. PubMed PMID: 31575676; PMCID: PMC6771388.
44. Hoek KS, Goding CR. Cancer stem cells versus phenotype-switching in melanoma. Pigment Cell Melanoma Res. 2010;23(6):746-59. Epub 20100820. doi: 10.1111/j.1755-148X.2010.00757.x. PubMed PMID: 20726948.
45. Wouters J, Kalender-Atak Z, Minnoye L, Spanier KI, De Waegeneer M, Bravo Gonzalez-Blas C, Mauduit D, Davie K, Hulselmans G, Najem A, Dewaele M, Pedri D, Rambow F, Makhzami S, Christiaens V, Ceyssens F, Ghanem G, Marine JC, Poovathingal S, Aerts S. Robust gene expression programs underlie recurrent cell states and phenotype switching in melanoma. Nat Cell Biol. 2020;22(8):986-98. Epub 20200803. doi: 10.1038/s41556-020-0547-3. PubMed PMID: 32753671.
46. Laurette P, Strub T, Koludrovic D, Keime C, Le Gras S, Seberg H, Van Otterloo E, Imrichova H, Siddaway R, Aerts S, Cornell RA, Mengus G, Davidson I. Transcription factor MITF and remodeller BRG1 define chromatin organisation at regulatory elements in melanoma cells. Elife. 2015;4. Epub 20150324. doi: 10.7554/eLife.06857. PubMed PMID: 25803486; PMCID: PMC4407272.
47. Verfaillie A, Imrichova H, Atak ZK, Dewaele M, Rambow F, Hulselmans G, Christiaens V, Svetlichnyy D, Luciani F, Van den Mooter L, Claerhout S, Fiers M, Journe F, Ghanem GE, Herrmann C, Halder G, Marine JC, Aerts S. Decoding the regulatory landscape of melanoma reveals TEADS as regulators of the invasive cell state. Nat Commun. 2015;6:6683. Epub 20150409. doi: 10.1038/ncomms7683. PubMed PMID: 25865119; PMCID: PMC4403341.
48. Tirosh I, Izar B, Prakadan SM, Wadsworth MH, 2nd, Treacy D, Trombetta JJ, Rotem A, Rodman C, Lian C, Murphy G, Fallahi-Sichani M, Dutton-Regester K, Lin JR, Cohen O, Shah P, Lu D, Genshaft AS, Hughes TK, Ziegler CG, ..., Garraway LA. Dissecting the multicellular ecosystem of metastatic melanoma by single-cell RNA-seq. Science. 2016;352(6282):189-96. doi: 10.1126/science.aad0501. PubMed PMID: 27124452; PMCID: PMC4944528.
49. Rambow F, Rogiers A, Marin-Bejar O, Aibar S, Femel J, Dewaele M, Karras P, Brown D, Chang YH, Debiec-Rychter M, Adriaens C, Radaelli E, Wolter P, Bechter O, Dummer R, Levesque M, Piris A, Frederick DT, Boland G, ..., Marine JC. Toward Minimal Residual Disease-Directed Therapy in Melanoma. Cell. 2018;174(4):843-55 e19. Epub 20180712. doi: 10.1016/j.cell.2018.06.025. PubMed PMID: 30017245.
50. Marin-Bejar O, Rogiers A, Dewaele M, Femel J, Karras P, Pozniak J, Bervoets G, Van Raemdonck N, Pedri D, Swings T, Demeulemeester J, Borght SV, Lehnert S, Bosisio F, van den Oord JJ, Bempt IV, Lambrechts D, Voet T, Bechter O, ..., Marine JC. Evolutionary predictability of genetic versus nongenetic resistance to anticancer drugs in melanoma. Cancer Cell. 2021;39(8):1135-49 e8. Epub 20210617. doi: 10.1016/j.ccell.2021.05.015. PubMed PMID: 34143978.

51. Tsoi J, Robert L, Paraiso K, Galvan C, Sheu KM, Lay J, Wong DJL, Atefi M, Shirazi R, Wang X, Braas D, Grasso CS, Palaskas N, Ribas A, Graeber TG. Multi-stage Differentiation Defines Melanoma Subtypes with Differential Vulnerability to Drug-Induced Iron-Dependent Oxidative Stress. Cancer Cell. 2018;33(5):890-904 e5. Epub 20180412. doi: 10.1016/j.ccell.2018.03.017. PubMed PMID: 29657129; PMCID: PMC5953834.
52. Hoek KS, Eichhoff OM, Schlegel NC, Dobbeling U, Kobert N, Schaerer L, Hemmi S, Dummer R. In vivo switching of human melanoma cells between proliferative and invasive states. Cancer Res. 2008;68(3):650-6. doi: 10.1158/0008-5472.CAN-07-2491. PubMed PMID: 18245463.
53. Widmer DS, Cheng PF, Eichhoff OM, Belloni BC, Zipser MC, Schlegel NC, Javelaud D, Mauviel A, Dummer R, Hoek KS. Systematic classification of melanoma cells by phenotype-specific gene expression mapping. Pigment Cell Melanoma Res. 2012;25(3):343-53. Epub 20120302. doi: 10.1111/j.1755-148X.2012.00986.x. PubMed PMID: 22336146.
54. Schmidl C, Rendeiro AF, Sheffield NC, Bock C. ChIPmentation: fast, robust, low-input ChIP-seq for histones and transcription factors. Nat Methods. 2015;12(10):963-5. Epub 20150817. doi: 10.1038/nmeth.3542. PubMed PMID: 26280331; PMCID: PMC4589892.
55. Conway K, Edmiston SN, Vondras A, Reiner A, Corcoran DL, Shen R, Parrish EA, Hao H, Lin L, Kenney JM, Ilelaboye G, Kostrzewa CE, Kuan PF, Busam KJ, Lezcano C, Lee TK, Hernando E, Googe PB, Ollila DW, Moschos S, Gorlov I, Amos CI, Ernstoff MS, Cust AE, Wilmott JS, Scolyer RA, Mann GJ, Vergara IA, Ko J, Rees JR, Yan S, Nagore E, Bosenberg M, Rothberg BG, Osman I, Lee JE, Saenger Y, Bogner P, Thompson CL, Gerstenblith M, Holmen SL, Funchain P, Brunsgaard E, Depcik-Smith ND, Luo L, Boyce T, Orlow I, Begg CB, Berwick M, Thomas NE, Inter MELSG. DNA Methylation Classes of Stage II and III Primary Melanomas and Their Clinical and Prognostic Significance. JCO Precis Oncol. 2024;8:e2400375. Epub 20241107. doi: 10.1200/PO-24-00375. PubMed PMID: 39509669; PMCID: PMC11737429.
56. Chang L, Xie Y, Taylor B, Wang Z, Sun J, Armand EJ, Mishra S, Xu J, Tastemel M, Lie A, Gibbs ZA, Indralingam HS, Tan TM, Bejar R, Chen CC, Furnari FB, Hu M, Ren B. Droplet Hi-C enables scalable, single-cell profiling of chromatin architecture in heterogeneous tissues. Nat Biotechnol. 2025;43(10):1694-707. Epub 20241018. doi: 10.1038/s41587-024-02447-1. PubMed PMID: 39424717; PMCID: PMC12520981.
57. Sakellaropoulos T, Do C, Jiang G, Cova G, Meyn P, Dimartino D, Ramaswami S, Heguy A, Tsirigos A, Skok JA. MethNet: a robust approach to identify regulatory hubs and their distal targets from cancer data. Nat Commun. 2024;15(1):6027. Epub 20240717. doi: 10.1038/s41467-024-50380-3. PubMed PMID: 39025865; PMCID: PMC11258126.
58. Doench JG, Fusi N, Sullender M, Hegde M, Vaimberg EW, Donovan KF, Smith I, Tothova Z, Wilen C, Orchard R, Virgin HW, Listgarten J, Root DE. Optimized sgRNA design to maximize activity and minimize off-target effects of CRISPR-Cas9. Nat Biotechnol. 2016;34(2):184-91. Epub 20160118. doi: 10.1038/nbt.3437. PubMed PMID: 26780180; PMCID: PMC4744125.
59. Gladstein S, Stawarz A, Almassalha LM, Cherkezyan L, Chandler JE, Zhou X, Subramanian H, Backman V. Measuring Nanoscale Chromatin Heterogeneity with Partial Wave Spectroscopic Microscopy. Methods Mol Biol. 2018;1745:337-60. doi: 10.1007/978-1-4939-7680-5_19. PubMed PMID: 29476478; PMCID: PMC5983358.
60. Almassalha LM, Bauer GM, Chandler JE, Gladstein S, Cherkezyan L, Stypula-Cyrus Y, Weinberg S, Zhang D, Thusgaard Ruhoff P, Roy HK, Subramanian H, Chandel NS, Szleifer I, Backman V. Label-free imaging of the native, living cellular nanoarchitecture using partial-wave spectroscopic microscopy. Proc Natl Acad Sci U S A. 2016;113(42):E6372-E81. Epub 20161004. doi: 10.1073/pnas.1608198113. PubMed PMID: 27702891; PMCID: PMC5081614.
61. Gladstein S, Almassalha LM, Cherkezyan L, Chandler JE, Eshein A, Eid A, Zhang D, Wu W, Bauer GM, Stephens AD, Morochnik S, Subramanian H, Marko JF, Ameer GA, Szleifer I, Backman V. Multimodal interference-based imaging of nanoscale structure and macromolecular

motion uncovers UV induced cellular paroxysm. Nat Commun. 2019;10(1):1652. Epub 20190410. doi: 10.1038/s41467-019-09717-6. PubMed PMID: 30971691; PMCID: PMC6458150.

62. Virk RKA, Wu W, Almassalha LM, Bauer GM, Li Y, VanDerway D, Frederick J, Zhang D, Eshein A, Roy HK, Szleifer I, Backman V. Disordered chromatin packing regulates phenotypic plasticity. Sci Adv. 2020;6(2):eaax6232. Epub 20200108. doi: 10.1126/sciadv.aax6232. PubMed PMID: 31934628; PMCID: PMC6949045.

63. Eid A, Eshein A, Li Y, Virk R, Van Derway D, Zhang D, Taflove A, Backman V. Characterizing chromatin packing scaling in whole nuclei using interferometric microscopy. Opt Lett. 2020;45(17):4810-3. doi: 10.1364/OL.400231. PubMed PMID: 32870863; PMCID: PMC7951997.

64. Pujadas Liwag EM, Wei X, Acosta N, Carter LM, Yang J, Almassalha LM, Jain S, Daneshkhah A, Rao SSP, Seker-Polat F, MacQuarrie KL, Ibarra J, Agrawal V, Aiden EL, Kanemaki MT, Backman V, Adli M. Depletion of lamins B1 and B2 promotes chromatin mobility and induces differential gene expression by a mesoscale-motion-dependent mechanism. Genome Biol. 2024;25(1):77. Epub 20240322. doi: 10.1186/s13059-024-03212-y. PubMed PMID: 38519987; PMCID: PMC10958841.

65. Langmead B, Salzberg SL. Fast gapped-read alignment with Bowtie 2. Nat Methods. 2012;9(4):357-9. Epub 20120304. doi: 10.1038/nmeth.1923. PubMed PMID: 22388286; PMCID: PMC3322381.

66. Li H, Handsaker B, Wysoker A, Fennell T, Ruan J, Homer N, Marth G, Abecasis G, Durbin R, Genome Project Data Processing S. The Sequence Alignment/Map format and SAMtools. Bioinformatics. 2009;25(16):2078-9. Epub 20090608. doi: 10.1093/bioinformatics/btp352. PubMed PMID: 19505943; PMCID: PMC2723002.

67. Ramirez F, Dundar F, Diehl S, Gruning BA, Manke T. deepTools: a flexible platform for exploring deep-sequencing data. Nucleic Acids Res. 2014;42(Web Server issue):W187-91. Epub 20140505. doi: 10.1093/nar/gku365. PubMed PMID: 24799436; PMCID: PMC4086134.

68. Liu T. Use model-based Analysis of ChIP-Seq (MACS) to analyze short reads generated by sequencing protein-DNA interactions in embryonic stem cells. Methods Mol Biol. 2014;1150:81-95. doi: 10.1007/978-1-4939-0512-6_4. PubMed PMID: 24743991.

69. Quinlan AR, Hall IM. BEDTools: a flexible suite of utilities for comparing genomic features. Bioinformatics. 2010;26(6):841-2. Epub 20100128. doi: 10.1093/bioinformatics/btq033. PubMed PMID: 20110278; PMCID: PMC2832824.

70. Sandelin A, Alkema W, Engstrom P, Wasserman WW, Lenhard B. JASPAR: an open-access database for eukaryotic transcription factor binding profiles. Nucleic Acids Res. 2004;32(Database issue):D91-4. doi: 10.1093/nar/gkh012. PubMed PMID: 14681366; PMCID: PMC308747.

71. Heinz S, Benner C, Spann N, Bertolino E, Lin YC, Laslo P, Cheng JX, Murre C, Singh H, Glass CK. Simple combinations of lineage-determining transcription factors prime cis-regulatory elements required for macrophage and B cell identities. Mol Cell. 2010;38(4):576-89. doi: 10.1016/j.molcel.2010.05.004. PubMed PMID: 20513432; PMCID: PMC2898526.

72. Machanick P, Bailey TL. MEME-ChIP: motif analysis of large DNA datasets. Bioinformatics. 2011;27(12):1696-7. Epub 20110412. doi: 10.1093/bioinformatics/btr189. PubMed PMID: 21486936; PMCID: PMC3106185.

73. Ross-Innes CS, Stark R, Teschendorff AE, Holmes KA, Ali HR, Dunning MJ, Brown GD, Gojis O, Ellis IO, Green AR, Ali S, Chin SF, Palmieri C, Caldas C, Carroll JS. Differential oestrogen receptor binding is associated with clinical outcome in breast cancer. Nature. 2012;481(7381):389-93. Epub 20120104. doi: 10.1038/nature10730. PubMed PMID: 22217937; PMCID: PMC3272464.

74. Servant N, Varoquaux N, Lajoie BR, Viara E, Chen CJ, Vert JP, Heard E, Dekker J, Barillot E. HiC-Pro: an optimized and flexible pipeline for Hi-C data processing. Genome Biol.

2015;16:259. Epub 20151201. doi: 10.1186/s13059-015-0831-x. PubMed PMID: 26619908; PMCID: PMC4665391.
75. Berico P, Flores Yanke AF, Vand Rajabpour F, Do C, Simonin Wilmer I, Sakellaropoulos T, Delclaux Obieta I, Stagnitta R, Vazquez Cruz E, Osman I, Skok J, Robles-Espinoza CD, Lund AW, Schober M, Hernando E. A targetable developmental program co-regulates angiogenesis and immune evasion. bioRxiv. 2024. Epub 20241221. doi: 10.1101/2024.12.21.628442. PubMed PMID: 39764043; PMCID: PMC11702693.
76. Open2C, Abdennur N, Abraham S, Fudenberg G, Flyamer IM, Galitsyna AA, Goloborodko A, Imakaev M, Oksuz BA, Venev SV, Xiao Y. Cooltools: Enabling high-resolution Hi-C analysis in Python. PLoS Comput Biol. 2024;20(5):e1012067. Epub 20240506. doi: 10.1371/journal.pcbi.1012067. PubMed PMID: 38709825; PMCID: PMC11098495.
77. Durand NC, Shamim MS, Machol I, Rao SS, Huntley MH, Lander ES, Aiden EL. Juicer Provides a One-Click System for Analyzing Loop-Resolution Hi-C Experiments. Cell Syst. 2016;3(1):95-8. doi: 10.1016/j.cels.2016.07.002. PubMed PMID: 27467249; PMCID: PMC5846465.
78. Wang S, Lee S, Chu C, Jain D, Kerpedjiev P, Nelson GM, Walsh JM, Alver BH, Park PJ. HiNT: a computational method for detecting copy number variations and translocations from Hi-C data. Genome Biol. 2020;21(1):73. Epub 20200323. doi: 10.1186/s13059-020-01986-5. PubMed PMID: 32293513; PMCID: PMC7087379.
79. Forcato M, Nicoletti C, Pal K, Livi CM, Ferrari F, Bicciato S. Comparison of computational methods for Hi-C data analysis. Nat Methods. 2017;14(7):679-85. Epub 20170612. doi: 10.1038/nmeth.4325. PubMed PMID: 28604721; PMCID: PMC5493985.
80. Salameh TJ, Wang X, Song F, Zhang B, Wright SM, Khunsriraksakul C, Ruan Y, Yue F. A supervised learning framework for chromatin loop detection in genome-wide contact maps. Nat Commun. 2020;11(1):3428. Epub 20200709. doi: 10.1038/s41467-020-17239-9. PubMed PMID: 32647330; PMCID: PMC7347923.
81. van der Weide RH, van den Brand T, Haarhuis JHI, Teunissen H, Rowland BD, de Wit E. Hi-C analyses with GENOVA: a case study with cohesin variants. NAR Genom Bioinform. 2021;3(2):lqab040. Epub 20210522. doi: 10.1093/nargab/lqab040. PubMed PMID: 34046591; PMCID: PMC8140737.
82. Fulco CP, Nasser J, Jones TR, Munson G, Bergman DT, Subramanian V, Grossman SR, Anyoha R, Doughty BR, Patwardhan TA, Nguyen TH, Kane M, Perez EM, Durand NC, Lareau CA, Stamenova EK, Aiden EL, Lander ES, Engreitz JM. Activity-by-contact model of enhancer-promoter regulation from thousands of CRISPR perturbations. Nat Genet. 2019;51(12):1664-9. Epub 20191129. doi: 10.1038/s41588-019-0538-0. PubMed PMID: 31784727; PMCID: PMC6886585.
83. Love MI, Huber W, Anders S. Moderated estimation of fold change and dispersion for RNA-seq data with DESeq2. Genome Biol. 2014;15(12):550. doi: 10.1186/s13059-014-0550-8. PubMed PMID: 25516281; PMCID: PMC4302049.
84. Hao Y, Stuart T, Kowalski MH, Choudhary S, Hoffman P, Hartman A, Srivastava A, Molla G, Madad S, Fernandez-Granda C, Satija R. Dictionary learning for integrative, multimodal and scalable single-cell analysis. Nat Biotechnol. 2024;42(2):293-304. Epub 20230525. doi: 10.1038/s41587-023-01767-y. PubMed PMID: 37231261; PMCID: PMC10928517.
85. Pozniak J, Pedri D, Landeloos E, Van Herck Y, Antoranz A, Vanwynsberghe L, Nowosad A, Roda N, Makhzami S, Bervoets G, Maciel LF, Pulido-Vicuna CA, Pollaris L, Seurinck R, Zhao F, Flem-Karlsen K, Damsky W, Chen L, Karagianni D, Cinque S, Kint S, Vandereyken K, Rombaut B, Voet T, Vernaillen F, Annaert W, Lambrechts D, Boecxstaens V, Saeys Y, van den Oord J, Bosisio F, Karras P, Shain AH, Bosenberg M, Leucci E, Paschen A, Rambow F, Bechter O, Marine JC. A TCF4-dependent gene regulatory network confers resistance to immunotherapy in melanoma. Cell. 2024;187(1):166-83 e25. doi: 10.1016/j.cell.2023.11.037. PubMed PMID: 38181739.

86. Aibar S, Gonzalez-Blas CB, Moerman T, Huynh-Thu VA, Imrichova H, Hulselmans G, Rambow F, Marine JC, Geurts P, Aerts J, van den Oord J, Atak ZK, Wouters J, Aerts S. SCENIC: single-cell regulatory network inference and clustering. Nat Methods. 2017;14(11):1083-6. Epub 20171009. doi: 10.1038/nmeth.4463. PubMed PMID: 28991892; PMCID: PMC5937676.
87. Stuart T, Srivastava A, Madad S, Lareau CA, Satija R. Author Correction: Single-cell chromatin state analysis with Signac. Nat Methods. 2022;19(2):257. doi: 10.1038/s41592-022-01393-7. PubMed PMID: 34997233.
88. Li W, Xu H, Xiao T, Cong L, Love MI, Zhang F, Irizarry RA, Liu JS, Brown M, Liu XS. MAGeCK enables robust identification of essential genes from genome-scale CRISPR/Cas9 knockout screens. Genome Biol. 2014;15(12):554. doi: 10.1186/s13059-014-0554-4. PubMed PMID: 25476604; PMCID: PMC4290824.
89. Dobin A, Davis CA, Schlesinger F, Drenkow J, Zaleski C, Jha S, Batut P, Chaisson M, Gingeras TR. STAR: ultrafast universal RNA-seq aligner. Bioinformatics. 2013;29(1):15-21. Epub 20121025. doi: 10.1093/bioinformatics/bts635. PubMed PMID: 23104886; PMCID: PMC3530905.
90. Robinson MD, McCarthy DJ, Smyth GK. edgeR: a Bioconductor package for differential expression analysis of digital gene expression data. Bioinformatics. 2010;26(1):139-40. Epub 20091111. doi: 10.1093/bioinformatics/btp616. PubMed PMID: 19910308; PMCID: PMC2796818.
91. Li B, Dewey CN. RSEM: accurate transcript quantification from RNA-Seq data with or without a reference genome. BMC Bioinformatics. 2011;12:323. Epub 20110804. doi: 10.1186/1471-2105-12-323. PubMed PMID: 21816040; PMCID: PMC3163565.
92. Zhou W, Triche TJ, Jr., Laird PW, Shen H. SeSAMe: reducing artifactual detection of DNA methylation by Infinium BeadChips in genomic deletions. Nucleic Acids Res. 2018;46(20):e123. doi: 10.1093/nar/gky691. PubMed PMID: 30085201; PMCID: PMC6237738.
93. Colaprico A, Silva TC, Olsen C, Garofano L, Cava C, Garolini D, Sabedot TS, Malta TM, Pagnotta SM, Castiglioni I, Ceccarelli M, Bontempi G, Noushmehr H. TCGAbiolinks: an R/Bioconductor package for integrative analysis of TCGA data. Nucleic Acids Res. 2016;44(8):e71. Epub 20151223. doi: 10.1093/nar/gkv1507. PubMed PMID: 26704973; PMCID: PMC4856967.
94. Lawrence M, Huber W, Pages H, Aboyoun P, Carlson M, Gentleman R, Morgan MT, Carey VJ. Software for computing and annotating genomic ranges. PLoS Comput Biol. 2013;9(8):e1003118. Epub 20130808. doi: 10.1371/journal.pcbi.1003118. PubMed PMID: 23950696; PMCID: PMC3738458.
95. Cerami E, Gao J, Dogrusoz U, Gross BE, Sumer SO, Aksoy BA, Jacobsen A, Byrne CJ, Heuer ML, Larsson E, Antipin Y, Reva B, Goldberg AP, Sander C, Schultz N. The cBio cancer genomics portal: an open platform for exploring multidimensional cancer genomics data. Cancer Discov. 2012;2(5):401-4. doi: 10.1158/2159-8290.CD-12-0095. PubMed PMID: 22588877; PMCID: PMC3956037.
96. Arafeh R, Shibue T, Dempster JM, Hahn WC, Vazquez F. The present and future of the Cancer Dependency Map. Nat Rev Cancer. 2025;25(1):59-73. Epub 20241028. doi: 10.1038/s41568-024-00763-x. PubMed PMID: 39468210.
97. Goldman MJ, Craft B, Hastie M, Repecka K, McDade F, Kamath A, Banerjee A, Luo Y, Rogers D, Brooks AN, Zhu J, Haussler D. Visualizing and interpreting cancer genomics data via the Xena platform. Nat Biotechnol. 2020;38(6):675-8. doi: 10.1038/s41587-020-0546-8. PubMed PMID: 32444850; PMCID: PMC7386072.
98. Yost KE, Zhao Y, Hung KL, Zhu K, Xu D, Corces MR, Shams S, Louie BH, Sarmashghi S, Sundaram L, Luebeck J, Clarke S, Doane AS, Granja JM, Choudhry H, Imielinski M, Cherniack AD, Khurana E, Bafna V, Felau I, Zenklusen JC, Laird PW, Curtis C, Cancer Genome Atlas Analysis N, Greenleaf WJ, Chang HY. Three-dimensional genome landscape of primary human cancers. Nat Genet. 2025;57(5):1189-200. Epub 20250512. doi: 10.1038/s41588-025-02188-0. PubMed PMID: 40355593; PMCID: PMC12081301.

99. Almassalha LM, Bauer GM, Wu W, Cherkezyan L, Zhang D, Kendra A, Gladstein S, Chandler JE, VanDerway D, Seagle BL, Ugolkov A, Billadeau DD, O'Halloran TV, Mazar AP, Roy HK, Szleifer I, Shahabi S, Backman V. Macrogenomic engineering via modulation of the scaling of chromatin packing density. Nat Biomed Eng. 2017;1(11):902-13. Epub 20171106. doi: 10.1038/s41551-017-0153-2. PubMed PMID: 29450107; PMCID: PMC5809134.

100. Stephens AD, Liu PZ, Banigan EJ, Almassalha LM, Backman V, Adam SA, Goldman RD, Marko JF. Chromatin histone modifications and rigidity affect nuclear morphology independent of lamins. Mol Biol Cell. 2018;29(2):220-33. Epub 20171115. doi: 10.1091/mbc.E17-06-0410. PubMed PMID: 29142071; PMCID: PMC5909933.

101. Almassalha LM, Carignano M, Liwag EP, Li WS, Gong R, Acosta N, Dunton CL, Gonzalez PC, Carter LM, Kakkaramadam R, Kroger M, MacQuarrie KL, Frederick J, Ye IC, Su P, Kuo T, Medina KI, Pritchard JA, Skol A, Nap R, Kanemaki M, Dravid V, Szleifer I, Backman V. Chromatin conformation, gene transcription, and nucleosome remodeling as an emergent system. Sci Adv. 2025;11(2):eadq6652. Epub 20250110. doi: 10.1126/sciadv.adq6652. PubMed PMID: 39792661; PMCID: PMC11721585.

102. Lieberman-Aiden E, van Berkum NL, Williams L, Imakaev M, Ragoczy T, Telling A, Amit I, Lajoie BR, Sabo PJ, Dorschner MO, Sandstrom R, Bernstein B, Bender MA, Groudine M, Gnirke A, Stamatoyannopoulos J, Mirny LA, Lander ES, Dekker J. Comprehensive mapping of long-range interactions reveals folding principles of the human genome. Science. 2009;326(5950):289-93. doi: 10.1126/science.1181369. PubMed PMID: 19815776; PMCID: PMC2858594.

103. Simonis M, Klous P, Splinter E, Moshkin Y, Willemsen R, de Wit E, van Steensel B, de Laat W. Nuclear organization of active and inactive chromatin domains uncovered by chromosome conformation capture-on-chip (4C). Nat Genet. 2006;38(11):1348-54. Epub 20061008. doi: 10.1038/ng1896. PubMed PMID: 17033623.

104. Kleffman K, Levinson G, Rose IVL, Blumenberg LM, Shadaloey SAA, Dhabaria A, Wong E, Galan-Echevarria F, Karz A, Argibay D, Von Itter R, Floristan A, Baptiste G, Eskow NM, Tranos JA, Chen J, Vega YSdMEC, Call M, Rogers R, Jour G, Wadghiri YZ, Osman I, Li YM, Mathews P, DeMattos RB, Ueberheide B, Ruggles KV, Liddelow SA, Schneider RJ, Hernando E. Melanoma-Secreted Amyloid Beta Suppresses Neuroinflammation and Promotes Brain Metastasis. Cancer Discov. 2022;12(5):1314-35. doi: 10.1158/2159-8290.CD-21-1006. PubMed PMID: 35262173; PMCID: PMC9069488.

105. Ibrahim M, Illa-Bochaca I, Jour G, Vega-Saenz de Miera E, Fracasso J, Ruggles K, Osman I, Schober M. NF1 Loss Promotes EGFR Activation and Confers Sensitivity to EGFR Inhibition in NF1 Mutant Melanoma. Cancer Res. 2025. Epub 20250610. doi: 10.1158/0008-5472.CAN-24-3904. PubMed PMID: 40494652; PMCID: PMC12221223.

106. Liu L, Luo Q, Sun J, Ju Y, Morita Y, Song G. Chromatin organization regulated by EZH2-mediated H3K27me3 is required for OPN-induced migration of bone marrow-derived mesenchymal stem cells. Int J Biochem Cell Biol. 2018;96:29-39. Epub 20180111. doi: 10.1016/j.biocel.2018.01.006. PubMed PMID: 29337251.

107. Stephens AD, Banigan EJ, Adam SA, Goldman RD, Marko JF. Chromatin and lamin A determine two different mechanical response regimes of the cell nucleus. Mol Biol Cell. 2017;28(14):1984-96. Epub 20170105. doi: 10.1091/mbc.E16-09-0653. PubMed PMID: 28057760; PMCID: PMC5541848.

108. Stephens AD, Banigan EJ, Marko JF. Chromatin's physical properties shape the nucleus and its functions. Curr Opin Cell Biol. 2019;58:76-84. Epub 20190316. doi: 10.1016/j.ceb.2019.02.006. PubMed PMID: 30889417; PMCID: PMC6692209.

109. Wang X, Luan Y, Yue F. EagleC: A deep-learning framework for detecting a full range of structural variations from bulk and single-cell contact maps. Sci Adv. 2022;8(24):eabn9215. Epub 20220615. doi: 10.1126/sciadv.abn9215. PubMed PMID: 35704579; PMCID: PMC9200291.

110. Corces MR, Granja JM, Shams S, Louie BH, Seoane JA, Zhou W, Silva TC, Groeneveld C, Wong CK, Cho SW, Satpathy AT, Mumbach MR, Hoadley KA, Robertson AG, Sheffield NC,

Felau I, Castro MAA, Berman BP, Staudt LM, Zenklusen JC, Laird PW, Curtis C, Cancer Genome Atlas Analysis N, Greenleaf WJ, Chang HY. The chromatin accessibility landscape of primary human cancers. Science. 2018;362(6413). doi: 10.1126/science.aav1898. PubMed PMID: 30361341; PMCID: PMC6408149.

111. Puram SV, Tirosh I, Parikh AS, Patel AP, Yizhak K, Gillespie S, Rodman C, Luo CL, Mroz EA, Emerick KS, Deschler DG, Varvares MA, Mylvaganam R, Rozenblatt-Rosen O, Rocco JW, Faquin WC, Lin DT, Regev A, Bernstein BE. Single-Cell Transcriptomic Analysis of Primary and Metastatic Tumor Ecosystems in Head and Neck Cancer. Cell. 2017;171(7):1611-24 e24. Epub 20171130. doi: 10.1016/j.cell.2017.10.044. PubMed PMID: 29198524; PMCID: PMC5878932.

112. Chung W, Eum HH, Lee HO, Lee KM, Lee HB, Kim KT, Ryu HS, Kim S, Lee JE, Park YH, Kan Z, Han W, Park WY. Single-cell RNA-seq enables comprehensive tumour and immune cell profiling in primary breast cancer. Nat Commun. 2017;8:15081. Epub 20170505. doi: 10.1038/ncomms15081. PubMed PMID: 28474673; PMCID: PMC5424158.

113. Patel AP, Tirosh I, Trombetta JJ, Shalek AK, Gillespie SM, Wakimoto H, Cahill DP, Nahed BV, Curry WT, Martuza RL, Louis DN, Rozenblatt-Rosen O, Suva ML, Regev A, Bernstein BE. Single-cell RNA-seq highlights intratumoral heterogeneity in primary glioblastoma. Science. 2014;344(6190):1396-401. Epub 20140612. doi: 10.1126/science.1254257. PubMed PMID: 24925914; PMCID: PMC4123637.

114. Rambow F, Rogiers A, Marin-Bejar O, Aibar S, Femel J, Dewaele M, Karras P, Brown D, Chang YH, Debiec-Rychter M, Adriaens C, Radaelli E, Wolter P, Bechter O, Dummer R, Levesque M, Piris A, Frederick DT, Boland G, Flaherty KT, van den Oord J, Voet T, Aerts S, Lund AW, Marine JC. Toward Minimal Residual Disease-Directed Therapy in Melanoma. Cell. 2018;174(4):843-55 e19. Epub 20180712. doi: 10.1016/j.cell.2018.06.025. PubMed PMID: 30017245.

115. Polyak K, Weinberg RA. Transitions between epithelial and mesenchymal states: acquisition of malignant and stem cell traits. Nat Rev Cancer. 2009;9(4):265-73. Epub 20090305. doi: 10.1038/nrc2620. PubMed PMID: 19262571.

116. Barkley D, Moncada R, Pour M, Liberman DA, Dryg I, Werba G, Wang W, Baron M, Rao A, Xia B, Franca GS, Weil A, Delair DF, Hajdu C, Lund AW, Osman I, Yanai I. Cancer cell states recur across tumor types and form specific interactions with the tumor microenvironment. Nat Genet. 2022;54(8):1192-201. Epub 20220805. doi: 10.1038/s41588-022-01141-9. PubMed PMID: 35931863; PMCID: PMC9886402.

117. Shaffer SM, Dunagin MC, Torborg SR, Torre EA, Emert B, Krepler C, Beqiri M, Sproesser K, Brafford PA, Xiao M, Eggan E, Anastopoulos IN, Vargas-Garcia CA, Singh A, Nathanson KL, Herlyn M, Raj A. Rare cell variability and drug-induced reprogramming as a mode of cancer drug resistance. Nature. 2017;546(7658):431-+. doi: 10.1038/nature22794 http://www.nature.com/nature/journal/vaop/ncurrent/abs/nature22794.html#supplementary-information.

118. Tan YY, Li JJ, Zhao GY, Huang KC, Cardenas H, Wang YN, Matei D, Cheng JX. Metabolic reprogramming from glycolysis to fatty acid uptake and beta-oxidation in platinum-resistant cancer cells. Nature Communications. 2022;13(1). doi: 10.1038/s41467-022-32101-w. PubMed PMID: WOS:000836609800006.

119. Sundaram L, Kumar A, Zatzman M, Salcedo A, Ravindra N, Shams S, Louie BH, Bagdatli ST, Myers MA, Sarmashghi S, Choi HY, Choi WY, Yost KE, Zhao Y, Granja JM, Hinoue T, Hayes DN, Cherniack A, Felau I, Choudhry H, Zenklusen JC, Farh KK, McPherson A, Curtis C, Laird PW, Cancer Genome Atlas Analysis Networkdouble d, Demchok JA, Yang L, Tarnuzzer R, Caesar-Johnson SJ, Wang Z, Doane AS, Khurana E, Castro MAA, Lazar AJ, Broom BM, Weinstein JN, Akbani R, Kumar SV, Raphael BJ, Wong CK, Stuart JM, Safavi R, Benz CC, Johnson BK, Kyi C, Shen H, Corces MR, Chang HY, Greenleaf WJ. Single-cell chromatin accessibility reveals malignant regulatory programs in primary human cancers. Science. 2024;385(6713):eadk9217. Epub 20240906. doi: 10.1126/science.adk9217. PubMed PMID: 39236169; PMCID: PMC12289346.

120. Do C, Jiang G, Cova G, Zappile P, Heguy A, Skok JA. The coordination between CTCF, cohesin and TFs impacts nucleosome repositioning and chromatin insulation to define state specific 3D chromatin folding. bioRxiv. 2025. Epub 20250521. doi: 10.1101/2024.11.02.620823. PubMed PMID: 39605491; PMCID: PMC11601386.
121. Rao SSP, Huang SC, Glenn St Hilaire B, Engreitz JM, Perez EM, Kieffer-Kwon KR, Sanborn AL, Johnstone SE, Bascom GD, Bochkov ID, Huang X, Shamim MS, Shin J, Turner D, Ye Z, Omer AD, Robinson JT, Schlick T, Bernstein BE, Casellas R, Lander ES, Aiden EL. Cohesin Loss Eliminates All Loop Domains. Cell. 2017;171(2):305-20 e24. doi: 10.1016/j.cell.2017.09.026. PubMed PMID: 28985562; PMCID: PMC5846482.
122. Phillips JE, Corces VG. CTCF: master weaver of the genome. Cell. 2009;137(7):1194-211. doi: 10.1016/j.cell.2009.06.001. PubMed PMID: 19563753; PMCID: PMC3040116.
123. Narita T, Kilic S, Higashijima Y, Scherer NM, Pappas G, Maskey E, Choudhary C. Disentangling the architectural and non-architectural functions of CTCF and cohesin in gene regulation. Nat Genet. 2025. Epub 20251118. doi: 10.1038/s41588-025-02404-x. PubMed PMID: 41254162.
124. Zhan P, Xi GM, Zhang B, Wu Y, Liu HB, Liu YF, Xu WJ, Zhu Q, Cai F, Zhou ZJ, Miu YY, Wang XX, Jin JJ, Li Q, Lv TF, Song Y. NCAPG2 promotes tumour proliferation by regulating G2/M phase and associates with poor prognosis in lung adenocarcinoma. J Cell Mol Med. 2017;21(4):665-76. Epub 20161115. doi: 10.1111/jcmm.13010. PubMed PMID: 27862966; PMCID: PMC5345611.
125. Hu WF, Krieger KL, Lagundzin D, Li X, Cheung RS, Taniguchi T, Johnson KR, Bessho T, Monteiro ANA, Woods NT. CTDP1 regulates breast cancer survival and DNA repair through BRCT-specific interactions with FANCI. Cell Death Discov. 2019;5:105. Epub 20190619. doi: 10.1038/s41420-019-0185-3. PubMed PMID: 31240132; PMCID: PMC6584691.
126. Marques E, Englund JI, Tervonen TA, Virkunen E, Laakso M, Myllynen M, Makela A, Ahvenainen M, Lepikhova T, Monni O, Hautaniemi S, Klefstrom J. Par6G suppresses cell proliferation and is targeted by loss-of-function mutations in multiple cancers. Oncogene. 2016;35(11):1386-98. Epub 20150615. doi: 10.1038/onc.2015.196. PubMed PMID: 26073086; PMCID: PMC4800288.
127. Shoshan E, Braeuer RR, Kamiya T, Mobley AK, Huang L, Vasquez ME, Velazquez-Torres G, Chakravarti N, Ivan C, Prieto V, Villares GJ, Bar-Eli M. NFAT1 Directly Regulates IL8 and MMP3 to Promote Melanoma Tumor Growth and Metastasis. Cancer Res. 2016;76(11):3145-55. Epub 20160324. doi: 10.1158/0008-5472.CAN-15-2511. PubMed PMID: 27013197; PMCID: PMC4891299.
128. Lee YC, Tsai KW, Liao JB, Kuo WT, Chang YC, Yang YF. High expression of tight junction protein 1 as a predictive biomarker for bladder cancer grade and staging. Sci Rep. 2022;12(1):1496. Epub 20220127. doi: 10.1038/s41598-022-05631-y. PubMed PMID: 35087173; PMCID: PMC8795112.
129. Martinez-Noel G, Luck K, Kuhnle S, Desbuleux A, Szajner P, Galligan JT, Rodriguez D, Zheng L, Boyland K, Leclere F, Zhong Q, Hill DE, Vidal M, Howley PM. Network Analysis of UBE3A/E6AP-Associated Proteins Provides Connections to Several Distinct Cellular Processes. J Mol Biol. 2018;430(7):1024-50. Epub 20180206. doi: 10.1016/j.jmb.2018.01.021. PubMed PMID: 29426014; PMCID: PMC5866790.
130. Janssen SM, Moscona R, Elchebly M, Papadakis AI, Redpath M, Wang H, Rubin E, van Kempen LC, Spatz A. BORIS/CTCFL promotes a switch from a proliferative towards an invasive phenotype in melanoma cells. Cell Death Discov. 2020;6:1. Epub 20200102. doi: 10.1038/s41420-019-0235-x. PubMed PMID: 32123577; PMCID: PMC7026120.
131. Moscona R, Janssen SM, Elchebly M, Papadakis AI, Rubin E, Spatz A. BORIS/CTCFL-mediated chromatin accessibility alterations promote a pro-invasive transcriptional signature in melanoma cells. Pigment Cell Melanoma Res. 2023;36(3-4):299-313. Epub 20230421. doi: 10.1111/pcmr.13089. PubMed PMID: 37082838.

132. Xu X, Jarajapu V, Chadourne M, Soto-Vargas Z, Ochoa-Rios SL, Jasani N, Wang K, Mecozzi N, Yao J, Yu X, Karreth FA. FRA1 drives melanoma metastasis through an actionable transcriptional network. Oncogene. 2025. Epub 20251124. doi: 10.1038/s41388-025-03632-5. PubMed PMID: 41286309.
133. Acosta N, Gong R, Su Y, Frederick J, Medina KI, Li WS, Mohammadian K, Almassalha L, Wang G, Backman V. Three-color single-molecule localization microscopy in chromatin. Light: Science & Applications. 2025;14(1):123. doi: 10.1038/s41377-025-01786-1.
134. Nicetto D, Donahue G, Jain T, Peng T, Sidoli S, Sheng L, Montavon T, Becker JS, Grindheim JM, Blahnik K, Garcia BA, Tan K, Bonasio R, Jenuwein T, Zaret KS. H3K9me3-heterochromatin loss at protein-coding genes enables developmental lineage specification. Science. 2019;363(6424):294-7. Epub 20190103. doi: 10.1126/science.aau0583. PubMed PMID: 30606806; PMCID: PMC6664818.
135. Kim YJ, Sheu KM, Tsoi J, Abril-Rodriguez G, Medina E, Grasso CS, Torrejon DY, Champhekar AS, Litchfield K, Swanton C, Speiser DE, Scumpia PO, Hoffmann A, Graeber TG, Puig-Saus C, Ribas A. Melanoma dedifferentiation induced by IFN-gamma epigenetic remodeling in response to anti-PD-1 therapy. J Clin Invest. 2021;131(12). doi: 10.1172/JCI145859. PubMed PMID: 33914706; PMCID: PMC8203459.
136. Fontanals-Cirera B, Hasson D, Vardabasso C, Di Micco R, Agrawal P, Chowdhury A, Gantz M, de Pablos-Aragoneses A, Morgenstern A, Wu P, Filipescu D, Valle-Garcia D, Darvishian F, Roe JS, Davies MA, Vakoc CR, Hernando E, Bernstein E. Harnessing BET Inhibitor Sensitivity Reveals AMIGO2 as a Melanoma Survival Gene. Mol Cell. 2017;68(4):731-44 e9. doi: 10.1016/j.molcel.2017.11.004. PubMed PMID: 29149598; PMCID: PMC5993436.

Figure 1

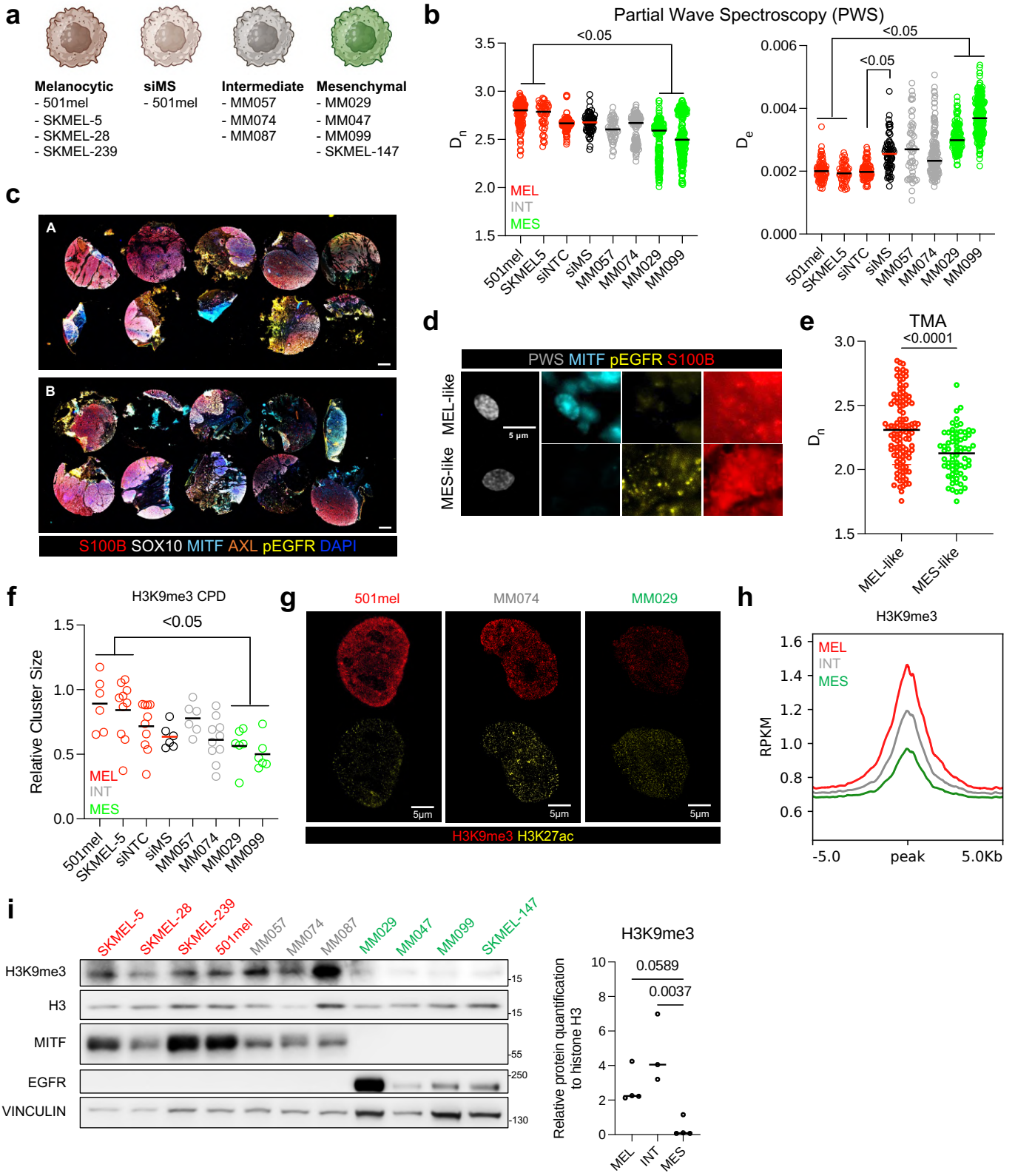
a
Melanocytic
- 501mel
- SKMEL-5
- SKMEL-28
- SKMEL-239
siMS
- 501mel
Intermediate
- MM057
- MM074
- MM087
Mesenchymal
- MM029
- MM047
- MM099
- SKMEL-147
b
Partial Wave Spectroscopy (PWS)
<0.05
D_n
MEL
INT
MES
501mel
SKMEL5
siNTC
siMS
MM057
MM074
MM029
MM099
D_e
c
A
B
S100B SOX10 MITF AXL pEGFR DAPI
d
PWS MITF pEGFR S100B
MEL-like
MES-like
5 µm
e
TMA
<0.0001
MEL-like
MES-like
f
H3K9me3 CPD
Relative Cluster Size
g
501mel
MM074
MM029
5µm
H3K9me3 H3K27ac
h
H3K9me3
RPKM
-5.0
peak
5.0Kb
i
SKMEL-5
SKMEL-28
SKMEL-239
501mel
MM057
MM074
MM087
MM029
MM047
MM099
SKMEL-147
H3K9me3
H3
MITF
EGFR
VINCULIN
15
55
250
130
Relative protein quantification to histone H3
0.0589
0.0037

Figure 2

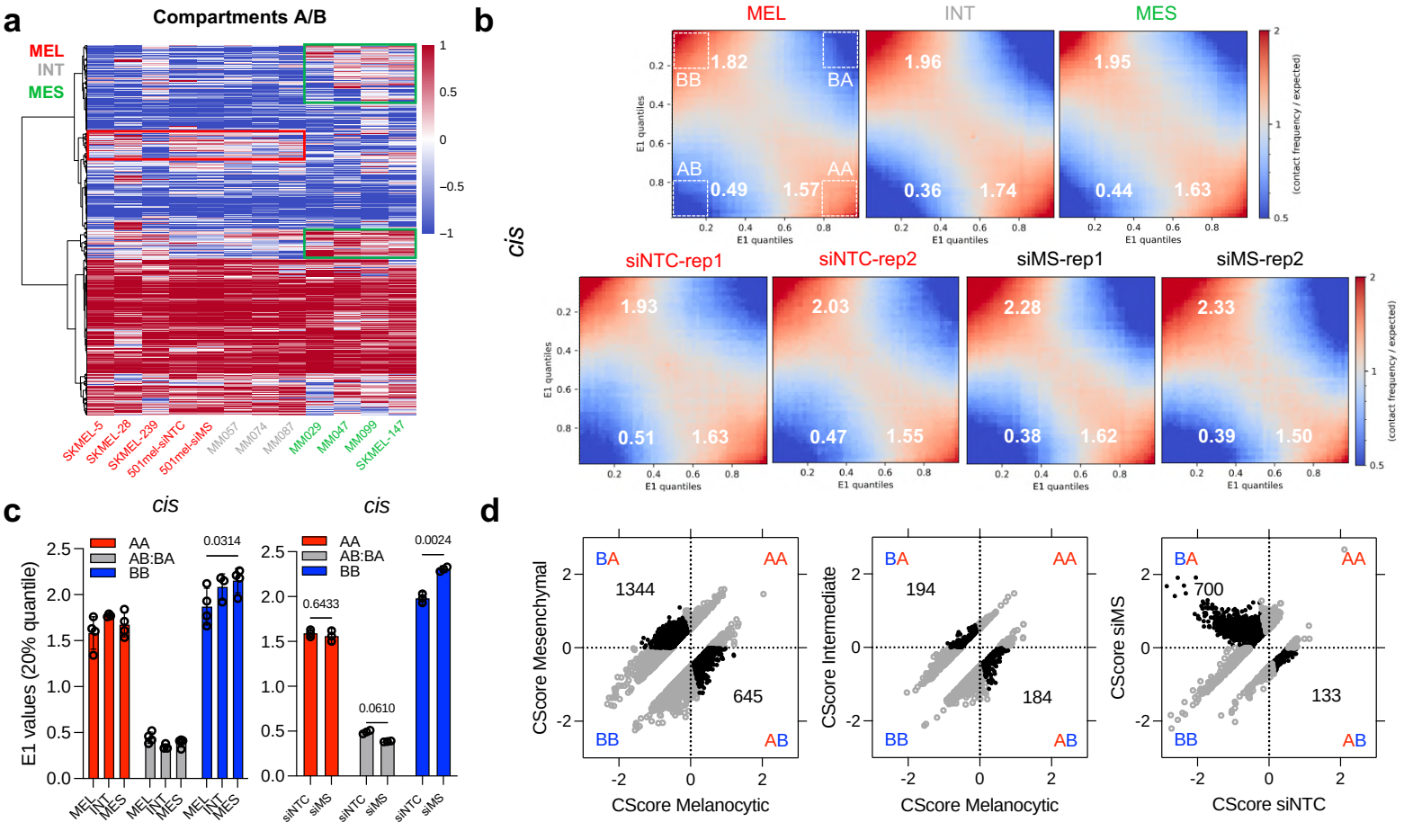
a
Compartments A/B
MEL
INT
MES
SKMEL-5
SKMEL-28
SKMEL-239
501mel-siNTC
501mel-siMS
MM057
MM074
MM087
MM029
MM047
MM099
SKMEL-147
b
cis
MEL
INT
MES
1.82
BB
BA
AB
AA
0.49
1.57
1.96
0.36
1.74
1.95
0.44
1.63
E1 quantiles
(contact frequency / expected)
siNTC-rep1
siNTC-rep2
siMS-rep1
siMS-rep2
1.93
0.51
1.63
2.03
0.47
1.55
2.28
0.38
1.62
2.33
0.39
1.50
c
cis
cis
E1 values (20% quantile)
AA
AB:BA
BB
0.0314
0.6433
0.0610
0.0024
MEL
INT
MES
siNTC
siMS
d
CScore Mesenchymal
CScore Melanocytic
1344
645
CScore Intermediate
194
184
CScore siMS
CScore siNTC
700
133

Figure 3

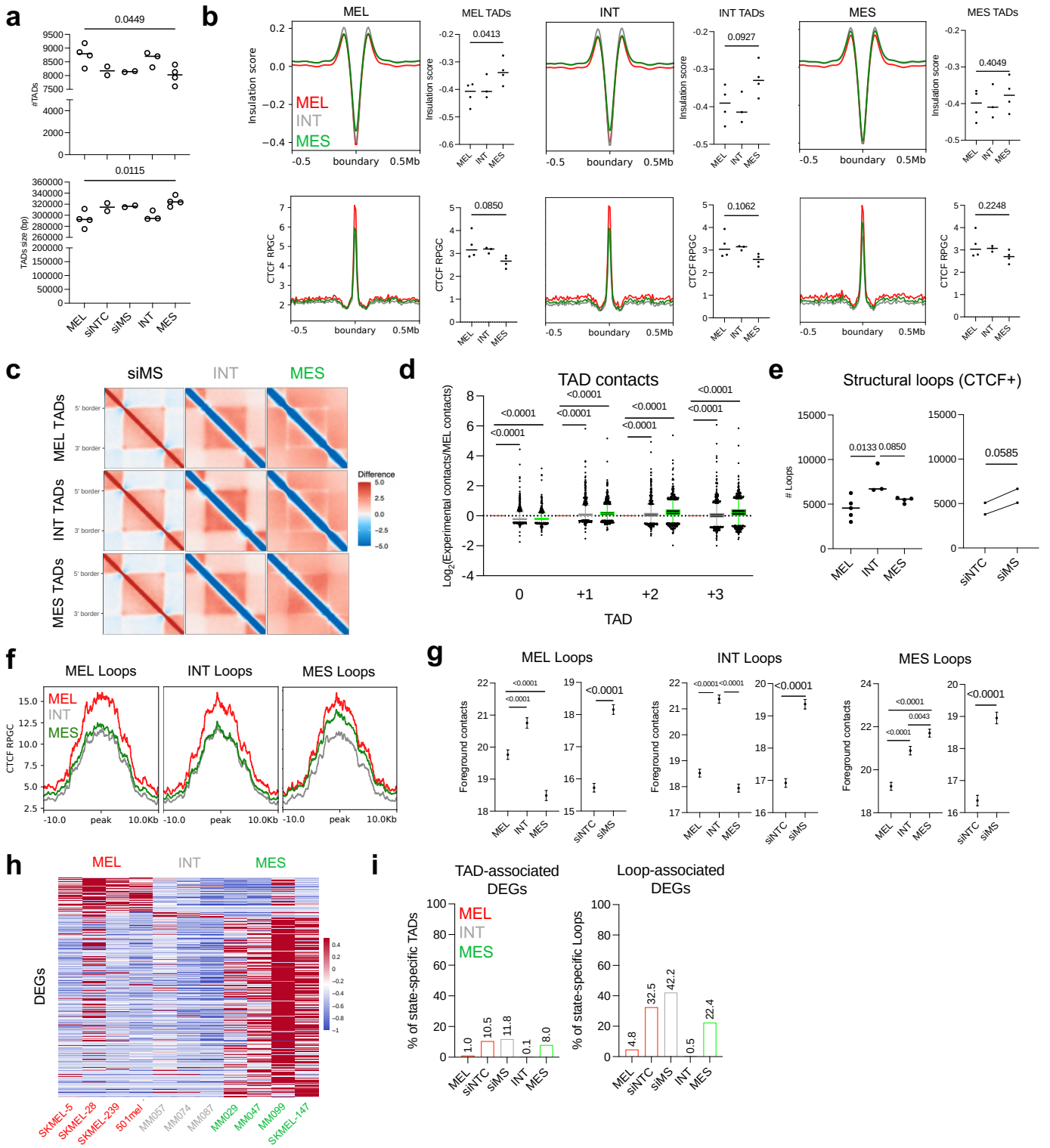
a
0.0449
#TADs
0.0115
TADs size (bp)
MEL
siNTC
siMS
INT
MES
b
MEL
INT
MES
MEL TADs
INT TADs
MES TADs
Insulation score
CTCF RPGC
0.0413
0.0927
0.4049
0.0850
0.1062
0.2248
-0.5
boundary
0.5Mb
c
siMS
INT
MES
MEL TADs
INT TADs
MES TADs
5' border
3' border
Difference
d
TAD contacts
Log2(Experimental contacts/MEL contacts)
<0.0001
0
+1
+2
+3
TAD
e
Structural loops (CTCF+)
Loops
0.0133
0.0850
0.0585
f
MEL Loops
INT Loops
MES Loops
CTCF RPGC
peak
10.0Kb
g
MEL Loops
INT Loops
MES Loops
Foreground contacts
0.0043
h
MEL
INT
MES
DEGs
SKMEL-5
SKMEL-28
SKMEL-239
501mel
MM057
MM074
MM087
MM029
MM047
MM099
SKMEL-147
i
TAD-associated DEGs
Loop-associated DEGs
% of state-specific TADs
% of state-specific Loops
1.0
10.5
11.8
0.1
8.0
4.8
32.5
42.2
0.5
22.4

Figure 4

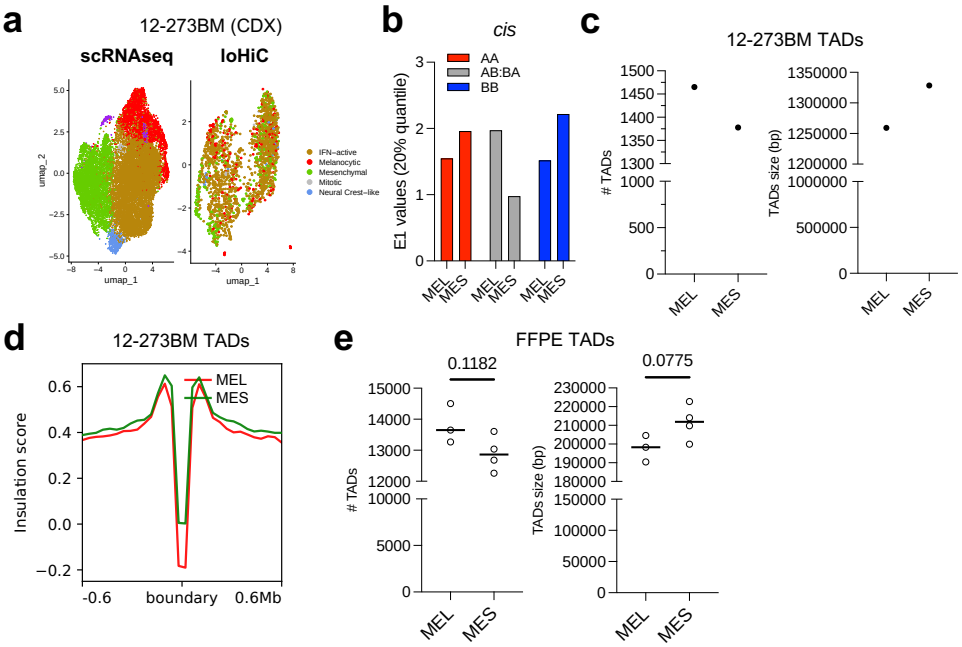
a
12-273BM (CDX)
scRNAseq
loHiC
umap_2
umap_1
IFN–active
Melanocytic
Mesenchymal
Mitotic
Neural Crest–like
b
cis
AA
AB:BA
BB
E1 values (20% quantile)
MEL
MES
c
12-273BM TADs
TADs
TADs size (bp)
MEL
MES
d
12-273BM TADs
MEL
MES
Insulation score
-0.6
boundary
0.6Mb
e
FFPE TADs
0.1182
0.0775
TADs
TADs size (bp)
MEL
MES

Figure 5

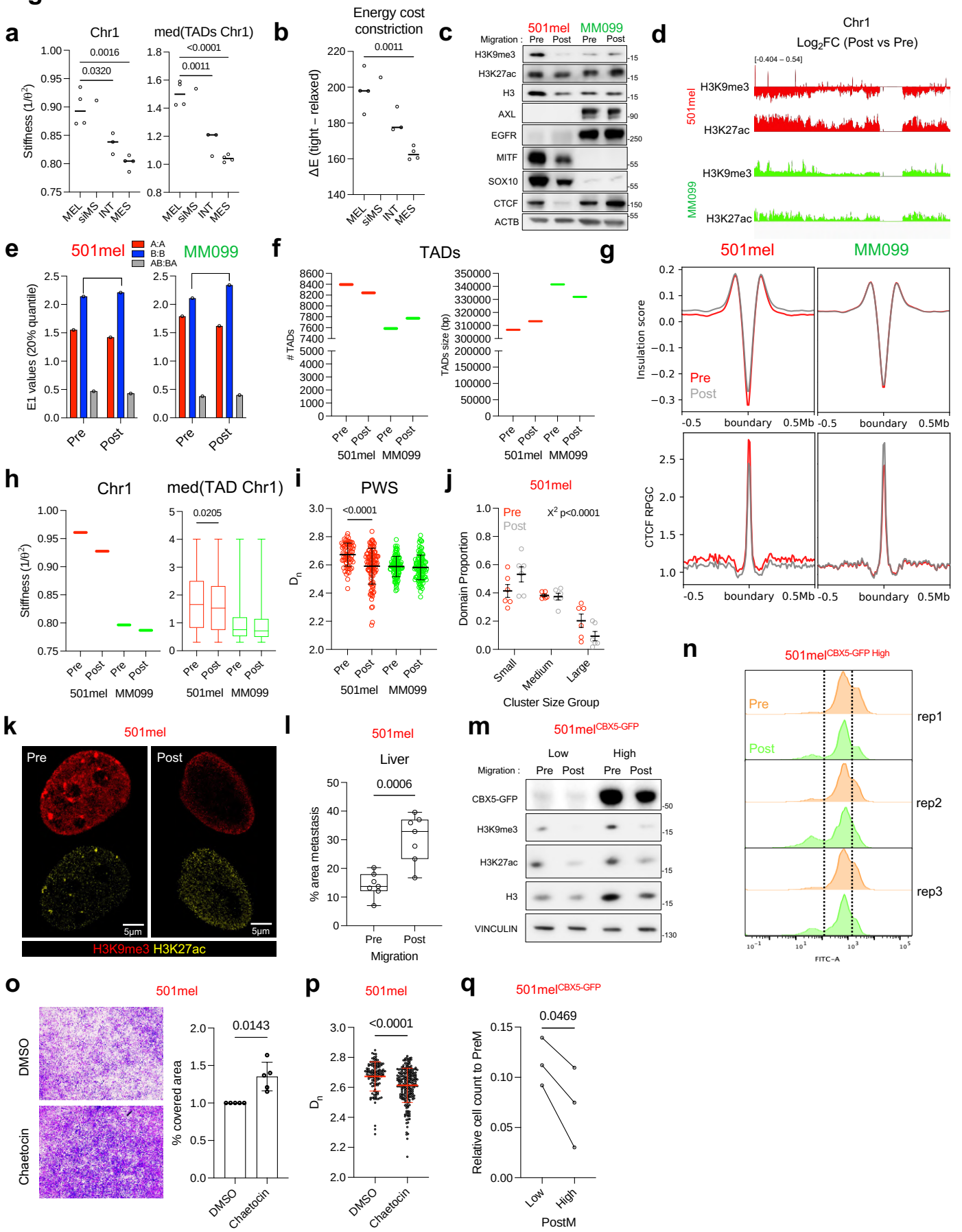
a
Chr1
med(TADs Chr1)
Stiffness (1/θ²)
0.0016
0.0320
<0.0001
0.0011
MEL
siMS
INT
MES
b
Energy cost constriction
ΔE (tight – relaxed)
0.0011
c
501mel
MM099
Migration :
Pre
Post
H3K9me3
H3K27ac
H3
AXL
EGFR
MITF
SOX10
CTCF
ACTB
d
Chr1
Log2FC (Post vs Pre)
[-0.404 – 0.54]
501mel
MM099
H3K9me3
H3K27ac
e
501mel
MM099
A:A
B:B
AB:BA
E1 values (20% quantile)
Pre
Post
f
TADs
TADs
TADs size (bp)
g
501mel
MM099
Insulation score
Pre
Post
-0.5
boundary
0.5Mb
CTCF RPGC
h
Chr1
med(TAD Chr1)
Stiffness (1/θ²)
0.0205
i
PWS
<0.0001
Dn
j
501mel
Pre
Post
X² p<0.0001
Domain Proportion
Small
Medium
Large
Cluster Size Group
n
501mel CBX5-GFP High
Pre
Post
rep1
rep2
rep3
FITC-A
k
501mel
Pre
Post
5µm
H3K9me3 H3K27ac
l
501mel
Liver
0.0006
% area metastasis
Migration
m
501mel CBX5-GFP
Low
High
CBX5-GFP
H3K9me3
H3K27ac
H3
VINCULIN
o
501mel
DMSO
Chaetocin
0.0143
% covered area
p
501mel
<0.0001
Dn
q
501mel CBX5-GFP
0.0469
Relative cell count to PreM
PostM

Figure 6

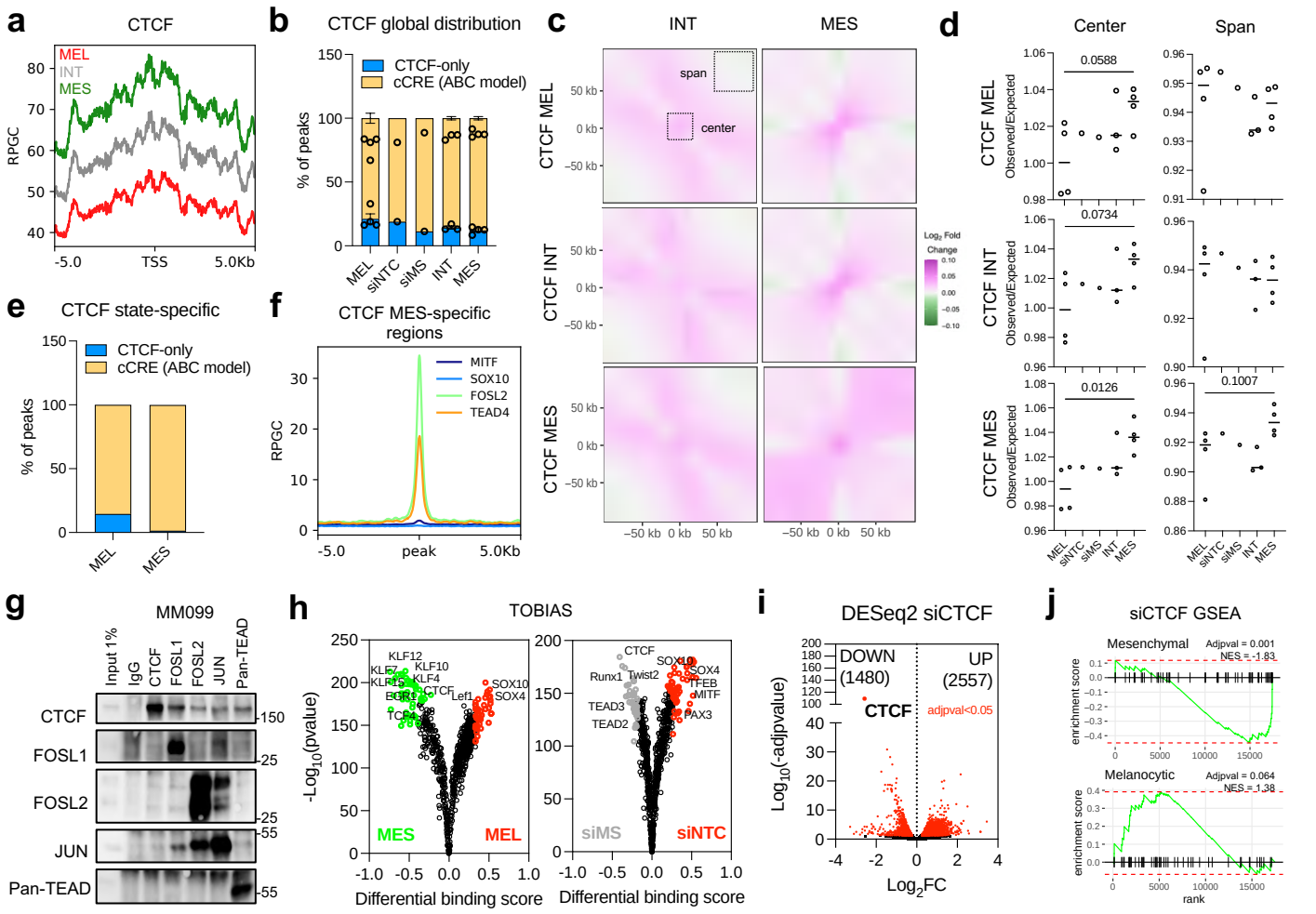
a
CTCF
MEL
INT
MES
RPGC
-5.0
TSS
5.0Kb
b
CTCF global distribution
CTCF-only
cCRE (ABC model)
% of peaks
MEL
siNTC
siMS
INT
MES
c
INT
MES
span
center
CTCF MEL
CTCF INT
CTCF MES
50 kb
0 kb
−50 kb
Log2 Fold Change
d
Center
Span
CTCF MEL
CTCF INT
CTCF MES
Observed/Expected
0.0588
0.0734
0.0126
0.1007
e
CTCF state-specific
CTCF-only
cCRE (ABC model)
% of peaks
MEL
MES
f
CTCF MES-specific regions
MITF
SOX10
FOSL2
TEAD4
RPGC
-5.0
peak
5.0Kb
g
MM099
Input 1%
IgG
CTCF
FOSL1
FOSL2
JUN
Pan-TEAD
h
TOBIAS
-Log10(pvalue)
MES
MEL
siMS
siNTC
Differential binding score
i
DESeq2 siCTCF
DOWN
(1480)
UP
(2557)
CTCF
adjpval<0.05
Log10(-adjpvalue)
Log2FC
j
siCTCF GSEA
Mesenchymal
Adjpval = 0.001
NES = -1.83
Melanocytic
Adjpval = 0.064
NES = 1.38
enrichment score
rank

Figure 7

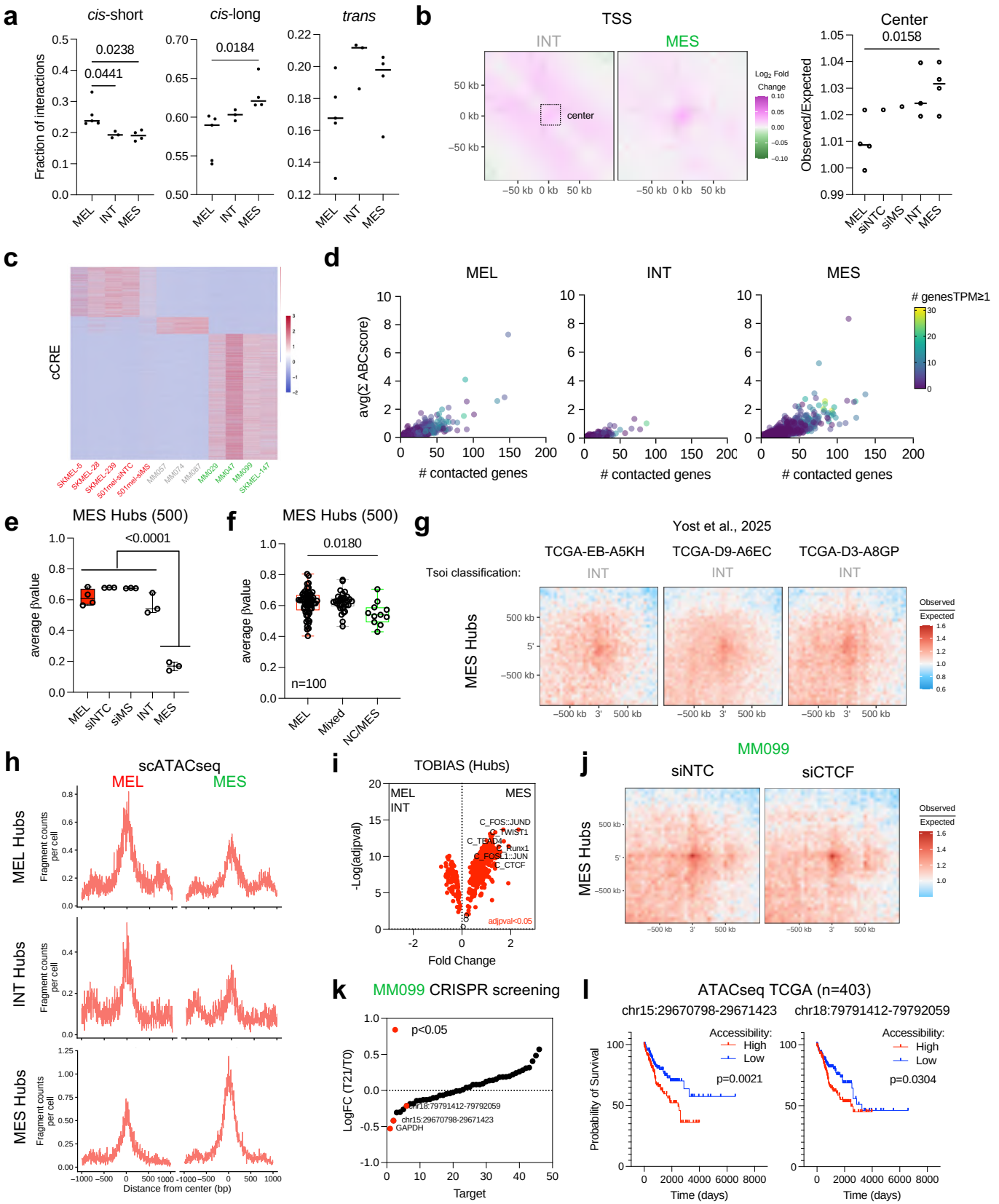
a
cis-short
cis-long
trans
Fraction of interactions
0.0238
0.0441
0.0184
MEL
INT
MES
b
TSS
INT
MES
center
Log2 Fold Change
Center
0.0158
Observed/Expected
MEL
siNTC
siMS
INT
MES
c
cCRE
SKMEL-5
SKMEL-28
SKMEL-239
501mel-siNTC
501mel-siMS
MM057
MM074
MM087
MM029
MM047
MM099
SKMEL-147
d
MEL
INT
MES
avg(Σ ABCscore)
# contacted genes
# genesTPM≥1
e
MES Hubs (500)
<0.0001
average βvalue
MEL
siNTC
siMS
INT
MES
f
MES Hubs (500)
0.0180
average βvalue
n=100
MEL
Mixed
NC/MES
g
Yost et al., 2025
TCGA-EB-A5KH
TCGA-D9-A6EC
TCGA-D3-A8GP
Tsoi classification:
INT
MES Hubs
500 kb
5'
−500 kb
Observed
Expected
h
scATACseq
MEL
MES
MEL Hubs
INT Hubs
MES Hubs
Fragment counts per cell
Distance from center (bp)
i
TOBIAS (Hubs)
MEL
INT
MES
-Log(adjpval)
Fold Change
C_FOS::JUND
TWIST1
C_TBX4
C_Runx1
C_FOSL1::JUN
C_CTCF
adjpval<0.05
j
MM099
siNTC
siCTCF
MES Hubs
Observed
Expected
k
MM099 CRISPR screening
p<0.05
LogFC (T21/T0)
chr18:79791412-79792059
chr15:29670798-29671423
GAPDH
Target
l
ATACseq TCGA (n=403)
chr15:29670798-29671423
chr18:79791412-79792059
Accessibility:
High
Low
p=0.0021
p=0.0304
Probability of Survival
Time (days)

Supplemental Figure 1

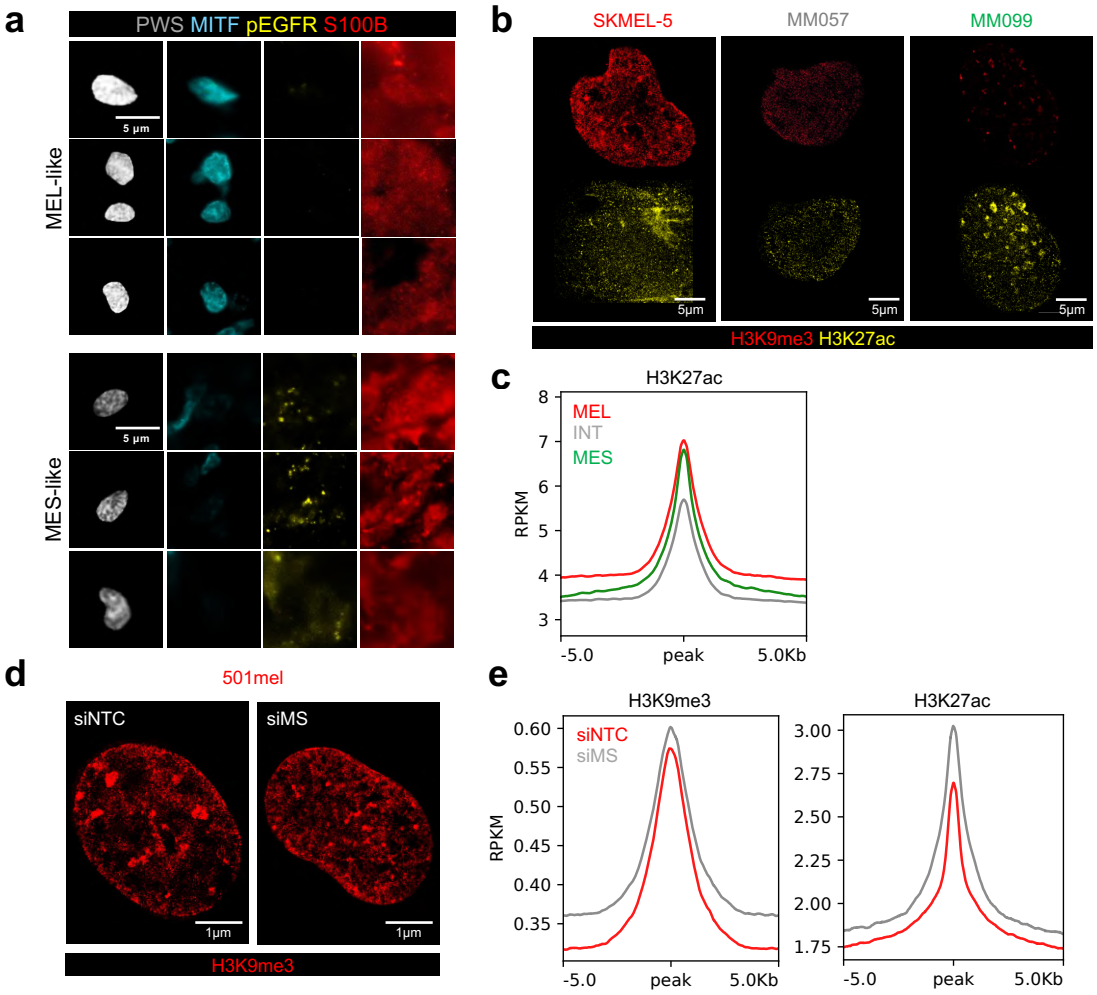

Supplemental Figure 2

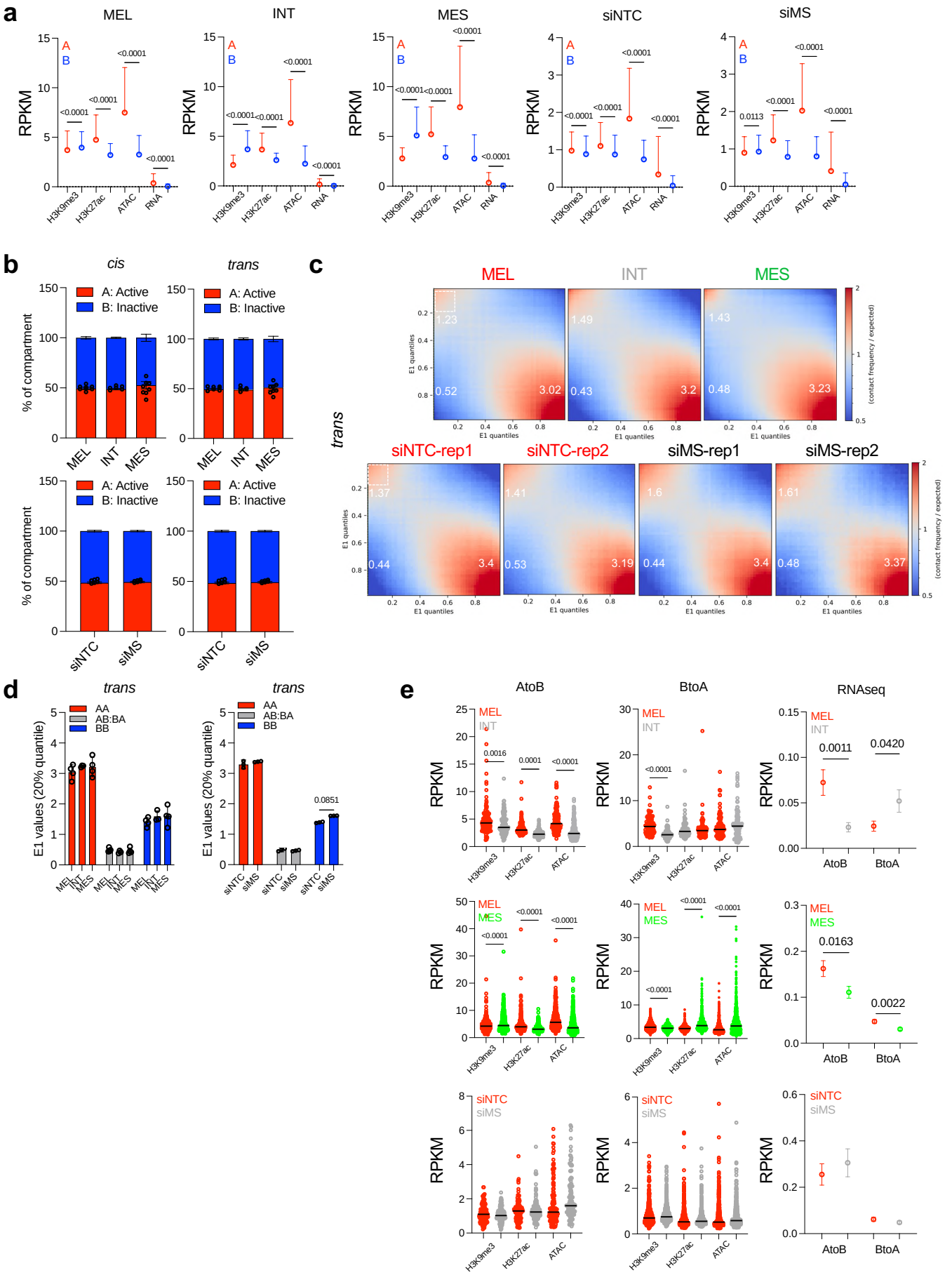

Supplemental Figure 3

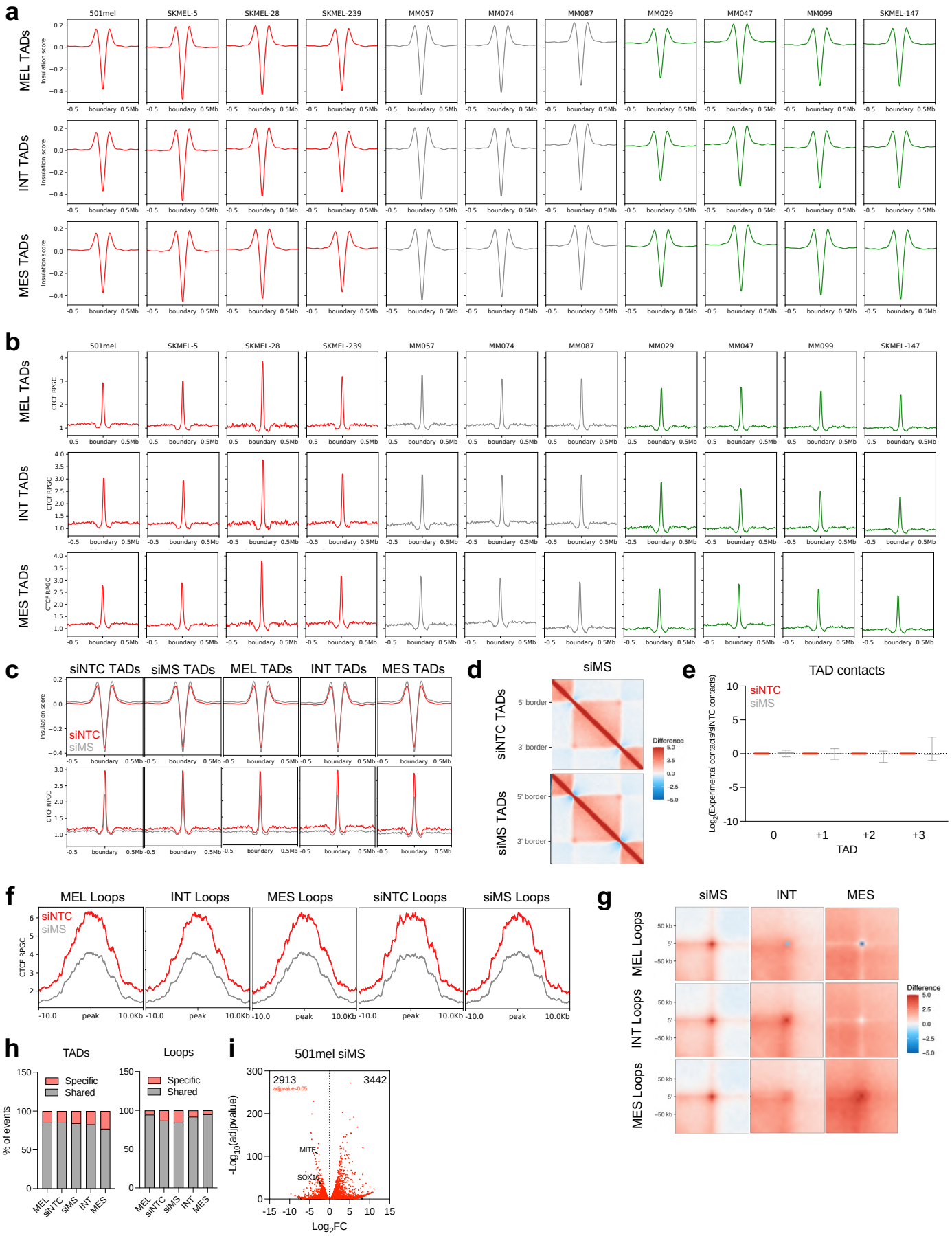

Supplemental Figure 4

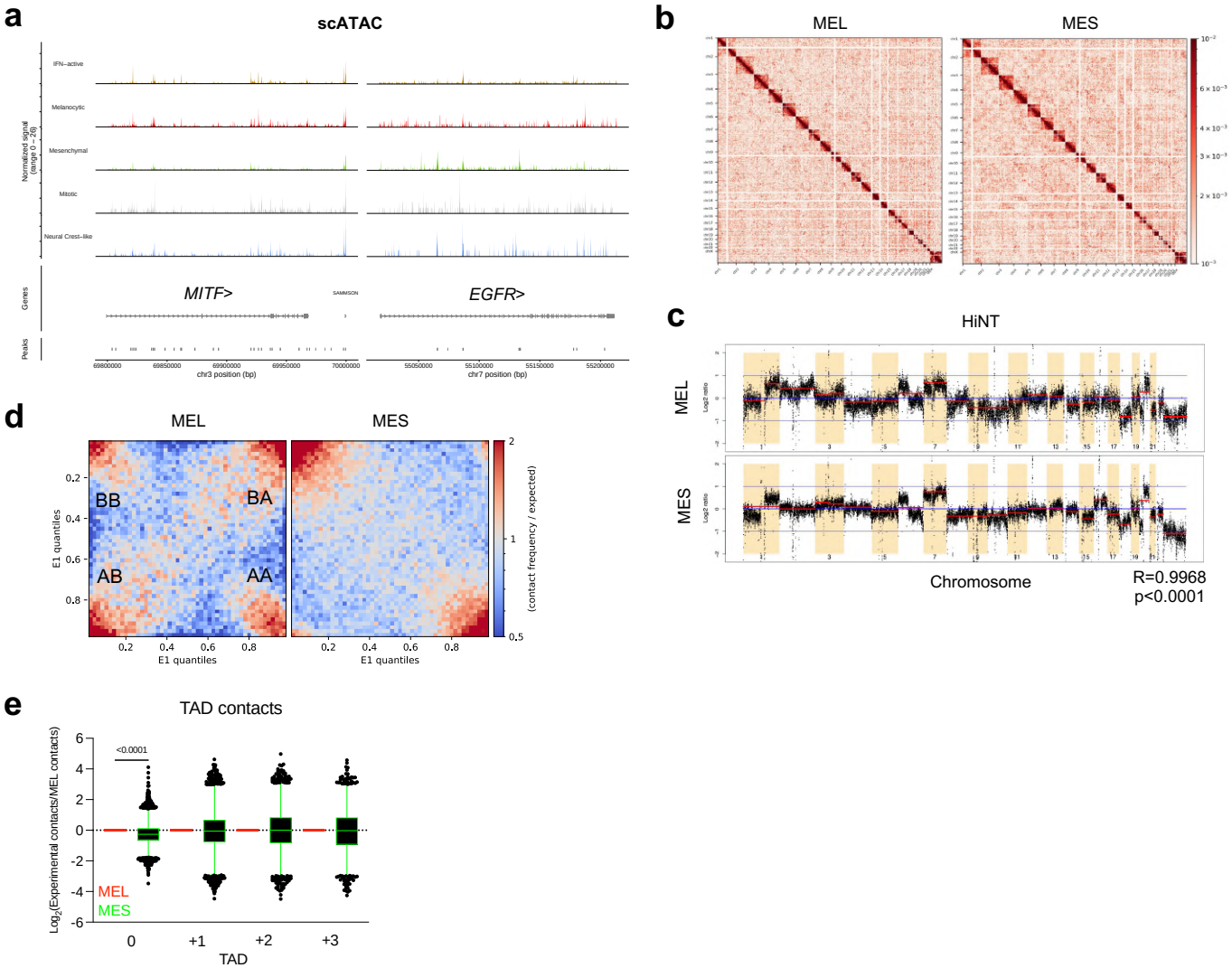

Supplemental Figure 5

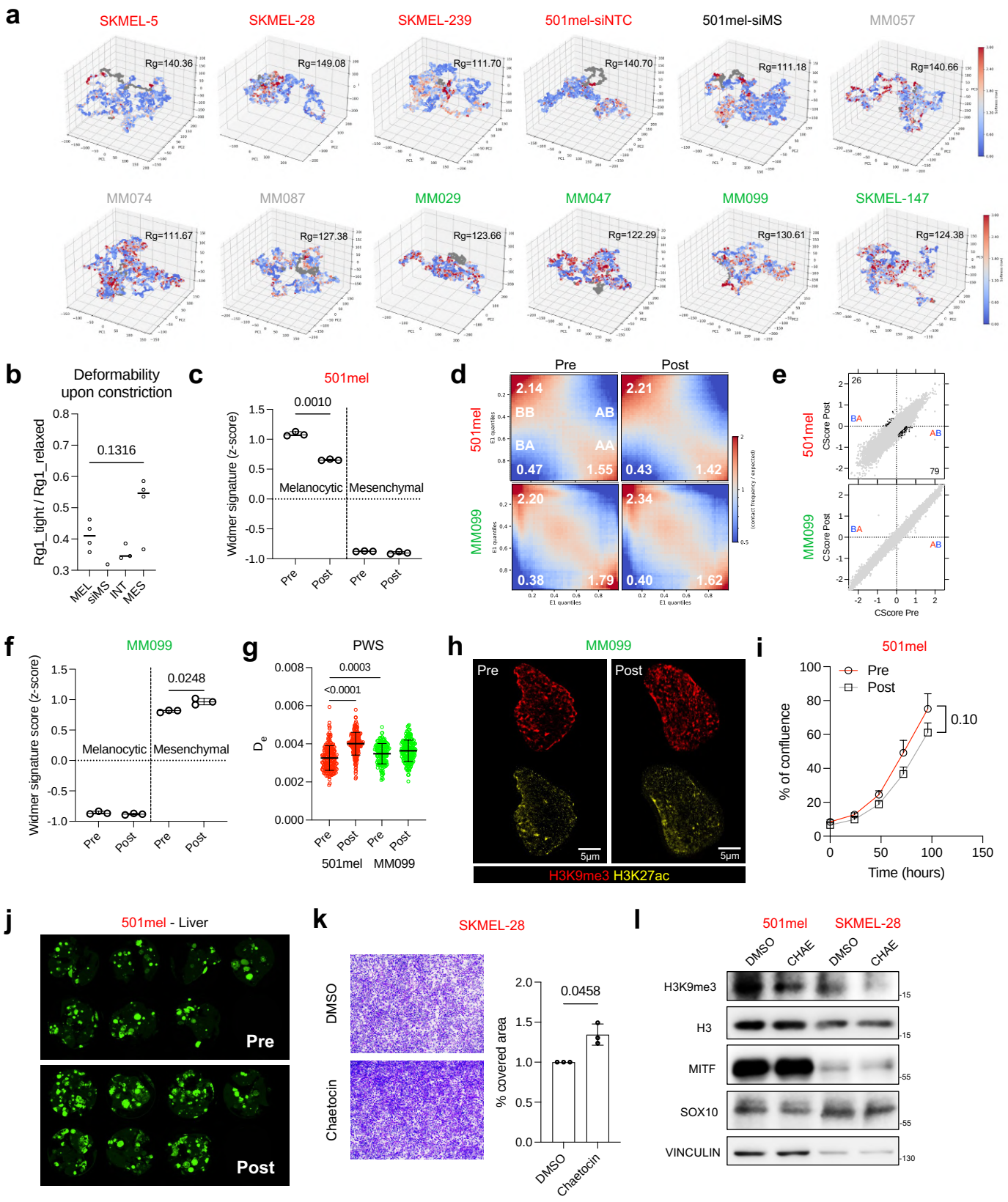

Supplemental Figure 6

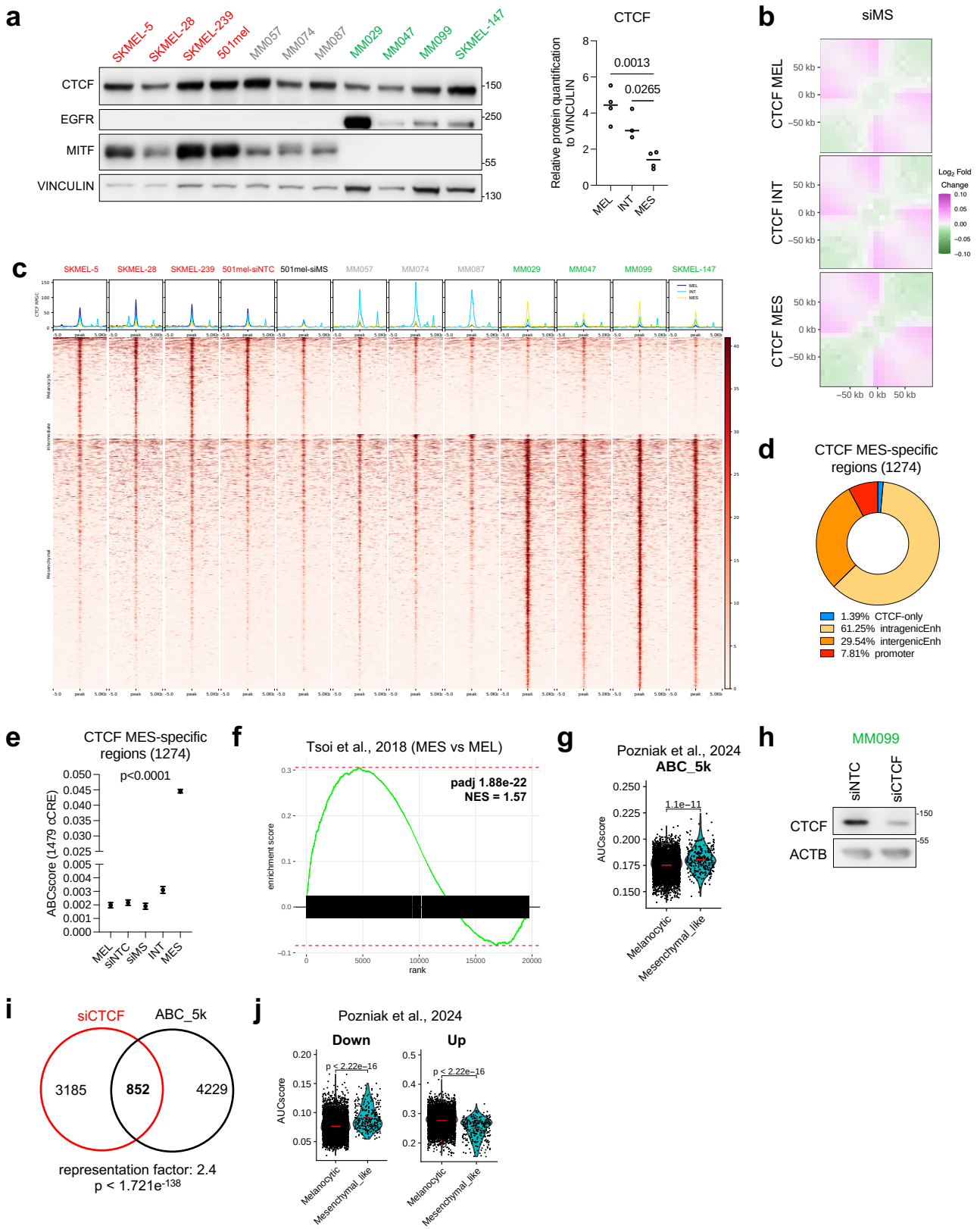
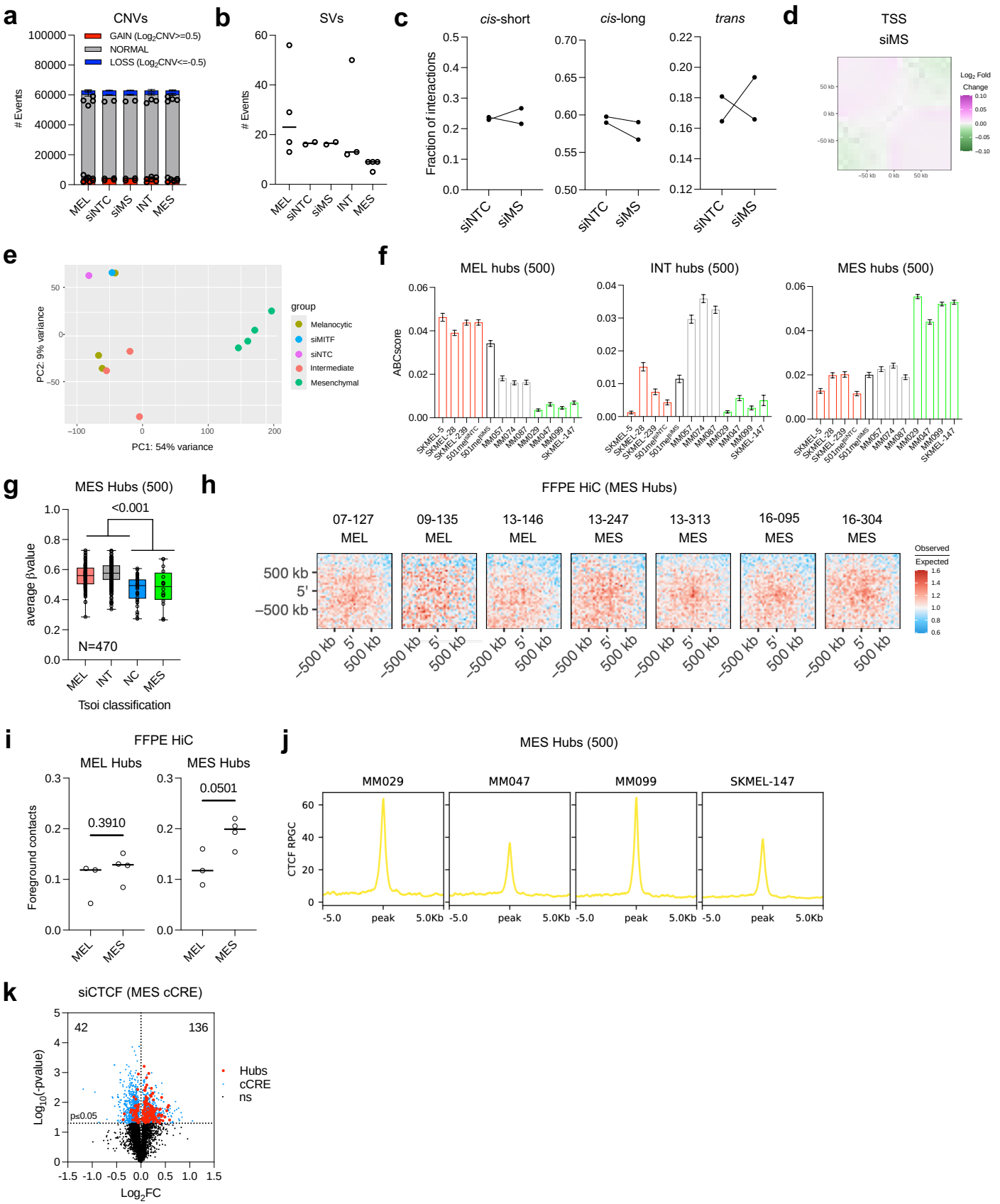
Supplemental Figure 7